

Investigation of the active site  
of the [FeFe] hydrogenase from  
*Desulfovibrio desulfuricans*

Inaugural-Dissertation

zur

Erlangung des Doktorgrades der  
Mathematisch-Naturwissenschaftlichen Fakultät  
der Heinrich-Heine-Universität Düsseldorf

vorgelegt von

**Alexey Evgenievich Silakov**  
aus der Russischen Föderation

Düsseldorf 2007

angefertigt am  
Max-Planck-Institut für Bioanorganische Chemie  
in Mülheim an der Ruhr  
unter Anteilung von Dr. E.Reijerse und Prof.Dr. W.Lubitz.

Gedruckt mit der Genehmigung der  
Mathematisch-Naturwissenschaftlichen Fakultät  
der Heinrich-Heine-Universität Düsseldorf

Referent: Prof. Dr. W. Lubitz  
Koreferent: Prof. Dr. G. Büldt  
Tag der mündlichen Prüfung: 17. 01. 2007

---

# Abstract

**Alexey Evgenievich Silakov**

Hydrogen plays an important role in the metabolism of certain microorganisms, where the reaction  $H_2 \rightleftharpoons 2H^+ + 2e^-$  is catalyzed by metalloenzymes called hydrogenases. The active site of the [FeFe] hydrogenase (the so called H-cluster) contains a classical [4Fe4S] cluster connected via the sulphur of a cysteine residue to a bi-nuclear cluster. The  $[2Fe]_H$  subcluster is coordinated by CO and CN ligands, which stabilize metals in low-oxidation states.

Several states of the active site can be detected using EPR. The oxidized form of the H-cluster ( $H_{ox}$ ) shows a very characteristic rhombic EPR spectrum. The distal iron of the  $[2Fe]_H$  subcluster has an exchangeable coordination site. Upon inhibition of the protein by CO, this coordination site is occupied by the CO ligand (the so-called  $H_{ox}$ -CO state). In this case an axial EPR signal is observed.

In this thesis, the active site of the [FeFe] hydrogenase from the *Desulfovibrio desulfuricans* was investigated in various states. The electronic structure of the H-cluster was studied using CW EPR and advanced pulse EPR techniques including Davies-ENDOR, and HYSCORE. The nuclear spin interactions of the  $^1H$ ,  $^{13}C$ ,  $^{14}N$  and  $^{57}Fe$  nuclei were determined. It was found that the  $H_{ox}$ -CO state is characterized by a rather strong  $[2Fe]_H$ -[4Fe4S] $_H$  exchange interaction and moderate localization of the unpaired spin on the bi-nuclear subcluster. In contrast, the exchange interaction in the  $H_{ox}$  state is much weaker. The unpaired spin density was found to be almost equally distributed over the iron atoms of the bi-nuclear subcluster. These facts point to large changes in the electronic structure of the H-cluster upon inhibition by CO.

The light induced conversion of the  $H_{ox}$ -CO state has been studied as a function of the excitation wavelength at low temperature (40 K). Two additional species were detected by EPR during illumination. Investigation of the wavelength dependence of the photo-dissociation conversion rates shows, that this dependence is related to the optical absorption spectrum of the [FeFe] hydrogenase.

In order to characterize the light-induced species, they were examined for the first time by advanced EPR spectroscopy. One of these species has been identified as the  $H_{ox}$  state. The other species is characterized by an EPR spectrum with large rhombicity. According to earlier FT-IR studies, the second species most probably has lost the bridging CO ligand. However, the study presented in this thesis suggests that the former bridging CO ligand is in the terminal position of one of the irons of the binuclear subcluster. The investigation of the electronic structure of the second light induced species reveals, that in terms of the exchange coupling this state is intermediate between the  $H_{ox}$  and the  $H_{ox}$ -CO states.

---

## Acknowledgment

I would like to thank Prof. Dr. W. Lubitz. for giving me the opportunity to perform this study in the Max Planck Institute for Bioinorganic Chemistry and I am thankful for his support of the projects presented in this thesis.

Prof. Dr. Büldt is gratefully acknowledged for being a second reviewer of my thesis.

It was a great pleasure for me to have Dr. E. J. Reijerse as my supervisor. I would like to thank him for many useful scientific discussions we had together and for his constant support and advice. I am also very grateful for his patience while working on corrections of this thesis.

I sincerely thank Prof. Dr. S. P. J. Albracht and Prof. Dr. E. C. Hatchikian for providing the  $^{57}\text{Fe}$  and most of the  $^{13}\text{C}$  enriched samples of the [FeFe]-hydrogenase.

I acknowledge Dr. C. Fichtner and D. Johanson for their work on the first "domestic" preparations of the [FeFe]-hydrogenase. I am also thankful to B. Wenk for continuing the preparations and further support with samples for my investigation.

I would like to thank Dr. B. Epel for his advice about EPR spectroscopy as well as for his help with the 'SpecMan' software and hardware.

Dr. J. Niklas is gratefully acknowledged for useful discussions as well as for his help in correcting this thesis.

I'm grateful to G. Klihm and F. Reikowski for their help with handling the EPR spectrometers.

Finally, the work done during a PhD course would not be so interesting and effective without the encouragement of friends and family. I am thanking all of them for their help, advice and support.

# Contents

<b>1</b>	<b>Introduction</b>	<b>7</b>
<b>2</b>	<b>[FeFe] hydrogenase</b>	<b>11</b>
2.1	Structure of the [FeFe] hydrogenase . . . . .	11
2.2	Active site of the [FeFe] hydrogenase . . . . .	13
2.3	Redox and coordination states of the H-cluster . . . . .	14
2.4	Exchange-coupling model of the H-cluster in the paramagnetic states . . . . .	19
<b>3</b>	<b>Motivation of the work</b>	<b>21</b>
<b>4</b>	<b>EPR spectroscopy</b>	<b>23</b>
4.1	Spin Hamiltonian . . . . .	23
4.1.1	The Spin Hamiltonian approach . . . . .	23
4.1.2	Zeeman interaction . . . . .	23
4.1.3	Hyperfine interaction . . . . .	25
4.1.4	Quadrupole interaction . . . . .	26
4.2	EPR methods . . . . .	27
4.2.1	Measurement of EPR spectra . . . . .	27
4.2.2	ENDOR . . . . .	31
4.2.3	TRIPLE . . . . .	32
4.2.4	ESEEM and HYSCORE . . . . .	34
4.3	Density matrix formalism . . . . .	37
4.4	Relaxation effects in TRIPLE experiment . . . . .	40
<b>5</b>	<b>Materials and methods</b>	<b>45</b>
5.1	Purification and activation of the enzyme . . . . .	45
5.2	Preparation of samples for EPR measurements . . . . .	46
5.3	X-band EPR experiments . . . . .	46
5.4	Q-band EPR experiments and 'SpecMan' set-up . . . . .	47
5.5	Photo-dissociation experiments . . . . .	48
5.6	Simulation of EPR, ENDOR and HYSCORE spectra . . . . .	49

---

5.7	UV/Vis experiments . . . . .	51
<b>6</b>	<b>The <math>H_{ox}</math>-CO state of the H-cluster</b>	<b>53</b>
6.1	EPR spectra of non-labeled samples . . . . .	53
6.2	Investigation of the $^{57}Fe$ HF couplings . . . . .	54
6.2.1	Broadening effect in the EPR spectrum . . . . .	54
6.2.2	Pulse ENDOR study . . . . .	56
6.2.3	HYSORE study . . . . .	62
6.2.4	Assignment of the HF couplings to the iron nuclei . . . . .	64
6.3	Investigation of the $^{13}C$ HF couplings of the CO ligands . . . . .	67
6.3.1	Labeling by $^{13}C$ isotope . . . . .	67
6.3.2	HYSORE measurements . . . . .	68
6.3.3	Q-band ENDOR measurements . . . . .	71
6.3.4	Assignment . . . . .	71
6.4	Discussion . . . . .	73
6.4.1	The spin-coupling model . . . . .	73
6.4.2	Oxidation states of the iron atoms in $[2Fe]_H$ -subcluster . . . . .	74
<b>7</b>	<b>The <math>H_{ox}</math> state of the H-cluster</b>	<b>75</b>
7.1	CW EPR spectra of non-labeled samples . . . . .	75
7.2	Investigation of the $^{57}Fe$ HF couplings . . . . .	77
7.2.1	Pulse ENDOR study . . . . .	77
7.2.2	Lineshape analysis of CW EPR spectra . . . . .	82
7.2.3	Assignment . . . . .	84
7.3	Investigation of the $^{14}N$ nuclear spin couplings . . . . .	85
7.4	Summary and Discussion . . . . .	92
7.4.1	Electronic structure . . . . .	92
7.4.2	Comparison with earlier spectroscopic studies . . . . .	92
<b>8</b>	<b>Photo-dissociation of the <math>H_{ox}</math>-CO state</b>	<b>95</b>
8.1	Light-induced states . . . . .	95
8.2	Photo-dissociation kinetics . . . . .	98
8.2.1	Processing of the EPR data . . . . .	98
8.2.2	Kinetics . . . . .	99
8.3	Dissociation models and wavelength dependence of the conversion rates .	101
8.3.1	Kinetic models . . . . .	102
8.3.2	Wavelength dependence . . . . .	106
8.4	Summary and discussion . . . . .	108

---

<b>9</b>	<b>The second light induced state</b>	<b>111</b>
9.1	EPR spectra . . . . .	111
9.2	Investigation of the $^{57}\text{Fe}$ HF couplings . . . . .	113
9.3	$^1\text{H}$ ENDOR study . . . . .	117
9.4	Investigation of the $^{14}\text{N}$ nuclear spin interactions . . . . .	119
9.5	Investigation of the $^{13}\text{C}$ HF couplings . . . . .	123
9.6	Discussion . . . . .	125
9.6.1	Electronic structure . . . . .	125
9.6.2	Comparison with theoretical studies . . . . .	126
<b>10</b>	<b>Summary and Outlook</b>	<b>127</b>
10.1	Summary . . . . .	127
10.2	Outlook . . . . .	129
	<b>References</b>	<b>130</b>
	<b>Curriculum Vitae</b>	<b>138</b>

## CONTENTS

---

---

# 1 Introduction

---

Many bacteria, archaea and a unique class of organelles, known as hydrogenosomes, use hydrogen in their metabolic processes. Such microorganisms are often closely associated in nature, which lead to proposal that their fusion resulted in the emergence of the eukaryotic cell. Hydrogen can be used either as a source of low potential electrons or, upon evolution of hydrogen, is used as a means of reoxidizing the redox pool of the cell. The hydrogenases are one of the oldest enzymes in nature. They catalyze the simple redox reaction:



In most of the cases this reaction could take place in both directions [1].

The function of the cytoplasmic hydrogenase is to remove excess reductants during microbial fermentation. The periplasmic hydrogenases have a function of hydrogen oxidation. For example, in the anaerobic sulfate-reducing bacterium *Desulfovibrio vulgaris*, protons ( $H^+$ ) produced from oxidation of hydrogen are used to drive ATP synthesis. The electrons are transferred into the *c*-type cytochrome network and delivered via the cytoplasmic membrane to the cytoplasm for the reduction of sulfate or thiosulfate (see figure 1.1) [1–3].

Hydrogenase found in various microorganisms can be quite different. Nevertheless, with regard to the overall metal content hydrogenases can be divided into three classes: [NiFe]-, [FeFe]- and [Fe]-hydrogenases.

The majority of hydrogenases contains nickel in addition to iron and are termed [NiFe]-hydrogenases. The X-ray crystal structure of the [NiFe] hydrogenase from *Desulfovibrio gigas* [4, 5] reveals that the active site is a Ni-Fe dinuclear center attached to the large subunit via four thiolates from Cys residues.

The iron atom is bound to three non-protein ligands: two cyanides and one carbon monoxide. Thus their active site is described as a  $(CysS)_2Ni(\mu-X)(\mu-CysS)_2Fe(CN)_2(CO)$  group [4–8] (figure 1.2). The small subunit contains two [4Fe4S] clusters and one [3Fe4S] cluster. By comparison of the amino acid sequences of [NiFe]-hydrogenases, it was

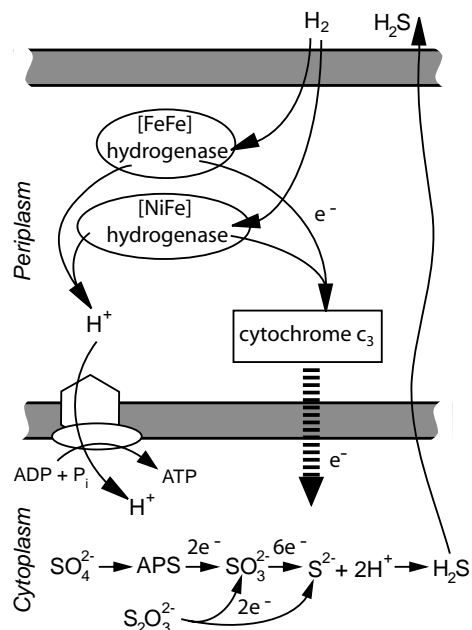


**Figure 1.1:** Simplified diagram of sulfate reduction in *D. vulgaris* Hildenborough (modified from [3]). The gaseous hydrogen diffuses to the periplasm. Here one of the hydrogenases oxidizes the hydrogen. The released electrons are captured by the *c*-type cytochrome network. The electrons are then be channeled through the cytoplasmic membrane by one of the transmembrane protein conduits and used in the reduction of sulfite to sulfide.

concluded that only the 'cubane' cluster closest to the active site is conserved in all enzymes [9]. FTIR studies [6–8] showed that [NiFe]-hydrogenases contain a set of three unique infrared absorption bands in the spectral region of  $2100 - 1850 \text{ cm}^{-1}$ . Since the frequency of IR bands is very sensitive to the status of the active site, it was concluded that these unique bands are due to intrinsic CO and CN ligands of the active site (diatomic molecules with a triple bond or triatomic molecules with two adjacent double bonds). Also a unique low spin Fe(II) site was detected, in addition to the high spin iron sites of the Fe-S clusters, by Mössbauer spectroscopy [10]. It is believed that the oxidation state (2+) of the iron atom of the [NiFe] cluster remains the same during the catalytic cycle [11, 12].

In addition, there is a subclass of [NiFe]-hydrogenases which contains nickel and selenium in equal proportions, the so-called [NiFeSe]-hydrogenases. These enzymes are widely distributed among sulfate-reducing bacteria [13–15] and are either periplasmic [14] or associated with the cytoplasmic membrane [16]. The crystal structure of the reduced periplasmic [NiFeSe] hydrogenase from *Desulfovibrio baculatum* reveals an

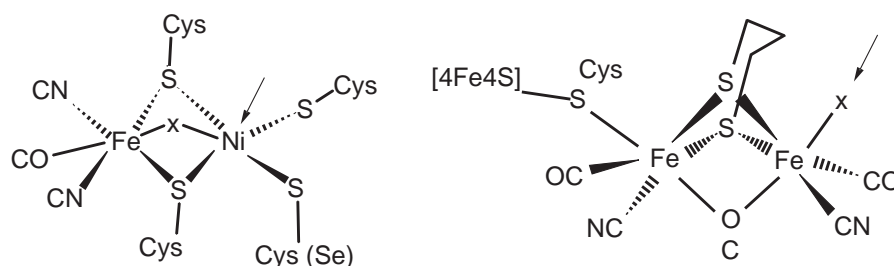


**Figure 1.2:** Schematic representation of the active sites of the [NiFe] (left) and [FeFe] (right) hydrogenases. If Se is present in the active site of an [NiFe]-hydrogenase it is located in one of the Cys of the Ni atom (shown in brackets). The arrows indicate open coordination sites.

overall similarity to that of [NiFe] hydrogenase from *D. gigas* and has a quite similar structure of the active site [17].

The second class of hydrogenases occurs in methanogenic Archaea [18, 19] and has long been thought to contain no metals. However, recently it was shown that the active site contains an  $\text{Fe}(\text{CO})_2$  group bound to an unknown organic cofactor [20–22]. These enzymes are now called [Fe]-hydrogenases. These enzymes,  $\text{H}_2$ -forming  $\text{N}^5, \text{N}^{10}$ -methylenetetrahydromethanopterin dehydrogenases, can activate  $\text{H}_2$  only in the presence of a second substrate (methenyl- $\text{H}_4\text{MPT}^1$ ) [23].

The third class is formed by [FeFe]-hydrogenases (previously known as 'Fe-only hydrogenase'), which exclusively contains iron. In contrast to the [Fe]-hydrogenases, the [FeFe]-hydrogenases have more than one iron in the active site and can oxidize hydrogen in the absence of additional cofactors. [FeFe]-hydrogenases are found in strictly anaerobic organisms and in many cases are very sensitive to molecular oxygen. In general, these hydrogenases can either be monomeric and cytoplasmic, or heterodimeric and periplasmic. These hydrogenases are involved in either hydrogen production or uptake, respectively [24].

The study presented in this thesis is focused on the [FeFe]-hydrogenases. The functional and structural properties of the paramagnetic states of the active site of this enzyme were examined by advanced EPR methods such as pulse ENDOR and ESEEM.

<sup>1</sup> $\text{H}_4\text{MPT}$  stands for 'tetrahydromethanopterin'



## 2 [FeFe] hydrogenase

### 2.1 Structure of the [FeFe] hydrogenase

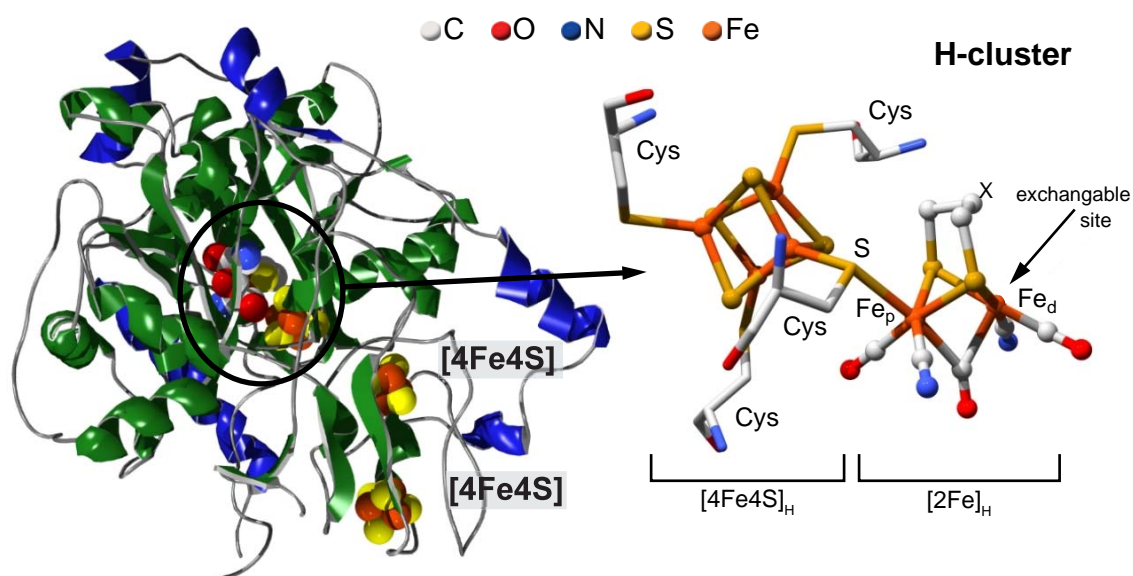


**Figure 2.1:** Structure of the [FeFe]-hydrogenase from *D. desulfuricans* (left) and the active site (H-cluster) in the oxidized active form (right). The coordinates of the protein structure were taken from the crystal structure published by Nicolet et al. [25] (Protein Data Bank entry: 1hfe). Coordinates of the H-cluster were combined from structures of the [FeFe]-hydrogenase from *D. desulfuricans* [25] and *C. pasteurianum* (hydrogenase I, Protein Data Bank entry 1c4a) [26]. The small arrow points to the open coordination site.

The anaerobic N<sub>2</sub>-fixing bacteria *Clostridium (C.) pasteurianum* was the first organism found to have a hydrogenase containing no nickel[27]. In fact, it is unique bacteria as it contains two different hydrogenases, neither of which contains nickel.. In earlier studies [24, 28] it was found that the prosthetic groups of [FeFe]-hydrogenase were located in only one subunit and consisted of several [4Fe4S] clusters and an active site of previously unknown structure, called the H-cluster (from 'hydrogen-activating cluster').

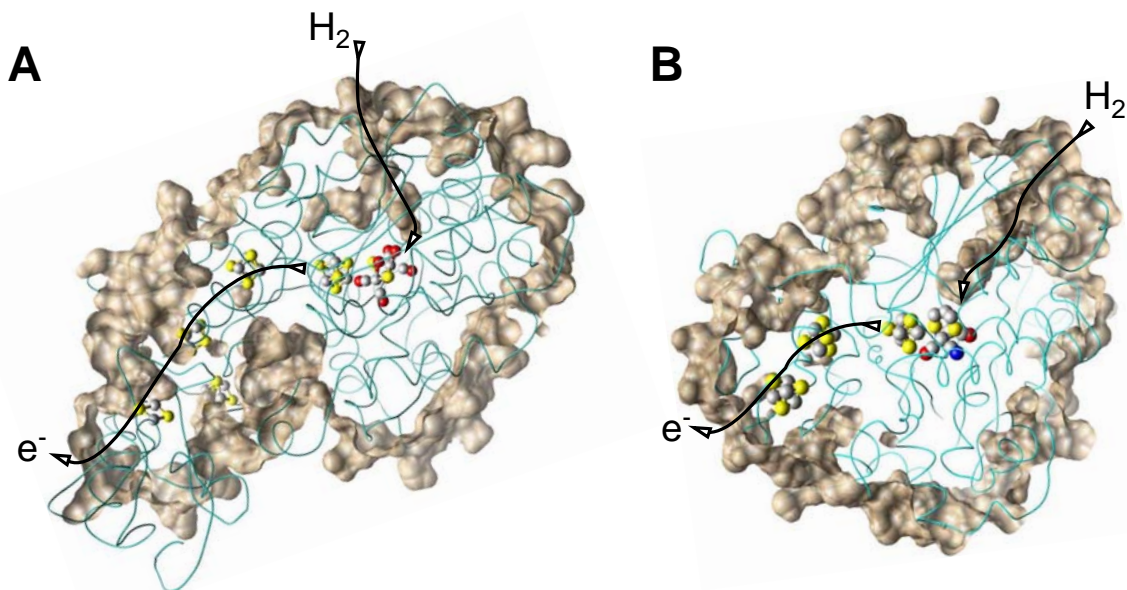


**Figure 2.2:** Analysis of the internal cavities in the bidirectional [FeFe] hydrogenases from *C. pasteurianum* (A) and *D. desulfuricans* (B). The proposed paths for hydrogen and electrons are marked by black lines. Analysis has been performed using a 0.75 Å probe, applied to the crystal structures of *C.p.I* (Protein Data Bank: 1c4a) and *D.d.* (Protein Data Bank: 1hfe)

The first [FeFe]-hydrogenase from *C. pasteurianum* (in this thesis it will be referred to as *C.p.I*) catalyzes the two-electron reduction of two protons to yield dihydrogen. It was found to contain 20 atoms of iron per mole of protein, arranged into five distinct [Fe-S] clusters. This hydrogenase was found to be very active in catalyzing both oxidation and evolution of the  $H_2$  and was thus named the 'bidirectional' hydrogenase [24].

The second hydrogenase purified from *C. pasteurianum* [29, 30] (*C.p.II*) was also active in  $H_2$  oxidation but rates of  $H_2$  evolution are very low. Analysis of the iron content shows that this hydrogenase contains approximately 8 irons [30, 31]. However, the physiological role of the *C.p.II* is yet unknown.

So far, the X-ray crystal structures of only two [FeFe]-hydrogenases are known. The structure of the cytoplasmic, monomeric *C.p.I* [FeFe]-hydrogenase, was resolved to 1.8 Å [32]. The second known structure is that of the periplasmic, heterodimeric [FeFe] hydrogenase from *Desulfovibrio (D.) desulfuricans* (ATCC 7757) (*D.d.*) [25] (resolved to 1.6 Å). In addition to the H-cluster, this enzyme was also found to contain two classical [4Fe4S] cubanes (so-called F-clusters).

The resolved structures of both enzymes (*D.d.* and *C.p.I*) reveal the existence of

hydrophobic channels from the 'surface' of the protein to the active site. This is similar to the [NiFe]-hydrogenases from *Desulfovibrio gigas* and *Desulfomicrobium baculatum* which were also found to have hydrophobic channels and cavities [33]. Based on this observation, it was postulated that these hydrophobic 'channels' serve as a pathway for the hydrogen gas substrate [25, 33]. Figure 2.2 shows a comparison between the structures of the [FeFe]-hydrogenases *D.d.* and *C.p.I.*, (protein databank code 1hfe and 1c4a, respectively). The structural analysis was performed using a small probe of radius 0.75 Å. Since the radius of H<sub>2</sub> is approximately 1 Å, some internal flexibility of the enzyme is required in order to allow gas passage [25].

In both structures, the enzymes contain a chain of iron-sulfur clusters. The [FeFe]-hydrogenase from *C. pasteurianum* contains in total of 5 iron-sulfur clusters, whereas the [FeFe]-hydrogenase from *Desulfovibrio vulgaris (desulfuricans)* contains three. In both cases it was suggested that the chain of iron-sulfur clusters provide the pathway for electrons to move from the surface to the active site of the protein.

In addition to these two crystal structures, there are also structures of the [FeFe]-hydrogenase in the CO-inhibited form of *C.p.I* [26, 34] and the *D. desulfuricans* enzyme prepared under H<sub>2</sub> [35].

## 2.2 Active site of the [FeFe] hydrogenase

The active center (the "H-cluster") of the [FeFe] hydrogenase from *D.d.* [25] is a six-iron cluster. It consists of a classical [4Fe4S] 'cubane' connected to the binuclear iron cluster whereby the sulfur ligand of a cysteine (figure 2.1). X-ray crystallography investigation of *C.p.I* reveals a structure of the active center almost identical to *D.d.* [32].

Similar to [NiFe] hydrogenase, it was discovered that [FeFe]-hydrogenases contains IR bands in the 2100 – 1850 cm<sup>-1</sup> spectral region, which strongly shift upon changes of the redox state of the enzyme [36–38]. By analogy to the [NiFe] hydrogenase these bands were assigned to the CN and CO ligands of the iron atoms of the H-cluster.

Earlier studies of the active site of the [FeFe] hydrogenase using pulse EPR methods such as ESEEM and HYSCORE revealed <sup>14</sup>N nuclear couplings with unusual quadrupole splitting, typical for CN ligands coordinated to low-spin irons. Basing on these observations, it was suggested that the [FeFe]-hydrogenases also contains one or two cyanide ligands, bound to the iron atoms [39, 40].

Recently, IR spectroscopic studies on the enzyme from *D.d.* [41] suggested that

## 2.3 Redox and coordination states of the H-cluster

---

each iron in the  $[2\text{Fe}]_{\text{H}}$  subcluster was coordinated by diatomic ligands CO and CN, thereby stabilizing the metals in low-oxidation states. Based on the crystallographic studies on the enzymes from *Clostridium pasteurianum* (*C.p.I*) [32] and *Desulfovibrio desulfuricans* [25], combined with IR studies on the *D. vulgaris* Hildenborough and *Megasphaera elsdenii* enzymes [8, 36] resulted in the proposed structure of the active site: an  $(\text{L})(\text{CO})(\text{CN})\text{Fe}(\mu\text{-RS}_2)(\mu\text{-CO})\text{Fe}(\text{CysS})(\text{CO})(\text{CN})$  moiety ( $[2\text{Fe}]_{\text{H}}$ ) linked via an Cys-thiol to a  $[4\text{Fe-4S}]$  'cubane' cluster ( $[4\text{Fe4S}]_{\text{H}}$ ).

Within the  $[2\text{Fe}]_{\text{H}}$  subcluster the iron atom bound to the Cys ligand is referred to as the proximal iron ( $\text{Fe}_p$ ) and the other iron atom is referred to as the distal one ( $\text{Fe}_d$ ). The distal iron ( $\text{Fe}_d$ ) has a vacant or exchangeable site. Remarkably, the hydrophobic channel, described above, is 'pointing' to  $\text{Fe}_d$  in the structures of both *C.p.I* and *D.d.* (see figure 2.2).

The linkage of the two thiol groups, coordinating iron atoms in the  $[2\text{Fe}]_{\text{H}}$  subcluster is another matter of discussion in the literature. A  $\text{S}(-(\text{CH}_2)_3\text{-})\text{S}$  (PDT) link was originally proposed from the crystal structure [25]. However, DFT calculations on the catalytic mechanism of the H-cluster [42, 43] and a reanalysis of the X-ray crystallographic data [35] suggested that the central atom was most likely a nitrogen, i.e.  $\text{S}(-\text{CH}_2\text{-NH-CH}_2\text{-})\text{S}$  (DTN), despite the lack of experimental data supporting this proposed structure.

Since the  $[\text{FeFe}]$  hydrogenases from *D. vulgaris* Hildenborough and *D. desulfuricans* have identical amino acid sequences [44–46], these enzymes are considered to be identical [38, 47]. The IR spectra of the enzymes from *D. vulgaris*, strain Hildenborough [8, 36], *M. elsdenii* [8], *D. desulfuricans* [35, 37] and of hydrogenase I from *C. pasteurianum* [41] also show a high degree of similarity. Other spectroscopic methods such as electron paramagnetic resonance (EPR), electron-nuclear double resonance (ENDOR) and Mössbauer spectroscopy also reveal similar properties of the H-clusters amongs these hydrogenases [38, 40, 48–52]. Therefore it is expected that all these enzymes contain very similar active sites.

## 2.3 Redox and coordination states of the H-cluster

In contrast to the enzymes of *C. pasteurianum* and *M. elsdenii*, which are purified under strict anaerobic conditions [27, 53], the hydrogenases from *D. desulfuricans* can be isolated aerobically [54]. However, the enzyme is inactive ( $\text{H}_{\text{ox}}^{\text{air}}$ ) and needs to be activated under reducing conditions (e.g.  $\text{H}_2$  or artificial reductants). After this treatment

the enzyme is in the reduced state ( $H_{\text{red}}$ ). Recent IR studies reveal that in the reducing state there is no bridging CO ligand [36, 47]. As reported by van Dijk et al. [55], the reductive activation can be reversed only under highly specific conditions.

The reductive activation of [FeFe] hydrogenase from *Desulfovibrio vulgaris* Hildenborough was investigated by Patil et al. using CW EPR spectroscopy [45]. It is known that in the as-isolated enzyme the H-cluster is in an EPR silent state. However, in this state an almost "isotropic"  $g = 2.02$  signal was observed. This signal was thought to be due to traces of an oxidatively damaged F cluster ( $[4\text{Fe}4\text{S}]$ ) and was assigned to a  $[3\text{Fe}-4\text{S}]^+$  cluster. At a potential in the range 0 – -200 mV vs NHE, a rhombic signal appeared characterized by a maximum  $g$ -value  $g_{\text{max}} = 2.06$  (for *D. vulgaris*  $g = (2.06, 1.96, 1.89)$ ) with maximum intensity at about -110mV. This signal was believed to belong to the H-cluster. However, these  $g$ -values are similar to characteristic values of a reduced  $[4\text{Fe}4\text{S}]$  cluster. Therefore, it was concluded, that this signal is due to reduction of the  $[4\text{Fe}4\text{S}]_{\text{H}}$  subcluster.

Upon further reduction of the redox potential, this rhombic signal was replaced by another rhombic signal with  $g$ -values  $g = (2.1, 2.04, 2.0)$ . This is a characteristic signal, observed in all [FeFe] hydrogenases and was assigned to the "oxidized" form of the H-cluster ( $H_{\text{ox}}$ ). It differs fundamentally from EPR spectra of ferredoxin type clusters  $[4\text{Fe}4\text{S}]$ . In the case of *D. desulfuricans*, the  $H_{\text{ox}}$  state could be obtained chemically from the  $H_{\text{red}}$  state by incubation under an inert argon atmosphere. In the case of *C. pasteurianum* the  $H_{\text{ox}}$  state was obtained from the as-isolated state by anoxic oxidation with thionin [48, 56]. The optimal intensity of this signal was observed at a potential of approximately -300 mV. Below -320 mV, the signal was depleted.

Upon complete reduction of the H-cluster an EPR silent state was obtained ( $H_{\text{red}}$ ). Another quite complex EPR signal was obtained at potentials below -250 mV with a maximum intensity at -350 mV. This signal was assigned to the pair of dipolar-coupled  $[4\text{Fe}4\text{S}]^{1+}$  clusters (reduced 'cubanes'). When the *D. vulgaris* enzyme is in the  $H_{\text{red}}$  state, the IR signature of the bridging CO is lost [36]. This was also observed in the *D. desulfuricans* enzyme [35]. The crystal structure of the latter enzyme, reduced using 6 bar  $\text{H}_2$ , suggested that the  $\text{Fe}_d$  atom contained three diatomic ligands, two of which were attributed to end-on bound CO groups. The bond between the formerly bridging CO and  $\text{Fe}_p$  seemed to be absent [35].

An active enzyme is very sensitive to inhibition by CO. In *D. d.* the exchangeable site at  $\text{Fe}_d$  is coordinated by the external CO ligand. Binding of CO to the enzyme in the  $H_{\text{ox}}$



state causes a change in the EPR signal, in which an axial EPR spectrum is observed ( $g_{\perp} = 2.006$ ,  $g_{\parallel} = 2.065$ ). This state can be obtained by incubation of an enzyme in the  $H_{ox}$  state in a CO atmosphere as well as in the  $H_{red}$  state.

From IR investigations it is known that upon light excitation at temperatures between 20 K and 70 K, the external CO ligand can be reversibly removed. At temperatures above 150 K the original rhombic EPR spectrum could be restored [36, 45, 47]. During illumination an additional state ( $L_2$ ) of the H-cluster can be observed. This state is characterized by a rather anisotropic rhombic EPR spectrum with g-values  $g=(2.221, 2.132, 2.048)$  for *D.desulfuricans* [38] and  $g=(2.26, 2.12, 1.89)$  for hydrogenase I from *C. pasteurianum* [51].

Earlier studies of the active site of the [FeFe] hydrogenases from *C. pasteurianum* showed the inhibition by CO strongly influenced the electronic structure. The Mössbauer investigation by Popescu and Münck of  $^{57}\text{Fe}$ -enriched [FeFe] hydrogenase II from *C. pasteurianum* [52] showed two types of  $^{57}\text{Fe}$  HF couplings in the  $H_{ox}$  state at approximately 7.5 MHz and 18 MHz. The weak HF coupling was assigned to the iron nuclei of the  $[4\text{Fe}4\text{S}]_H$  subcluster, while the larger HF coupling assigned to the proximal iron nucleus ( $\text{Fe}_p$ ) of the  $[2\text{Fe}]_H$  subcluster. Inhibition of CO ( $H_{ox}$ -CO) resulted in increased HF coupling constants in the range of 9.5MHz and 25-28 MHz. In this case, the larger HF couplings were assigned to the 'cubane' subcluster (according to the intensities of the lines and the isomeric shift) and small coupling to the  $\text{Fe}_p$  nucleus of the bi-nuclear subcluster. This shift indicate large changes in the electronic structure of the H-cluster upon coordination of an external CO ligand. These results consistent with the HF constants found previously in the same enzyme by Telser et al. [49] using EPR and ENDOR techniques. The distal iron atom in the bi-nuclear subcluster was proposed to be diamagnetic and carrying no spin density. Later, Pereira et al. [60] used Mössbauer spectroscopy for the investigation of the [FeFe] hydrogenase from *Desulfovibrio vulgaris* (Hildenborough). In this H-cluster, HF couplings were found to be consistent to those of Popescu and Münck. In the  $H_{ox}$  state the large coupling was assigned to the  $^{57}\text{Fe}$  in the  $[2\text{Fe}]_H$  subcluster and in the  $H_{ox}$ -CO inhibited state to the  $[4\text{Fe}4\text{S}]_H$  subcluser.

There is still some debate concerning the possible redox states of the bi-nuclear iron cluster in the various catalytic states. Popescu and Münck [52] have concluded (based on the isomeric shift) that the  $[4\text{Fe}4\text{S}]_H$  subcluster remains in the  $[2+]$  state in the  $H_{ox}$ ,  $H_{ox}$ -CO and  $H_{red}$  species. In that work the authors proposed an  $[\text{Fe(II)Fe(III)}]_H$  oxidation state of the bi-nuclear cluster in the  $H_{ox}$  and  $H_{ox}$ -CO states, though the possibility of

## 2.3 Redox and coordination states of the H-cluster

---

[Fe(I)Fe(II)] was not completely excluded. On the other hand, DFT calculations on model systems [57, 58] suggest the following valences of the iron atoms in the [2Fe] subunit of the H-cluster: the fully oxidized, inactive state ( $H_{ox}^{air}$ ) is believed to be Fe(II)Fe(II); the oxidized, active state ( $H_{ox}$ ) is Fe(II)Fe(I) and the reduced, active state ( $H_{red}$ ) is Fe(I)Fe(I). Inorganic model systems of the bi-nuclear subcluster have been prepared [61] which indicate that in the completely reduced state the Fe(I)Fe(I) arrangement is very stable. These findings have also been further confirmed by quantum chemical calculations [62].

Theoretical models of the catalytic cycle have also been recently considered by several groups. Early theoretical studies of the model complexes by Cao and Hall [57] using PDT as a di-thiol ligand have shown that in the completely reduced Fe(I)-Fe(I) form, the structure without bridging CO is slightly more stable than species with bridging CO. A proposed reaction mechanism (catalytic cycle) based on the DFT calculations showed that heterolytic cleavage of  $H_2$  can occur from  $(\mu^2-H_2)Fe(II)-Fe(II)$  via a proton transfer to 'spectator' ligands. Proton transfer to a CN- ligand was found to be thermodynamically favored but kinetically unfavorable over proton transfer to the bridging S of the PDT. Proton migration from a metal hydride to a base (S, CN, or basic protein site) results in a two-electron reduction at the metal centers. This may also explain the requirement of a di-metallic active site and ligand framework which supports low-oxidation-state metals. Coordination of  $H_2O$  to the empty site in the enzyme's diiron active center results in an oxidized inactive  $(H_2O)Fe(II)-Fe(II)$  form. These calculations have shown that reduction of this inactive form releases the  $H_2O$  to provide an open coordination site for  $H_2$ .

In a later study of the DTN containing model complexes by Liu and Hu [58] a hydroxyl ( $OH^-$ ) group bound to the distal iron in  $H_{ox}^{air}$  state was found to be more likely. The optimized structure of the fully reduced state ( $H_{red}$ ) contradicted with previous calculations. It was found that the form with a vacant external site was more consistent with the recent IR studies. In the suggested model, a proton is attached to the N of the DTN. By detailed analysis of the electronic structure of the 2Fe subunit, it was found that the major difference among all the redox states lies in the occupation of a frontier orbital, which is a mixed state between the Fe  $e_g$  and the  $CO_b$   $2\pi$  orbitals ( $e_g-2\pi$  orbital).

A recent theoretical overview of the different states of the H-cluster by Bruschi et al. [59] proposed that electron donor ligands such as  $CH_3S^-$  (which closely mimic the cysteinate residue bridging  $Fe_p$  and the [4Fe4S] cluster in the enzyme) should lead to a structurally similar [Fe(I)Fe(I)] species to that of the  $[2Fe]_H$  subcluster as observed in the fully reduced state of the enzyme (former bridging CO ligand is in the terminal position

of the  $Fe_d$ ). For the oxidized state with [Fe(I)Fe(II)], the species with the terminal CO and the bridging CO were found to be very close in energy. It was suggested that both of these species could take part in the catalytic cycle of the enzyme. Moreover, this investigation shows, that the replacement of PDT with DTN may have an influence on the structural properties of the diiron cluster. However, no conclusion has been drawn so far with respect to this ligand.

## 2.4 Exchange-coupling model of the H-cluster in the paramagnetic states

In order to explain the experimental observation of the  $^{57}\text{Fe}$  HF couplings of the  $[4\text{Fe}4\text{S}]_{\text{H}}$  subcluster, an exchange model has been discussed in the literature. As discussed previously, the  $[4\text{Fe}4\text{S}]_{\text{H}}$  subunit of the H-cluster remains in the 2+ state. Several experimental and theoretical studies were performed on this  $[4\text{Fe}4\text{S}]^{2+}$  cluster. It was found that the ground state of the cluster comprises two valence-delocalized pairs, with spin  $S_{1,2} = S_{3,4} = 9/2$  (see figure 2.4). The two pairs are antiferromagnetically coupled by Heisenberg-Dirac-VanVleck (HDVV) exchange  $J_{\text{cube}}$ , yielding a diamagnetic ground state ( $S_{\text{cube}} = 0$ ) and a triplet ( $S_{\text{cube}} = 1$ ) first excited state.

Bominaar and co-workers [63] have developed an electronic model that explains the experimentally observed  $^{57}\text{Fe}$  HF interactions of all iron nuclei in the  $S = 5/2$  state of the exchange-coupled siroheme- $[4\text{Fe}4\text{S}]^{2+}$  chromophore in oxidized *E. coli* sulfite reductase. Later, Belinsky [64] reviewed this model and adopted a simplified version to describe the  $S = 1/2$  state of NO-complexed sulfite reductase. Xia et al. [65] then applied this theory to explain the observed  $^{57}\text{Fe}$  HF couplings from the  $[4\text{Fe}4\text{S}]^{2+}$  found in the Ni-activated R-subunit of carbon monoxide dehydrogenase from *Clostridium thermoaceticum*.

The same principles were applied to the active [FeFe]hydrogenase by Popescu and Münck in order to explain the observation of the  $^{57}\text{Fe}$  HF couplings from the  $[4\text{Fe}4\text{S}]_{\text{H}}$  subcluster in the case of the  $\text{H}_{\text{ox}}$  and  $\text{H}_{\text{ox}}\text{-CO}$  state [52]. The coupling of the additional spin ( $S_5$ ) with coupling constant  $j$  mixes the  $S_{\text{cube}} = 1$  state of the 'cubane' with the ground states  $S_{\text{cube}} = 0$  of the 'cubane'. This gives rise to isotropic  $^{57}\text{Fe}$  HF couplings of the  $[4\text{Fe}4\text{S}]_{\text{H}}$  whose values depend on the  $j/J_{\text{cube}}$  ratio.

The calculations based on the work of Belinsky [64], result in the following expression for the HF constants of  $^{57}\text{Fe}$  nuclei of the  $[4\text{Fe}4\text{S}]_{\text{H}}$  [65]:

$$A_{1,2(3,4)} = \left\{ \frac{[1 - (1 - x)/\Gamma]}{6} + (-) \frac{33 x}{2 \Gamma} \right\} a \quad (2.1)$$

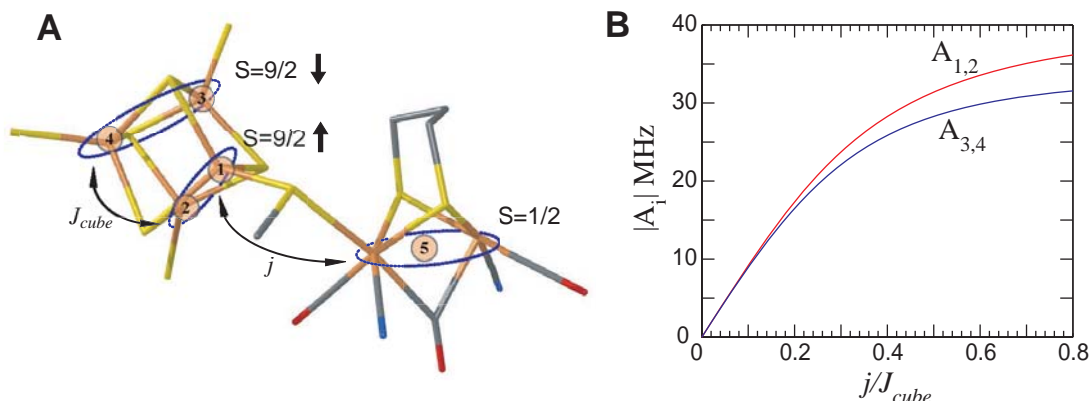


**Figure 2.4:** **A.** Scheme of exchange interactions of the H-cluster. Two valence-delocalized Fe(II)-Fe(III) pairs in the  $[4\text{Fe}4\text{S}]_{\text{H}}$ , each having a spin  $S_{\text{pair}} = 9/2$ , anti-ferromagnetically coupled by HDVV exchange  $J_{\text{cube}}$ . This results in a diamagnetic ground state  $S = 0$ . Spin coupling of the  $[2\text{Fe}]_{\text{H}}$  ( $S_{\text{H}} = 1/2$ ) to the closest iron atom of the 'cubane' (1) admixes wavefunctions of the first excited state  $S = 1$  of the  $[4\text{Fe}4\text{S}]_{\text{H}}$  to the ground state, giving rise to effective spin density on the irons of the 'cubane'. **B.** Dependence of the  $^{57}\text{Fe}$  hfcc's on the strength of the exchange interaction constants  $j$  and  $J_{\text{cube}}$  according to equation (2.1).

where  $\Gamma = [1 - 2x + 100x^2]^{1/2}$ ,  $x = j/4J_{\text{cube}}$  and  $a$  is the intrinsic HF tensor of the individual iron sites of the  $[4\text{Fe}4\text{S}]_{\text{H}}$ , considered to be isotropic in this model. According to experimental studies of the  $[4\text{Fe}4\text{S}]^{2+}$  cluster the value of  $J_{\text{cube}}$  was estimated to be about  $200 \text{ cm}^{-1}$  [65].

Figure 2.4 shows the dependence of the isotropic component of the  $^{57}\text{Fe}$  hfcc's of the 'cubane' on the  $j/J_{\text{cube}}$  ratio. Analysis of the HF interaction of the valence-delocalized pairs in  $[3\text{Fe}4\text{S}]^0$ ,  $[4\text{Fe}4\text{S}]^{2+,3+}$  clusters suggest  $a = -22 \text{ MHz}$  [66]. Described theory predicts alternating signs of the HF coupling constants for two Fe(II)-Fe(III) pairs which have also been confirmed by Mössbauer studies of the H-cluster in [FeFe]-hydrogenase II from *C. pasteurianum* (*C.p.II*) [52].

---

# 3

## Motivation of the work

---

During the last decade, much interest has been focused towards the development of alternative energy carriers. Hydrogenases are ideal candidates to be modeled in order to design hydrogen producing systems. Artificial hydrogenase could then be coupled to photosynthetic model systems such as Ru-complexes [1, 67]. Therefore, it is very important to understand the mechanism by which hydrogenases produce molecular hydrogen.

So far, knowledge about the catalytic cycle is quite limited. Recently, several crystal structures of the [FeFe]-hydrogenase have been solved, providing structural details of the active site. Although some controversies still remain unresolved, such as di-thiol moiety of the  $[2\text{Fe}]_{\text{H}}$ , which is of a key importance for modeling the catalytic mechanism. Only a few spectroscopic studies have been performed, providing some basic information about the electronic structure of the active states of the H-cluster.

The main goal of the study presented here is to resolve the electronic structure of the H-cluster in its EPR active states ( $\text{H}_{\text{ox}}\text{-CO}$  and  $\text{H}_{\text{ox}}$ ) using advanced EPR methods. For this investigation an [FeFe] hydrogenase from *D. desulfuricans* was used.

The determination of the nuclear spin interactions from  $^{57}\text{Fe}$ ,  $^{13}\text{C}$ ,  $^{14}\text{N}$  and  $^1\text{H}$  can provide information about the distribution of spin density over the H-cluster. Investigation of the  $^{57}\text{Fe}$  HF couplings has practical importance since it provides first hand information about the electronic structure of the H-cluster via the metal nuclei. Another probe is  $^{14}\text{N}$ , which gives more specific information about the spin density on the cyanide ligands in the  $[2\text{Fe}]_{\text{H}}$  subcluster. Using  $^{14}\text{N}$  spectroscopy it may be also possible to resolve whether a nitrogen is present in the di-thiol ligand in the  $[2\text{Fe}]_{\text{H}}$  subcluster. Additional information can be gained from specific labeling of the CO ligands with  $^{13}\text{C}$ , which is very important for understanding the role of the external CO binding. For this purpose EPR techniques (both continuous wave (CW) and pulse) are very convenient tools. In contrast to Mössbauer spectroscopy which suffers from the additional signals from the  $[4\text{Fe}4\text{S}]$  clusters, EPR spectroscopy focused exclusively the active center, which in general.

Comparison of previous studies of the [FeFe]-hydrogenases from other organisms may

---

reveal possible differences of their active sites.

It is known that inhibition by CO leads to large changes in the electronic structure of the H-cluster (see above). Light induced removal and changes of the ligands is probably related to the dissociation processes that happen in the native enzyme. Therefore it is important to investigate photo-dissociation processes in detail. Study of the photo-dissociated states can provide information about the intermediate states of the the active site during the catalytic reaction.

Resolving the electronic structure of the light-induced forms of the H-cluster by pulse EPR may help to understand the intra-cluster exchange coupling mechanism. Specific information about the role of the CO moiety may be gained by direct comparison of the spectroscopic data, with that of chemically prepared states ( $H_{ox}$ -CO and  $H_{ox}$ ).

---

# 4

## EPR spectroscopy

---

### 4.1 Spin Hamiltonian

#### 4.1.1 The Spin Hamiltonian approach

The spin Hamiltonian approach is a quite common method used for the interpretation of spectroscopic data from EPR and ENDOR spectroscopy. A Hamiltonian is called *spin Hamiltonian* when the true Hamiltonian of the system is replaced by an effective Hamiltonian, containing only spin operators. The spin Hamiltonian formalism is not actually a full physical model, its purpose is only to accurately describe and parameterize 'interactions' that have influence on the magnetic resonance spectra. It describes the EPR behavior of the systems without going into the physical details [68, 69]. In many cases, the effective values obtained from such analysis are not directly related to the physical properties of the investigated system. Then only in cooperation with theoretical calculations it is possible to resolve specific properties of the system.

The spin Hamiltonian can be split into terms, responsible for different types of interactions. There is a wide variety of interactions which could be taken into account, however, here only those, which are directly related to the current work will be discussed. An extensive introduction into the theory of the spin Hamiltonian approach can be found in [68, 70–72]

Within this study several contribution to the Spin Hamiltonian were considered:

$$\mathcal{H} = \mathcal{H}_{ze} + \mathcal{H}_{zn} + \mathcal{H}_{hf} + \mathcal{H}_q \quad (4.1)$$

In this equation the  $\mathcal{H}_{ze}$  and  $\mathcal{H}_{nz}$  terms represent the interaction of the electronic and nuclear spins with the external magnetic field (so called Zeeman interaction).  $\mathcal{H}_{hf}$  is the interaction term between electron and nuclear spin (hyperfine interaction). For nuclear spins  $I > 1/2$  the quadrupole interaction  $\mathcal{H}_q$  term has to be considered as well.

#### 4.1.2 Zeeman interaction

Classically, the energy of the interaction of a magnetic moment  $\vec{\mu}$  with a constant magnetic field  $\vec{B}$  can be written as  $E = -\vec{\mu}\vec{B}$ . In quantum mechanical systems, the

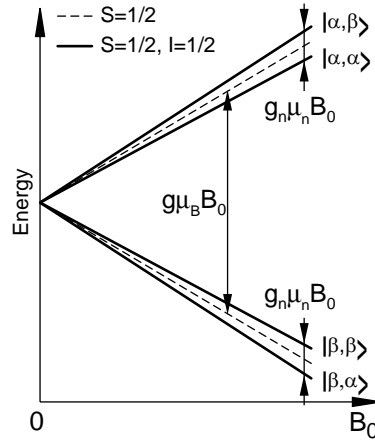


**Figure 4.1:** Energy level scheme for the system of one electron spin  $S = 1/2$  and one nucleus with  $I = 1/2$  as a dependence on the external magnetic field.

magnetic moment has to be substituted by its operator. The energy of the free electron in magnetic field can be expressed in terms of the spin Hamiltonian formalism by the following expression:

$$\mathcal{H}_{ze} = g_e \mu_B \vec{\mathbf{S}} \cdot \vec{\mathbf{B}}_0, \quad (4.2)$$

where  $g_e$  is the  $g$ -factor of the free electron and  $\mu_B$  is the Bohr magneton. If the magnetic field defines the  $z$ -direction, then the Hamiltonian simplifies to

$$\mathcal{H}_{ze} = g_e \mu_B \mathbf{S}_z B_0 \quad (4.3)$$

For the  $S = 1/2$  system, the solution of the eigenproblem will result in two energy levels separated by

$$\Delta E = g_e \mu_B B_0 \quad (4.4)$$

However, in real systems it is quite rare that the resonance is exactly at  $g_e$  (i.e. satisfying  $h\nu = g_e \mu_B B_0$ ). Moreover, it is quite common, that the resonance conditions are changing with changing orientation of the molecule along the external magnetic field. Therefore, an effective value  $g$  has been introduced, which satisfies  $h\nu = g \mu_B B_0$ . Here we will follow the common terminology and call this  $g$  a ' $g$ -tensor'. The deviation of the principal values from the  $g_e$  value of the free electron and the orientation dependence of the Zeeman interaction is originating from the spin orbital interaction [69, 72]. This effect is described by the following Hamiltonian

$$\mathcal{H}_{ze}^* + \mathcal{H}_{LS} = \mu_B B_0 (\mathbf{L} + g_e \mathbf{S}) + \lambda \mathbf{L} \mathbf{S} \quad (4.5)$$

In this case, the Zeeman term  $\mathcal{H}_{ze}^*$  includes the orbital angular momentum ( $\mathbf{L}$ ). The term  $\mathcal{H}_{LS} = \lambda \mathbf{L}\mathbf{S}$  is the spin-orbital interaction with the spin-orbital coupling constant  $\lambda$ . Using second order perturbation theory one can obtain the  $g$ -tensor in the form [72]

$$\mathbf{g} = g_e \mathbf{1} + 2\lambda \mathbf{\Lambda}, \quad (4.6)$$

where  $\mathbf{\Lambda}$  is a symmetric tensor, whose elements are described by

$$\Lambda_{ij} = \sum_{n \neq 0} \frac{\langle \psi_0 | L_i | \psi_n \rangle \langle \psi_n | L_j | \psi_0 \rangle}{\varepsilon_0 - \varepsilon_n}. \quad (4.7)$$

Here,  $\psi_0$  is the wave function of the ground state occupied by the unpaired electron with energy  $\varepsilon_0$  and  $\psi_n$  corresponds to the  $n^{\text{th}}$  excited state with energy  $\varepsilon_n$ .

The Zeeman interaction of a nuclear spin  $\mathbf{I}$  with the static magnetic field  $B_0$  is described by the nuclear Zeeman interaction

$$\mathcal{H}_{zn} = -g_n \mu_n B_0 \mathbf{I} \quad (4.8)$$

where  $g_n$  is the nuclear  $g$ -factor and  $\mu_n$  is the nuclear magneton. The spin quantum number  $I$  and the nuclear  $g_n$  factor are intrinsic properties of a nucleus.

### 4.1.3 Hyperfine interaction

The hyperfine interaction (HF) between the electron spin and a nuclear spin is described by the Hamiltonian

$$\mathcal{H}_{hf} = \mathbf{S}\mathbf{A}\mathbf{I} = \mathcal{H}_f + \mathcal{H}_{dd} \quad (4.9)$$

where  $\mathbf{A}$  is the HF tensor, which can be split into two terms: the isotropic (mostly Fermi contact) interaction ( $\mathcal{H}_f$ ) and the electron-nuclear dipole-dipole coupling ( $\mathcal{H}_{dd}$ ). The isotropic interaction can be written as

$$\mathcal{H}_f = a_{iso} \mathbf{S}\mathbf{I}, \quad (4.10)$$

$$a_{iso} = \frac{2}{3} \frac{\mu_0}{h} g_e \beta_e g_n \beta_n |\psi_0(0)|^2 \quad (4.11)$$

where,  $a_{iso}$  is the isotropic hyperfine coupling constant and  $|\psi_0(0)|^2$  is the electron spin density at the nucleus. In cases, where the unpaired electron resides in a  $p$ ,  $d$  or  $f$  orbital, the isotropic HF coupling may also be significant due to configuration interaction or spin

## 4.1 Spin Hamiltonian

---

polarization mechanisms [72, 73]. The anisotropic, or electron-nuclear dipole-dipole coupling is given by

$$\mathcal{H}_{dd} = \frac{\mu_0}{4\pi\hbar} g_e \beta_e g_n \beta_n \left[ \frac{(3\mathbf{S}\mathbf{r})(\mathbf{r}\mathbf{I})}{r^5} - \frac{\mathbf{S}\mathbf{I}}{r^3} \right], \quad (4.12)$$

where  $\mathbf{r}$  is the vector connecting the electron and nuclear spin. Integration over the spatial electron distribution, yields the following Hamiltonian:

$$\mathcal{H}_{dd} = \mathbf{S}\mathbf{T}\mathbf{I} \quad (4.13)$$

where  $\mathbf{T}$  is the dipolar coupling tensor. If this coupling considers only the wave-function of the ground state,  $\mathbf{T}$  is a traceless symmetric tensor with elements:

$$T_{ij} = \frac{\mu_0}{4\pi\hbar} g_e \beta_e g_n \beta_n \left\langle \psi_0 \left| \frac{3r_i r_j - \delta_{ij} r^2}{r^5} \right| \psi_0 \right\rangle \quad (4.14)$$

in which  $\delta_{ij}$  is the Kronecker symbol ( $\delta_{ij} = 0$  for  $i \neq j$  and  $\delta_{ij} = 1$  for  $i = j$ ).

### 4.1.4 Quadrupole interaction

Nuclei with a spin larger than 1/2 are distinguished by a non-spherical charge, which can be described by a nuclear electronic quadrupole moment  $Q$ . Using the spin Hamiltonian approach, this interaction can be written as an interaction of the nuclear spin with itself:

$$\mathcal{H}_q = \mathbf{I}\mathbf{P}\mathbf{I} \quad (4.15)$$

where  $\mathbf{P}$  is the traceless nuclear quadrupole tensor. In the principal axis system of  $\mathbf{P}$  the Hamiltonian  $\mathcal{H}_q$  can be written to first order as

$$\mathcal{H}_q = P_x I_x^2 + P_y I_y^2 + P_z I_z^2 = \frac{e^2 q Q}{4I(2I-1)\hbar} \left[ (3I_z^2 - I(I+1)^2) + \eta (I_x^2 - I_y^2) \right] \quad (4.16)$$

where  $eq$  is the electric field gradient and  $\eta = (P_y - P_x)/P_z$  is the asymmetry parameter with  $|P_z| \geq |P_y| \geq |P_x|$  and  $0 \leq \eta \leq 1$ . As it follows from (4.16), the largest value of the quadrupole tensor is given by

$$P_z = e^2 q Q / 2I(2I-1)\hbar. \quad (4.17)$$

It is quite common that only these two quantities are given:  $K = e^2 q Q / 4\hbar$  and  $\eta$ . In a molecule the magnitude of the electric field gradient at the nucleus can be written as

$$eq = -e \sum_j \left\langle \psi_j \left| \frac{3 \cos^2 \theta - 1}{r^3} \right| \psi_j \right\rangle n_j + e \sum_k Z_k \left( \frac{3 \cos^2 \theta_k - 1}{R_k^3} \right), \quad (4.18)$$

where the first term represents the electronic contribution to the electric field gradient, with  $\psi_j$  referring to the occupied molecular orbital and  $n_j$  is the number of electrons occupying the  $j^{\text{th}}$  orbital. The second term describes contribution of the nuclei with charges  $Z_k$ . In order to calculate electronic field gradient, all core and valence electrons must be considered.

## 4.2 EPR methods

### 4.2.1 Measurement of EPR spectra

In the continuous wave (CW) EPR experiments, a dependence of the electron paramagnetic resonance effect is observed as a function of external magnetic field upon continuous irradiation with a microwave frequency. Resonance occurs when the energy difference between two electronic state  $m_{S1}$  and  $m_{S2}$  (depending on the magnetic field) equals the energy of the MW field quantum ( $h\nu$ ). The magnitude of the EPR effect depends on the difference in the population of these levels. It is common, that lock-in detection and a field modulation technique are used to obtain the spectra [74].

When on resonance, two major concurrent effects are responsible for the strength of the signal, the absorption of the MW power that drives the transitions, and the relaxation of the excited spin levels. In a CW EPR experiment, the signal can be saturated if the rate of absorption, which is proportional to the microwave power, is higher than the relaxation rate. Lowering the temperature should increase the difference in populations and therefore increase the EPR signal. On the other side, at low temperature relaxation rates are decreases, which could lead to saturation at lower MW power. Since the relaxation properties are strongly dependent on the particular system, optimum conditions can be different from sample to sample.

In the case, that the electron Zeeman interaction can be described in terms of an isotropic  $g$ -value (all components of the  $g$ -tensor are equal) and no other interactions are present in the system, the CW EPR spectrum is characterized by one line at frequency  $\nu_S$  (figure 4.3), the width depends on relaxation properties [72]. If a HF interaction is present in the system, this line splits into  $(2I + 1)$  lines of equal amplitude. This splitting directly relates to the HF coupling. For the system ( $S = 1/2, I = 1/2$ ) in which the nucleus experiences an isotropic HF interaction  $a_{iso}$  (see eq. 4.10), the position of the lines in the EPR spectrum can be expressed (in first order approximation) as:

$$\nu_{EPR} = |\nu_S \pm a_{iso}/2| \quad (4.19)$$

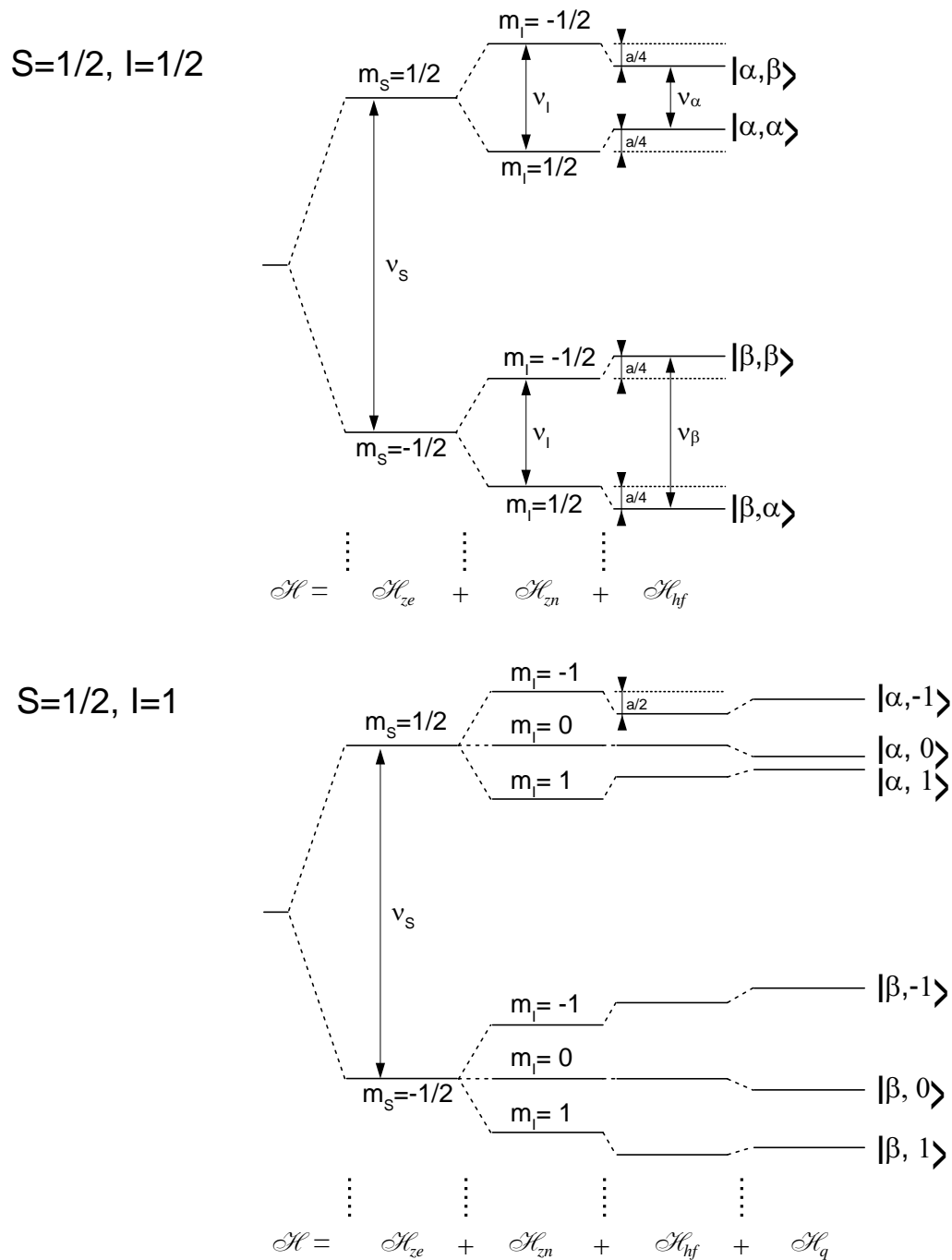


**Figure 4.2:** Energy level scheme in the case of electronic spin  $S = 1/2$  interacting with nucleus either with  $I = 1/2$  (top) or  $I = 1$  (bottom)

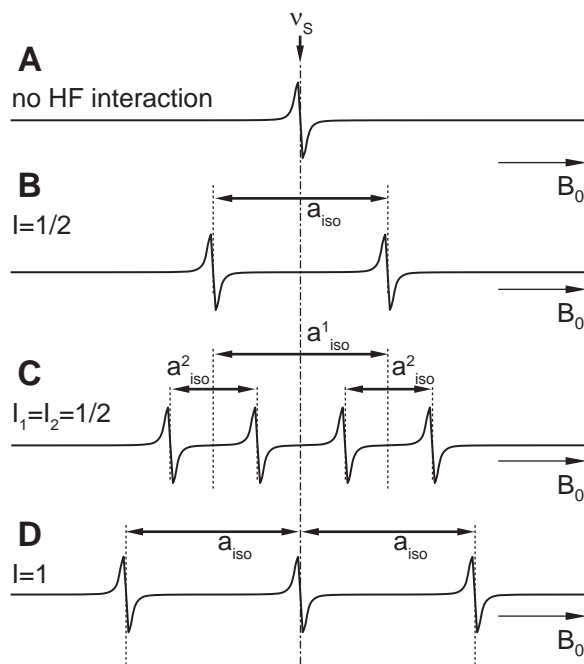


**Figure 4.3:** Simulation of the effect of HF interaction on CW EPR spectra in the case of an isotropic  $g$ -tensor ( $g_{iso}$ ) and an isotropic HF coupling  $a_{iso}$  for the case of one nucleus  $I = 1/2$  (**B**), two nuclei  $I_1 = I_2 = 1/2$  (**C**) and  $I = 1$  (**D**). The top trace represents the spectrum of a system without any coupled magnetic nuclei. In all cases the electron spin is  $S = 1/2$ .

As mentioned in the previous section, in the case of a nuclear magnetic spin  $I \geq 1$ , the quadruple interaction has to be taken into account. However, as it follows from figure 4.2, the quadruple interaction acts in the same way on both  $m_S$  manifolds. Therefore, if second order effects are not taken into account, the quadrupole interaction has no effect on the EPR spectrum.

In the case of  $g$ -anisotropy, the resonance conditions and consequently the positions of the lines in a spectrum depend on the orientation of the system along the external magnetic field. For the case of a frozen solution, an EPR spectrum would represent an assembly of EPR spectra, obtained from all possible orientations. Typical shapes of the EPR spectra of the frozen solution are shown in figure 4.4.

Most of the work, presented here was done using pulse EPR methods. In pulse EPR spectroscopy the response of the spin system on one or more microwave (MW) pulses is detected. One of the methods of obtaining an absorption-like EPR spectrum is the detection of the Electron Spin Echo (ESE) intensity after a sequence of MW pulses [69,

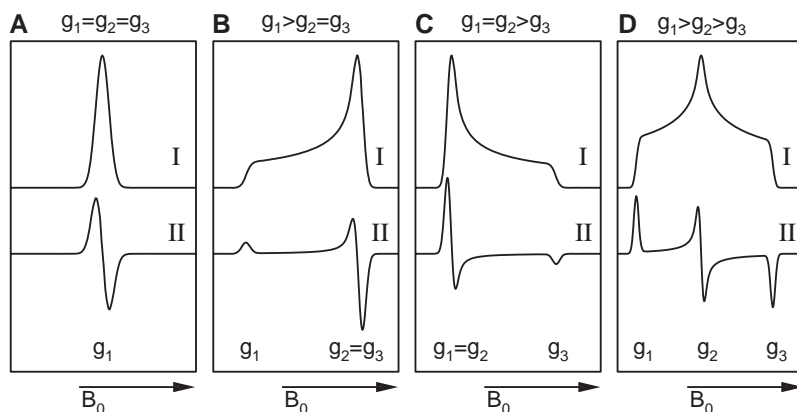


**Figure 4.4:** Absorption (I) and first derivative (II) EPR spectra in the case of an isotropic (A), axial (B,C) and rhombic (D) g-tensor

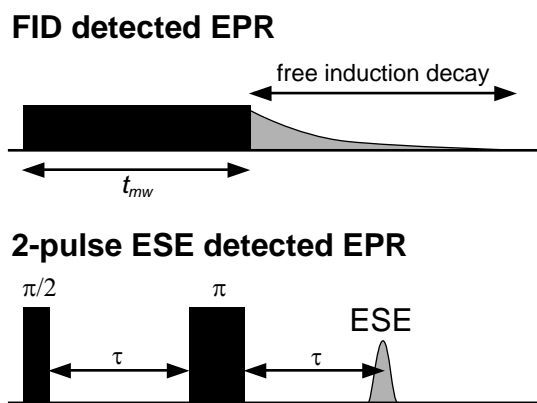


**Figure 4.5:** FID detected and 2-pulse ESE detected EPR pulse sequences.

75, 76] (figure 4.5). However, the EPR spectra obtained by this method can contain some distortions due to field dependent modulations originating from interactions with the nuclear spins. Polarization (the difference in population of the levels) at a particular magnetic field can be measured by integration of the free-induction decay (FID) after a 'soft'  $\pi/2$  MW pulse [69]. When the applied MW pulse is rather long (in the current study  $t_{mw} = 500 - 1000$  ns was used), the obtained spectra are essentially free of nuclear modulations. Therefore, detection of the FID while scanning the external magnetic field provides an EPR spectrum, similar to the original absorption spectrum.

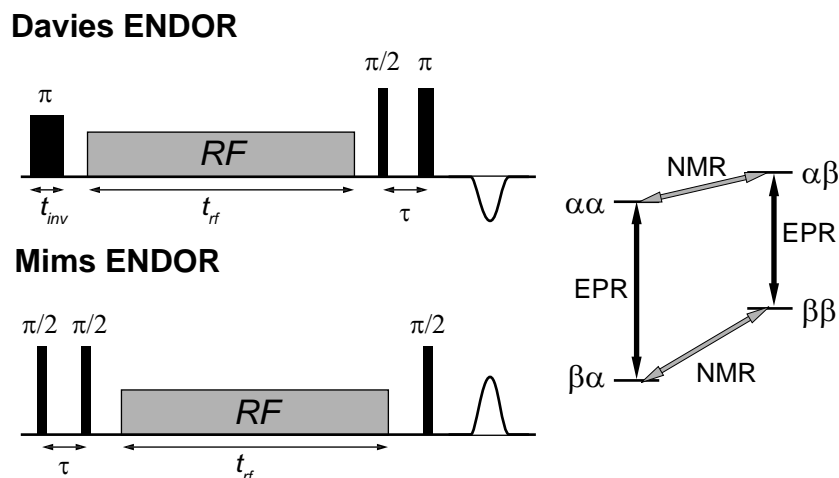


**Figure 4.6:** Basic pulse sequences (left) used for obtaining ENDOR spectra: Mims ENDOR and Davies ENDOR and energy levels scheme (right) for system  $S = 1/2$  and  $I = 1/2$  with marked transitions, excited by MW and RF pulses.

#### 4.2.2 ENDOR

If the HF interaction is smaller than the EPR linewidth, it will only result in a broadening of the EPR line [72]. In this case the limited resolution of EPR spectra (especially in frozen solution) often prevents the determination of HF tensors. Higher resolution can be obtained by application of advanced EPR techniques like electron-nuclear double resonance (ENDOR) spectroscopy [69, 70, 77]. This is a double resonance technique in which NMR transitions are observed by monitoring the intensity of an EPR transition (see figure 4.6). In an ENDOR experiment, the radio frequency is scanned, while other parameters are kept constant.

The two main pulse ENDOR techniques [78, 79] are called Mims ENDOR [80] and Davies ENDOR [81] after their inventors. The Mims ENDOR sequence is derived from a 3-pulse ESEEM sequence (see below). It starts with the preparation sequence of two non-selective  $\pi/2$  MW pulses, spaced by  $\tau$ , which creates a grating polarization pattern. During the mixing period, the polarization is changed by selective RF pulse and then recorded as a function of the RF frequency via a stimulated ESE. The efficiency of the Mims experiment depends on  $\tau$  and the value of the HF coupling. For the case of an isotropic HF coupling ( $a_{iso}$ ) the ENDOR efficiency is given by following expression [69, 79]:

$$F_{mims} = \frac{1}{4} (1 - \cos(a_{iso} \tau)) \quad (4.20)$$

In the Davies ENDOR sequence, the first MW  $\pi$ -pulse selectively inverts the polarization of one of the EPR transition. The following application of an RF pulse resonant with one of the NMR transitions changes this polarization, which is then detected by measuring changes of the intensity of the ESE after the sequence of two MW pulses. In contrast to the Mims-ENDOR sequence, in the Davies experiment it is important to apply selective inversion pulses. Therefore, the efficiency of the Davies ENDOR sequence depends on the selectivity parameter  $\eta_S = a t_{inv}/2\pi$ , where  $a$  is the orientation dependent HF coupling constant. In the case, if  $\eta_S \leq 1$  both transitions are excited, which leads to a decrease of ENDOR effect. The absolute ENDOR intensity as a function of the selectivity parameters  $\eta_S$  is described by the formula [69, 79]:

$$V(\eta_S) = V_{max} \frac{\sqrt{2}\eta_S}{\eta_S^2 + 1/2} \quad (4.21)$$

As it follows from formula (4.20), in the Mims ENDOR spectra peaks satisfying  $\tau = (2n + 1)\pi/a$  would have maximum amplitude and those which are so, that  $\tau = 2n\pi/a$  will be completely suppressed. Thus, for strong and quite anisotropic HF coupling the Mims ENDOR spectrum can have 'blind-spots' in the powder pattern for those cases where the components of the ENDOR spectrum are satisfying  $\tau = 2n\pi/a$ . Therefore in this case the Davies ENDOR sequence is preferable in order to obtain correct lineshapes. On the other hand, in the Davies ENDOR experiments weak couplings will be suppressed due to excitation of both electronic transitions by the inversion MW pulse (see eq. 4.21). Hence, for the detection of weak HF couplings, Mims ENDOR is preferable.

### 4.2.3 TRIPLE

TRIPLE (or double ENDOR) originally described for CW ENDOR experiments [82, 83], is an extension of the ENDOR technique in which two RF pulses are applied at different frequencies [79, 84]. The pulse sequence for the TRIPLE experiment can be derived from both the Mims or Davies ENDOR sequence by adding a second RF pulse right after the first one. Since only the Davies TRIPLE sequence has been used in the present work, the term 'TRIPLE' should in the following be associated with this type of experiment.

Figure 4.7 presents an explanation of double RF resonance for the Davies TRIPLE sequence, for the case of  $S = 1/2$ ,  $I_1 = 1/2$ ,  $I_2 = 1/2$  with HF constants  $a_{iso}^1 > a_{iso}^2 > 0$  in the weak coupling case and with  $\nu_I < 0$ . As for the Davies ENDOR sequence, the first selective MW pulse inverts the polarization of one electron spin transition, for instance

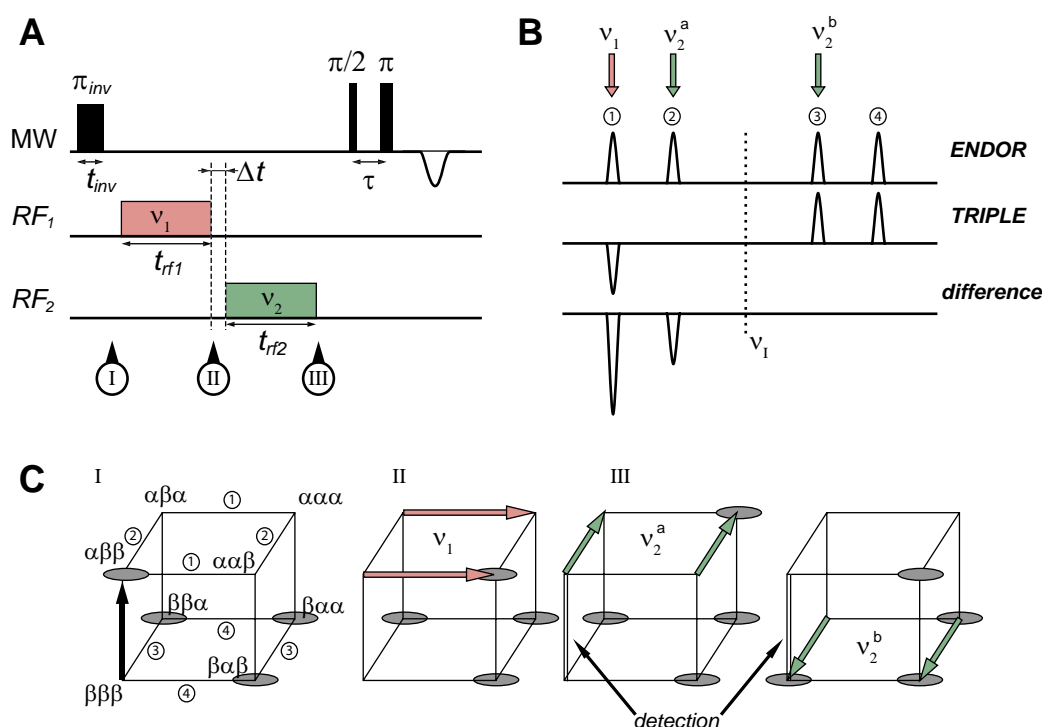


**Figure 4.7:** TRIPLE pulse sequence (A), schematic ENDOR and TRIPLE spectra (B) and energy level schemes showing changes in population of levels during the pulse sequence (C). Considered system:  $S = 1/2$ ,  $I_1 = 1/2$ ,  $I_2 = 1/2$ ;  $a_{iso}^1 > a_{iso}^2 > 0$ ;  $|2\nu_I| > a_{iso}^{1,2}/2$  and  $g_n > 0$ . **A**, TRIPLE pulse sequence, derived from Davies ENDOR sequence. **B**, ENDOR spectrum (top), TRIPLE spectrum (middle), obtained with exciting  $|\alpha\beta\beta\rangle \longleftrightarrow |\alpha\alpha\beta\rangle$  transition by first RF pulse ( $\nu_1$ ) and difference TRIPLE spectrum (bottom). The gray circles in the energy schemes mark most populated levels.

$|\beta\beta\beta\rangle \longleftrightarrow |\alpha\beta\beta\rangle$ . In the following the RF pulse with frequency  $\nu_1$  changes the polarisation of the NMR transition  $|\alpha\beta\beta\rangle \longleftrightarrow |\alpha\alpha\beta\rangle$ . In the absence of a second RF pulse (or if it is not resonant with any transitions), the detected signal would be exactly as in an Davies ENDOR experiment. Therefore the 'baseline' for the TRIPLE spectrum is the intensity of the ENDOR signal at frequency  $\nu_1$ .

If the second RF pulse during the scan is resonant with the NMR transition of the other nucleus, but at the same electron spin manifold  $|\alpha\alpha\beta\rangle \longleftrightarrow |\alpha\alpha\alpha\rangle$  (case  $\nu_2^a$  in figure 4.7) it will have no influence on the observed transition  $|\beta\beta\beta\rangle \longleftrightarrow |\alpha\beta\beta\rangle$ . Therefore, the signal will be the same as the 'baseline'. If the second RF pulse initiates the NMR transition of the second nucleus, corresponding to the other spin manifold  $|\beta\beta\alpha\rangle \longleftrightarrow |\beta\beta\beta\rangle$  (case  $\nu_2^b$ ) it restores the initial polarization of the detected transition, therefore a positive signal is

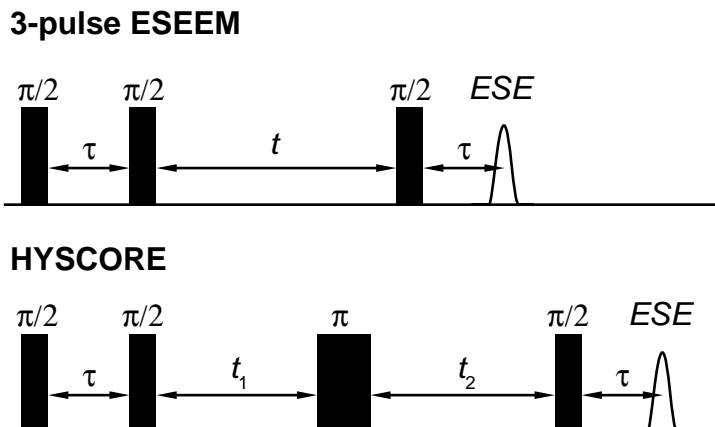


**Figure 4.8:** 3-pulse ESEEM and HYSCORE (4-pulse ESEEM) sequences. In the first case 1D ESEEM decay can be obtained by recording changes in ESE signal with increasing  $t$  delay. 2D HYSCORE spectrum obtained by varying delays  $t_1$  and  $t_2$ .

expected. The same effect will be observed in the case of excitation the  $|\beta\alpha\beta\rangle \longleftrightarrow |\beta\beta\beta\rangle$  transition by the first RF pulse.

If both RF pulses have the same frequency ( $\nu_2 = \nu_1$ ), then the second RF pulse would cancel effect of the first RF pulse. Thus the ESE signal will be the same as in the case of absence of any RF pulses: inversed ESE.

The most convenient way to observe the TRIPLE effect is to subtract the original ENDOR spectrum from the TRIPLE spectrum. As shown in figure 4.7,**B**, the difference TRIPLE spectrum shows only those peaks, which belong to NMR transitions of the same electron spin manifold. If two HF couplings would have different signs, these two peaks would appear at different sides of the nuclear Larmor frequency in the difference TRIPLE spectrum. Therefore, this method is very useful for the determination of relative signs of the HF couplings.

#### 4.2.4 ESEEM and HYSCORE

Electron spin echo envelope modulation (ESEEM) is another technique for studying hyperfine and nuclear quadrupole interactions in solids, which requires only MW pulses [69, 75, 76]. ESEEM techniques are particularly advantageous for the investigation of nuclear frequencies in the low frequency region, such as for  $^{57}\text{Fe}$  and  $^{14}\text{N}$  nuclei due to their smaller gyromagnetic ratio.

The pulse sequence of three pulse ESEEM is shown in figure 4.8. A non-selective

$\pi/2$  pulse excites electron spin coherences which evolve during the time  $\tau$ . The second non-selective  $\pi/2$  pulse transfers the electron spin coherences partially to nuclear spin coherence evolving during the interval  $t$ , which is varied in the experiment. A transfer of the nuclear spin coherence back to the electron spin coherence is achieved by the third pulse. After the interval  $\tau$  a "stimulated" echo with an intensity modulated as function of  $t$  (and  $\tau$ ) is detected. HYSCORE is another method of ESEEM spectroscopy, which is a two-dimensional (2D) technique and is derived from the 3-pulse ESEEM sequence [69, 85]. The correlation of the NMR transitions frequencies in one  $m_S$  manifold to those in the other manifold in a 2D experiment improves the resolution and provides information which can not be extracted from a 1D ESEEM spectrum. In the study presented here, HYSCORE experiments have become a standard method for the measurements of relatively weak spin interactions of  $^{13}\text{C}$ ,  $^{14}\text{N}$  and  $^{57}\text{Fe}$  nuclei.

As in the case of 3-pulse ESEEM, nuclear spin coherence is created in the preparation period and evolves during time  $t_1$ . Then a mixing  $\pi$  pulse is applied which interchanges nuclear spin coherence between electron spin manifolds. The nuclear spin coherences are evolves in the second free period (during time  $t_2$ ) and is then detected via changes in the amplitude of the stimulated ESE signal. 2D HYSCORE modulation patterns can be obtained by varying times  $t_1$  and  $t_2$  simultaneously.

Applying the four pulses during a HYSCORE sequence leads to the appearance of unwanted primary and stimulated echoes as well as FIDs. In total, 20 echoes can appear. Elimination of the unwanted echoes requires a 16-step phase cycling of the 3 pulses [69]. However, in most of the cases FIDs and anti-echo pathways are quite small. Then only a four-step phase cycling of the last two MW pulses may be applied instead:

$\pi/2$	$\pi/2$	$\pi$	$\pi/2$	detection
x	x	x	x	y
x	x	x	-x	-y
x	x	-x	x	y
x	x	-x	-x	-y

Using 2D Fast Fourier transformation, a 2D HYSCORE spectrum can be obtained. The cross peaks are not the same for all quadrants of the 2D spectrum, see fig. 4.9. For the weak-coupling case ( $|\nu_I| > |A/2|$ ), where  $\nu_\alpha$  and  $\nu_\beta$  have the same sign, cross peaks appear in the first (++) quadrant, while in the case of strong HF coupling ( $|\nu_I| < |A/2|$ ), peaks

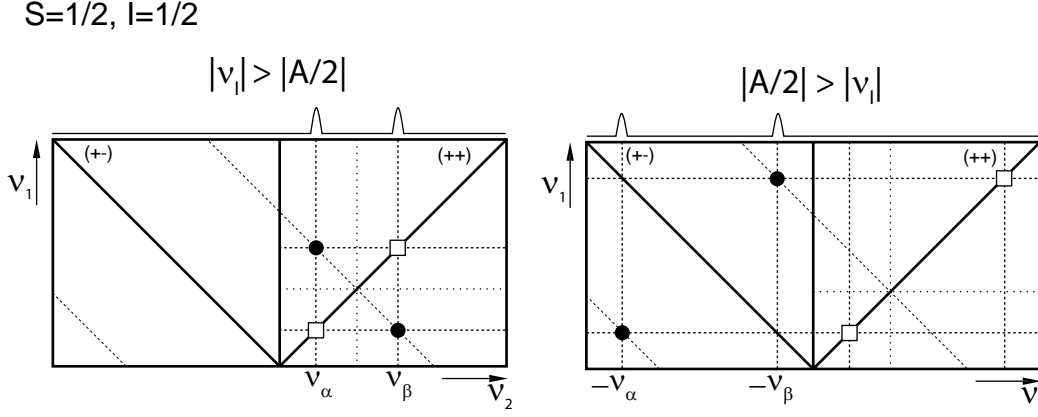


**Figure 4.9:** Schematic representation of HYSORE spectra in the case of weak and strong HF coupling. Filled circles represent 'wanted' cross-peaks and empty squares represent possible diagonal peaks due to non-ideality of the MW pulses. For intermediate case (not shown here) cross peaks can appear in both quadrants.

appear in the second (+ -)quadrant.

Taking into account only the modulation part (no relaxation effects) and assuming ideal pulses, one can derive the following modulation formula for the arbitrary nuclear spin coupled to the electronic spin  $S = 1/2$  [69, 86, 87]:

$$\begin{aligned}
 E(\tau, t_1, t_2) &= E_\alpha(\tau, t_1, t_2) + E_\beta(\tau, t_1, t_2) \\
 &= \sum_{ik,ln} A_{ik,ln}(\tau) e^{-2\pi i(v_{ik}^\alpha t_2 + v_{ln}^\beta t_1)} + \sum_{ik,ln} B_{ik,ln}(\tau) e^{-2\pi i(v_{ik}^\alpha t_1 + v_{ln}^\beta t_2)}
 \end{aligned} \quad (4.22)$$

where the coefficients  $A_{ik,ln}(\tau)$  and  $B_{ik,ln}(\tau)$  represent the modulation depth and the dependence on  $\tau$

$$A_{ik,ln} = \sum_{jm} (M_{il} M_{lj}^\dagger M_{jn} M_{nk}^\dagger M_{km} M_{mi}^\dagger) \left[ e^{-2\pi i(v_{ij}^\alpha + v_{lm}^\beta)\tau} + e^{2\pi i(v_{kj}^\alpha + v_{nm}^\beta)\tau} \right], \quad (4.23)$$

$$B_{ik,ln} = \sum_{jm} (M_{il} M_{lj}^\dagger M_{jn} M_{nk}^\dagger M_{km} M_{mi}^\dagger)^* \left[ e^{-2\pi i(v_{ij}^\alpha + v_{lm}^\beta)\tau} + e^{2\pi i(v_{kj}^\alpha + v_{nm}^\beta)\tau} \right]. \quad (4.24)$$

The  $M_{ij}$  terms represent the transition moments between nuclear spin level  $i$  of the  $\alpha$  electron spin manifold and nuclear spin level  $j$  of the  $\beta$  manifold. In the case of  $N$  magnetic nuclei coupled to the electron spin, calculation of the modulation of the ESE can be performed separately for each nucleus and then combined together according to

the product rule <sup>1</sup>:

$$E(\tau, t_1, t_2) = \frac{1}{2} \prod_c^N E_\alpha^c(\tau, t_1, t_2) + \frac{1}{2} \prod_c^N E_\beta^c(\tau, t_1, t_2) \quad (4.25)$$

Thus, the amplitude of a peak of a given nucleus depends not only on its modulation depth parameter and the  $\tau$ -dependent blind-spot term (both included in  $A_{ik,ln}^c$  and  $B_{ik,ln}^c$ ), but also on the corresponding terms from of all other nuclei [88]. Peaks of nuclei with shallow modulations can be strongly suppressed by other nuclei with deep modulations.

### 4.3 Density matrix formalism

The theory of density matrix formalism, first described for pulse NMR experiments, is a convenient approach for the description of quantum mechanical system dynamics [89, 90]. The state of a system at any time can be expressed in terms of a density matrix [69, 90] which, in general, has the form:

$$\rho = \begin{pmatrix} \overline{|c_1|^2} & \overline{c_1 c_2^*} & \dots & \overline{c_1 c_n^*} \\ \overline{c_2 c_1^*} & \overline{|c_2|^2} & & \\ \vdots & & \ddots & \\ \overline{c_n c_1^*} & & & \overline{|c_n|^2} \end{pmatrix} \quad (4.26)$$

where the diagonal elements ( $\overline{|c_i|^2}$ ) represents the probability to find the system in certain eigenstates and the non-diagonal elements  $\overline{c_i c_j^*}$  represents a "coherent superposition" (coherence) of the eigenstates. The time dependence of a system in terms of the density matrix is represented by the Liouville-von Neumann equation:

$$\frac{d\rho(t)}{dt} = -i[\mathcal{H}(t), \rho(t)] \quad (4.27)$$

When  $\mathcal{H}$  is time-independent, the formal integration of equation (4.27) leads to

$$\rho(t) = U(t)\rho(0)U(t)^\dagger \quad (4.28)$$

Where  $U(t)$  is an exponential operator (propagator), which propagate the density operator in time:

$$U(t) = \exp(-i\mathcal{H} t) \quad (4.29)$$

<sup>1</sup>For a simulation of powder spectra, this rule has to be applied inside the loop over orientations along the external magnetic field

### 4.3 Density matrix formalism

---

In the case of a time-dependent Hamiltonian, there is no straightforward integration possible. However, in many cases the experiment can be split into a sequence of time intervals, governed by different Hamiltonians, which remain constant within each interval. The evolution of the system at all time intervals is described by (4.28). Thus the overall evolution during the experiment can be calculated by:

$$\rho(t_{exp}) = U_n \dots U_2 U_1 \rho(0) U_1^\dagger U_2^\dagger \dots U_n^\dagger \quad (4.30)$$

For normalized state functions, the expectation value  $\langle A \rangle$  of an arbitrary observable operator  $A$  at time  $t$  is given by:

$$\langle A \rangle = \sum_r \sum_s \rho_{rs}(t) A_{rs} = tr \{ \rho(t) A \} \quad (4.31)$$

Thus the expectation value of any observable operator can be calculated by evaluating the trace of the product of the observable operator and the density operator. Combining (4.31) and (4.30) one can write

$$\langle A \rangle = tr \{ U_n \dots U_2 U_1 \rho(0) U_1^\dagger U_2^\dagger \dots U_n^\dagger A \} \quad (4.32)$$

This approach is called the *density operator formalism*. Typically, the propagators  $U_i$  corresponds either to perturbation (i.e. MW and RF pulses) or free evolution periods. If relaxation is present in the system, it is more convenient to describe the evolution of the system in terms of superoperators instead of propagators, as it was described above. A superoperator in Liouville space is a prescription for transforming one Hilbert space operator into another one:  $\rho' = \hat{R}\rho$ , where  $\hat{R}$  is the unitary transformation superoperator. The matrix elements of  $\rho$  are transformed as  $\rho'_{kl} = \sum_m \sum_n R_{klmn} \rho_{mn}$ . In terms of superoperators, it is possible to write the general equation of motion including both coherent and incoherent dynamics.

$$\frac{d}{dt} \rho(t) = -i \hat{\mathcal{H}} \rho(t) - \hat{\Gamma} \{ \rho(t) - \rho_{eq} \} \quad (4.33)$$

where  $\rho_{eq}$  is the density operator at thermal equilibrium. The matrix elements of the commutator superoperator  $\hat{\mathcal{H}}$  defined by  $\hat{\mathcal{H}}\rho = [\mathcal{H}, \rho]$ , can be calculated as

$$\hat{\mathcal{H}}_{klmn} = [\mathcal{H}_{kl} \delta_{mn} - \mathcal{H}_{mn} \delta_{kl}] \quad (4.34)$$

with  $\delta_{ij}$  is the Kronecker symbol ( $\delta_{ij} = 1$  for  $i=j$  and  $\delta_{ij}=0$  if  $i \neq j$ ).  $\hat{\Gamma}$  is the relaxation superoperator, whose matrix elements are dependent on the particular relaxation mechanisms, present in the system. If both Hamiltonian and the relaxation superoperator are

time-independent, the master equation (4.33) can be formally integrated. In this case the time dependence of the density matrix can be written as:

$$\rho(t) = \rho_{eq} + \exp\left[\left(-i\hat{\mathcal{H}} - \hat{\Gamma}\right)t\right](\rho(0) - \rho_{eq}) \quad (4.35)$$

The Liouvillian  $-i\hat{\mathcal{H}} - \hat{\Gamma}$  can always be written as a complex symmetric matrix, which is in general not Hermitian. If no relaxation is taken into account, solution of the (4.33) with the time-independent Hamiltonian yields a simple exponential expression, similar to eq.(4.29)

$$\rho(t) = \exp\left(-i\hat{\mathcal{H}}t\right)\rho(0) \quad (4.36)$$

In the eigenbasis of the Hamiltonian  $\mathcal{H}$ , the matrix representation of the master equation (4.33) can be written as:

$$\frac{d\rho_{\alpha\alpha'}(t)}{dt} = \frac{i}{\hbar} [\rho(t), \mathcal{H}_0] + \sum_{\beta\beta'} R_{\alpha\alpha'\beta\beta'} (\rho_{\beta\beta'}(t) - \rho_{\beta\beta'}^0) \quad (4.37)$$

where terms  $R_{\alpha\alpha'\beta\beta'}$  are elements of the *Redfield* relaxation supermatrix. For the case of a system with one spin  $S=1/2$  the elements of the relaxation matrix, corresponding to the longitudinal and transverse relaxation are following [69, 72, 90]:

$$R_{\alpha\alpha\alpha\alpha} = -\frac{1}{2T_1} \quad (4.38)$$

$$R_{\alpha\alpha\beta\beta} = +\frac{1}{2T_1} \quad (4.39)$$

$$R_{\alpha\beta\alpha\beta} = -\frac{1}{2T_2} \quad (4.40)$$

where  $\alpha \neq \beta$  and  $\alpha, \beta = [1, 2]$ ;  $T_1$  and  $T_2$  are the longitudinal and transverse relaxation times.

Therefore the relaxation matrix for the system  $S=1/2$  can be written in the following form

$$R = \begin{pmatrix} -1/2T_1 & & & 1/2T_1 \\ & -1/2T_2 & & \\ & & -1/2T_2 & \\ 1/2T_1 & & & -1/2T_1 \end{pmatrix} \begin{matrix} |1, 1\rangle \\ |1, 2\rangle \\ |2, 1\rangle \\ |2, 2\rangle \end{matrix} \quad (4.41)$$

Here only longitudinal and transverse relaxation are taken into account.

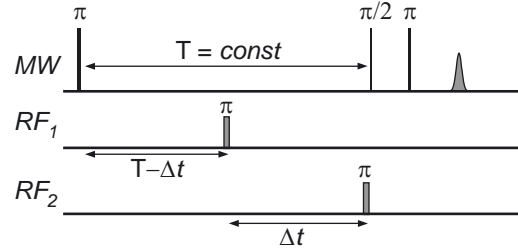
#### 4.4 Relaxation effects in TRIPLE experiment

This part of the "EPR spectroscopy" chapter concerns effects of the relaxation processes on TRIPLE spectra, which were experimentally observed during study of the  $H_{ox}$ -CO state of the H-cluster. As it will be shown in chapter 6,  $^{57}Fe$  difference TRIPLE spectra can reveal peaks, corresponding to the electron spin manifold, which NMR transitions were not excited by the first RF pulse. In this section the application of the density matrix approach to TRIPLE experiments is described.

During an earlier study of malonic acid, described by Höfer in his PhD thesis [84] pulse TRIPLE spectra also revealed peaks corresponding to the NMR transitions of both  $m_S$  manifolds. In that work a simplified quantitative description of this phenomena was presented.

In order to obtain an analytical expression Höfer considered the presence of only one  $I = 1/2$  nuclear spin coupled to the electronic spin  $S = 1/2$  (i.e. a four-level system).

The following pulse sequence was used for these calculations:



Here all pulses were considered to be infinitely short and first RF pulse to excite the NMR transition in the  $m_S = +1/2$  manifold.

The intensities of the lines in the difference TRIPLE spectrum were calculated for NMR transitions of the both electron spin manifolds ( $m_S = \pm 1/2$ ). The following dependence on the delay between the two RF pulses  $\Delta t$  was found:

$$I_{\pm}(\Delta t) = -I_0 \{ \exp(-T/T_{1S}) \pm \exp(-\Delta t/T_{1I}) \exp(-[T - \Delta t]/T_{1S}) \} \quad (4.42)$$

where  $I_0$  is the intensity of the Hahn echo signal,  $T_{1S}$  and  $T_{1I}$  are the longitudinal electronic and nuclear spin relaxation times.

As follows from this formula, if the first RF pulse starts immediately after the inversion pulse (then,  $\Delta t = T$ ), and  $T_{1S} \ll T \ll T_{1I}$ , it simplifies to

$$I_{\pm} = \mp I_0 \exp(-T/T_{1I}) \quad (4.43)$$

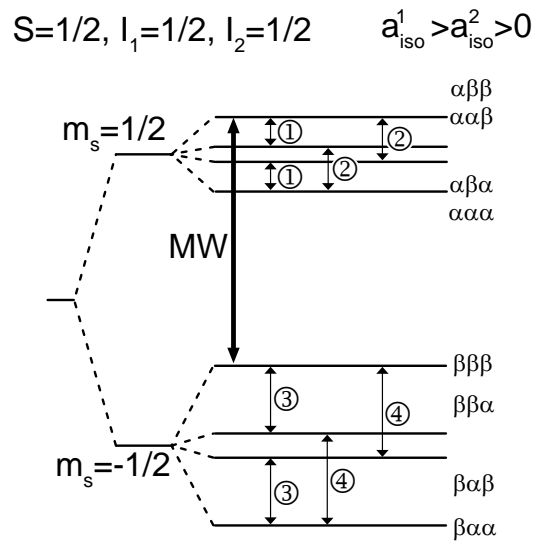


**Figure 4.10:** Energy scheme for the system of an electron spin  $S = 1/2$ , coupled to two nuclei  $I_1 = I_2 = 1/2$  with  $a_{iso}^1 > a_{iso}^2 > 0$  and  $\nu_{I1} = \nu_{I2} < 0$ .

Hence, in this case these two peaks in the difference TRIPLE spectrum will have the same intensities but different sign. As a result, it was concluded, that if the electron spin relaxation  $T_{1S}$  is much faster than the nuclear one ( $T_{1I}$ ) and if  $T_{1S}$  is comparable to the delay between applied RF pulses  $\Delta t$ , the detected signal is mostly due to the created polarization of the NMR transitions, which decays with the longitudinal nuclear spin relaxation rate ( $1/T_{1I}$ ).

Using the density matrix formalism described above it is possible to obtain numerical solutions for the more general case, when the system consist of two nuclear spins  $I_1 = I_2 = 1/2$ , coupled to a  $S = 1/2$  electron spin (see figure 4.10). The results of the calculations are shown in figure 4.11.

As follows from equation (4.43), the longitudinal nuclear spin relaxation reduces the created polarization of the NMR transition, which will only results in a general reduction of the ENDOR/TRIPLE efficiency. Therefore, in current calculations only the longitudinal electronic spin relaxation is taken into account (so that  $T_{1I_1} = T_{1I_2} \rightarrow \infty$ ). In all calculations presented here the electron spin relaxation rate was set to  $T_{1S} = 200\mu s$  while the time between MW inversion pulse and MW detecting sequence was set to  $T=300\mu s$ . The frequency of the first RF pulse was set to NMR transition of the first nuclear spin in the  $m_S = +1/2$  manifold (①) (see figure 4.10). Therefore, the amplitude

#### 4.4 Relaxation effects in TRIPLE experiment

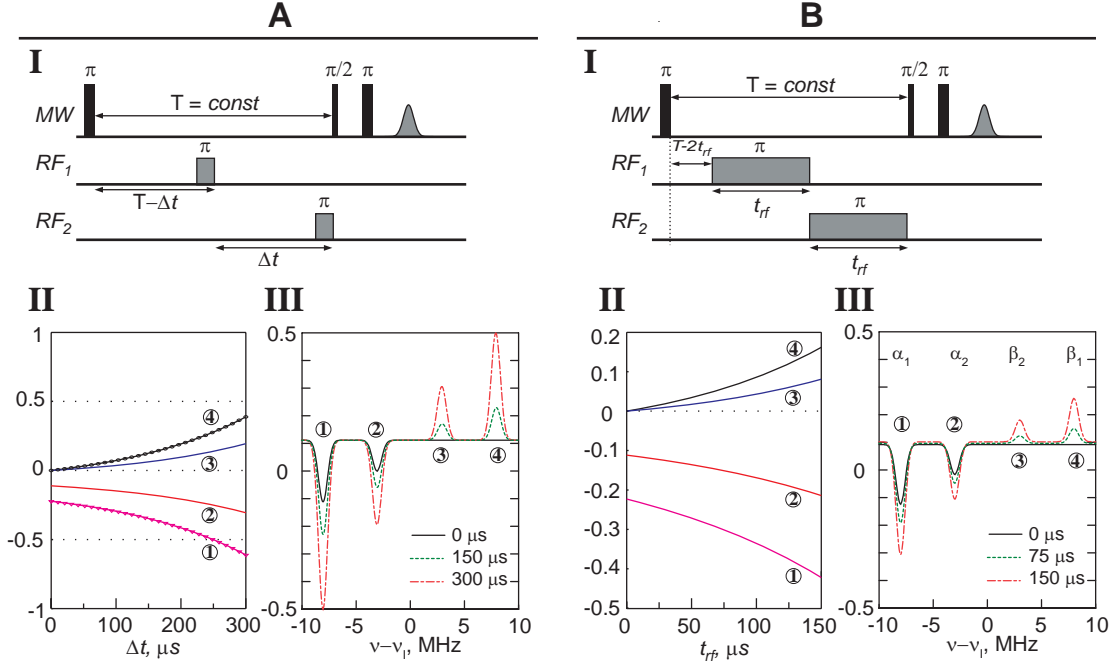


**Figure 4.11:** Calculation of the effect of longitudinal relaxation ( $T_{1S}$ ) on difference TRIPLE spectra. Case **A**: all pulses are momentary; delay between inversion and detection is constant ( $T = 300\mu\text{s}$ ); second RF pulse is directly before MW  $\pi/2$  pulse, first RF pulse shuttle between MW inversion pulse and second RF pulse. Only the relaxation processes during the evolution periods are taken into account. Case **B** RF pulses are rectangular (ideal) with finite length; MW pulses are momentary; between RF pulses there is no delay; length of both RF pulses ( $t_{rf} = t_{rf1} = t_{rf2}$ ) varied from 0 to  $T/2$ . In both sequences first RF pulse excites transition ①. Amplitudes of the lines in difference TRIPLE spectra as a function of  $\Delta t$  (**A**) and  $t_{rf}$  (**B**) shown on plots **II**. Plot **A.II** includes calculations according to analytical formula (scatter plot). Some selected traces of difference TRIPLE spectra are shown on the plot **III**. Marking of peaks is consistent with notations on figure 4.7. Considered system:  $S = 1/2$ ,  $I_1 = I_2 = 1/2$ ,  $a_{iso}^1 > a_{iso}^2 > 0$ ,  $\omega_I < 0$ . So that transitions ① and ② are of  $m_s = 1/2$  manifold, and ③, ④ belong to  $m_s = -1/2$  manifold.

of the peak corresponding to ④ NMR transition in the difference TRIPLE spectrum should have the same  $\Delta t$ -dependence as described by equation (4.42).

Figure 4.11,**A.II** presents a comparison of calculations, made using the relaxation matrix approach with those according to eq. (4.42). As expected, the dependence of the intensity of the peaks, corresponding to  $I_1$  (①, ④) exactly fits to the analytical expression (4.42). It was found, that the lines corresponding to the NMR transitions of the second nucleus (transitions ② and ③) behave in the same manner, though the amplitudes are twice smaller than for the peaks of ① and ④. This shows, that if several nuclear spins are

coupled to the electronic spin, they all can give rise to positive and negative peaks in the difference TRIPLE spectra, originating from both  $m_S$  manifolds.

In the experiments, presented in chapter 6 there was no delay between the two RF pulses<sup>2</sup>. Thus, in this case the observed positive peaks in the difference TRIPLE spectra can not be explained by this theory.

Another origin of the similar effect can be the longitudinal electron spin relaxation *during* the RF pulses. In the Q-band ENDOR and TRIPLE experiments, the length of the RF pulses was about 50  $\mu\text{s}$ . Therefore, it is necessary to consider an RF pulse with finite length (figure 4.11B). Calculations were performed using a similar pulse sequence as in the previous calculations (figure 4.11A). Also in this sequence, the delay between inversion and detection remains constant ( $T = 300\mu\text{s}$ ). The length of the RF pulses ( $t_{rf}$ ) however was varied from 0 to  $T/2$ . In order to simplify the analysis, the delay between the RF pulses was neglected ( $\Delta t = 0$ ). The results shown in figure 4.11B reveal similar spectra as in the first calculations. Increasing length of the RF pulses leads to appearing the positive peaks in the difference TRIPLE spectra, which corresponds to the NMR transitions of the  $m_S = -1/2$  manifold, while pumping RF pulse was exciting transition ① of the  $m_S = +1/2$  manifold.

It is concluded, that in a difference TRIPLE spectrum it is possible to observe peaks corresponding to NMR transitions of the other  $m_S$  manifold as pumped transition, but with opposite sign in addition to the peaks, corresponding to the direct TRIPLE resonance. The effect is owing to the relaxation of the electron spin polarization of the detected EPR transition to the equilibrium state during the mixing period when RF pulses are applied. The magnitude of this effect is strongly dependent on the longitudinal electron spin relaxation rate ( $1/T_{1S}$ ) with respect to the duration of the pulse sequence.

---

<sup>2</sup>In some experiments, not shown in this thesis,  $\Delta t$  was set to 4  $\mu\text{s}$ , however no principle difference with spectra shown on figure 6.6 has been found.

#### 4.4 Relaxation effects in TRIPLE experiment

---

---

# 5

## Materials and methods

---

### 5.1 Purification and activation of the enzyme

The enzyme was isolated from *D. desulfuricans* cells as described [44]. The amount of protein was determined via quantitative amino-acid analysis. The enzyme concentration derived in this way was in excellent agreement with the concentrations determined from the Fe-S UV/Vis signals in the H<sub>2</sub>-reduced enzyme. For growing the <sup>57</sup>Fe-enriched enzyme, the bulk salts for the growth medium were depleted of Fe by passage over Chelex-100 and the medium was supplemented with <sup>57</sup>Fe. Metallic Fe (95.6% enriched in <sup>57</sup>Fe) was purchased from Chemotrade (Germany), and 200 mg was dissolved in a minimum of concentrated sulphuric acid. The pH of this solution was adjusted to 6.6 with 10 M NaOH. The solution was filter-sterilized and subsequently added to 120 L of sterile lactatesulphate media distributed in 20 L flasks.

After purifications the enzyme was activated by repeatedly evacuating and flashing H<sub>2</sub> gas for 10 min. After this treatment the enzyme is in the fully reduced form (H<sub>red</sub>). The oxidized form (H<sub>ox</sub>) was obtained by replacing H<sub>2</sub> by Ar. The H<sub>ox</sub>-CO state have been prepared by incubation of the active enzyme under CO atmosphere for 10-15 min. All manipulations were performed on ice and in a dark. The sample was slowly stirred by small magnetic bar to improve gas exchange.

The active enzyme is both light and oxygen sensitive. Therefore, all manipulations with samples were performed under strict anaerobic conditions. For this purpose an anaerobic 'glove-box' with an atmosphere of N<sub>2</sub> with addition of 1-5% H<sub>2</sub> has been used in most of the cases. The exception is an activation with H<sub>2</sub>, Ar or CO gas, which was performed outside the 'glove-box'. To keep anaerobic conditions an 'eppendorf' plastic tube with the sample was placed inside a glass vial. The glass vial was sealed by a rubber cup with a metal stopper. To keep sample in the dark, glass vial was covered by black paper. All these manipulations are performed in 'glove-box' and then it was taken out and connected to the anaerobic line. A needle was passed through the rubber cap to connect the glass vial to the anaerobic line.

If [FeFe]-hydrogenase in the active form, it is also sensitive to day-light as it was recently discussed by Albracht et al. [38, 47]. Therefore all manipulations were performed in dark with dim red light. For this purpose the 'glove-box' has been covered by opaque material and equipped with red lamp.

### 5.2 Preparation of samples for EPR measurements

For EPR study, presented in this thesis, a standard quartz tubes has been used. Measurements at Q-band were performed using tubes of 2.8 mm outer diameter and 2 mm inner diameter. Volume of the sample inside the tube was varied from 20  $\mu\text{l}$  to 35  $\mu\text{l}$  with concentration of 0.3 - 1 mM. Some X-band EPR measurements were also performed using these samples.

Most of the X-band EPR measurements were performed using tubes either 5 mm outer and 4mm inner diameter filled with 200-300  $\mu\text{l}$  of sample or using tubes of 4 mm outer and 3 mm inner diameter filled with 50-200  $\mu\text{l}$  of sample. Photo-dissociation experiments were performed on moderately transparent samples with concentration of 50  $\mu\text{M}$ . All other experiments were performed on sample with concentration of 0.2 mM - 1 mM.

Samples of [FeFe]-hydrogenase were transferred to a quartz tube inside the 'glove-box' and immediately frozen to the temperature of liquid nitrogen (77K) (also inside the 'glove-box').

When necessary, frozen protein samples were repeatedly purged with  $\text{H}_2$  gas prior to any additional treatment in order to minimize oxidative damage to the protein. For this purpose EPR sample tube was connected to the anaerobic line via rubber tube. After 10-15 repetitions of purging the sample tube was sealed and transferred to the 'glove-box' for subsequent thawing and further treatment.

### 5.3 X-band EPR experiments

All X-band measurements presented in this work have been performed on a Bruker ELEXSYS E-580 X-band spectrometer with a SuperX-FT microwave bridge and CF935 Oxford flow cryostat. The temperature in the cryostat was controlled by an Oxford ITC 5025 temperature controller. For ENDOR measurements an overcoupled Bruker ER 4118X-MD5-EN dielectric ENDOR resonator was used. For HYSCORE and CW EPR measurements an ER 4118X-MD5 dielectric resonator has been used. Measurements of pulse EPR spectra have been performed using both resonators. If not specified, an ER

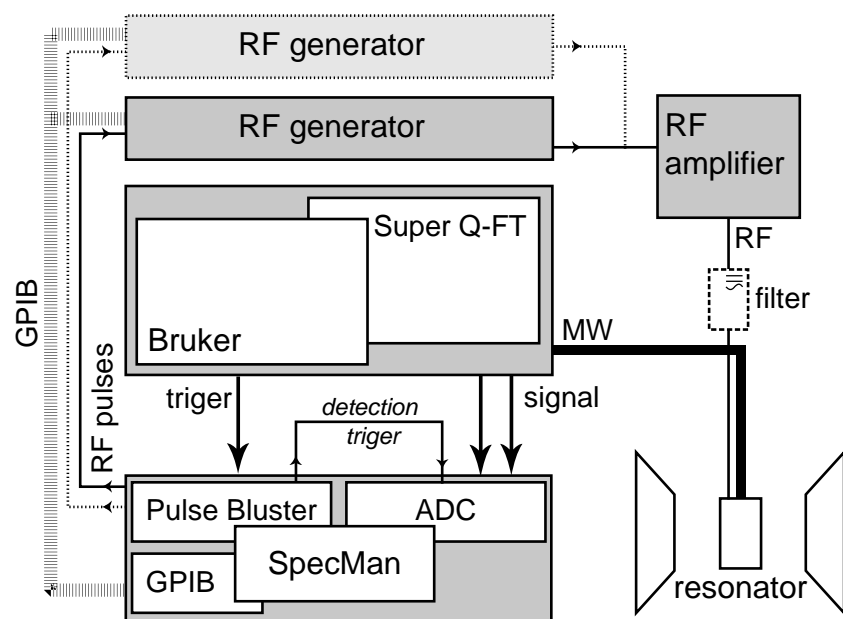


**Figure 5.1:** Scheme of the Q-band setup for ENDOR measurements with random-acquisition using the SpecMan software

4118X-MD5 resonator (no RF coils) has been used. In all pulse experiments the MW pulses were amplified using a Traveling Wave Tube (TWT) amplifier (1 kW). In order to suppress the harmonics of the  $^1\text{H}$  ENDOR signals, a low pass Trilithic<sup>TM</sup> filter H5LEC10-3-AA with a cut-off frequency of 10 MHz was used. The X-band ENDOR spectra were recorded using the standard Bruker data acquisition software. RF pulses were generated by standard Bruker RF generator and amplified by ENI A-500 RF amplifier with amplification factor of 60 dB.

#### 5.4 Q-band EPR experiments and 'SpecMan' set-up

All pulse Q-band measurements were performed on a Bruker ELEXSYS E 580 Q-band spectrometer with the SuperQ-FT microwave bridge. For these measurements a home-built slightly overcoupled cylindrical  $\text{TE}_{011}$  resonator has been used. This resonator has a construction similar to the one described by Sienkiewicz et al. [91]. The solid-state microwave amplifier in the bridge produces a power of 0.5 W at the resonator. This is sufficient for obtaining a MW  $\pi/2$  pulse of 32 ns. Cryogenic temperatures were reached using an Oxford CF935 flow cryostat.

The long RF pulses needed for Q-band  $^{57}\text{Fe}$  ENDOR and TRIPLE experiments,

## 5.5 Photo-dissociation experiments

---

(> 45  $\mu$ s) cause heating in the resonator, whereby its properties are changed, especially in case of high repetition rates. These effects lead to changes in intensity of the ESE signal that are not correlated with the ENDOR effect. Such changes can cause artifacts and baseline distortions in the ENDOR spectra. In principle, it is possible to decrease the "heating" effect by using a slower repetition rate, but this would increase the measurement time considerably.

Another possibility is the usage of a random-acquisition procedure in which the RF frequency is stochastically varied in the frequency range of the experiment [92]. In this case the heating effects will be randomized and only add to the experimental noise. Since stochastic changes of RF frequency are not implemented in the Bruker ELEXSYS system a home-built system has been used, based on SpecMan software on a PC computer [93]. The Bruker spectrometer was used for generating MW pulses and triggering the 'SpecMan' system, which in turn controlled the generation of RF pulses and recorded the signal coming from the Bruker spectrometer. For an analog-to-digital converter (ADC) device an Acqiris DP240 (DP235) PCI Digitizer Card (8 bit) has been used. For the generation of RF pulses a programmable TTL pulse generator Pulse Bluster<sup>TM</sup> (SpinCore Technology Inc.) has been used. The RF generator was controlled via the GPIB interface.

If SpecMan setup has been used the RF pulses were generated by an Agilent E4420B radio-frequency generator and amplified either by an ENI 3200L RF solid-state amplifier, with a 55dB amplification factor or by an ENI A-500 RF amplifier with a 60 dB amplification factor. In order to suppress the 'harmonics' of the <sup>1</sup>H ENDOR signals, a Trilithic<sup>TM</sup> high power low-pass filter H4LE35-3-AA ('cut off'-frequency 35MHz) was used.

The TRIPLE resonance experiments were also performed using the SpecMan system. In this case a Rohde&Schwarz<sup>TM</sup> SMT02 continuous-wave RF generator with a Mini-Circuit<sup>TM</sup> ZASWA-2-50DR switch was added to generate the fixed frequency pumping RF pulse.

## 5.5 Photo-dissociation experiments

Most of the photo-dissociation experiments were done using X-band Bruker ESP380 setup with an 4118X-MD5 resonator, at a temperature of 40 K. The modulation frequency was set to 100 kHz, modulation amplitude to 5 G, MW power was of 40 dB attenuation. Each scan was performed with a time constant of 40.96 ms and conversion time of 40.96

ms using 1024 points. Some additional X-band measurements were performed using a Bruker ELEXSYS E-580 X-band spectrometer with a SuperX-FT microwave bridge using the same settings as for the other experiments.

Illumination of the sample was carried out inside the Oxford cryostat within the X-band EPR set-up, by an optical parametric oscillator (OPO) GWU model VISIR 120 which was pumped by the second harmonic of a Nd:YAG laser Spectra Physics model GCR-130. Some experiments were done with the fundamental wavelength of 355 nm of the pump laser. The pulse repetition rate of the laser is about 10 Hz. Incident light intensity in front of the cryostat window was measured by a PEM 25 power-meter. The Nd:YAG laser can generate stable pulses only with more than 80% of maximum power of pumping lamp. So, the tuning OPO pumping beam power was used only for a fine adjustment of power of outcome laser beam. Mostly, the intensity of the outcome laser beam was adjusted by using Schott glass filters NG11. The KG series of the Schott glass filters were used for cutting an infrared components of the laser beam.

At the beginning of the illumination, when the photo-induced processes are fast, spectra were obtained from one scan of the magnetic field. To improve the observation of small changes at the second phase of the photo-dissociation experiment several scans were accumulated. The Q-band set-up consists of a Bruker ELEXSYS E 580 Q-band spectrometer with the SuperQ-FT microwave bridge in pulse mode. According to the studied wavelength dependence of the photo-dissociation rates, the fastest conversion was achieved at a wavelength of 355 nm. However, the wavelength of 531 nm has been chosen due to technical difficulties to obtain excitation light below 500 nm with sufficient power using the Q-band experimental set-up. If not specified, the temperature was set to 50 K. Photo-dissociation processes were controlled by observation of the FID signal after a MW pulse of 400-1000 ns with reduced power ( $>16$  dB attenuation). If not specified, the length of the MW pulse was 400 ns. For the illumination of the sample in the Q-band experimental set-up, light excitation at 532 nm was achieved with the laser system from Quantel (Brilliant Series). It consists of an OPO, type Vibrant 355 II, pumped by short ( $\approx 8$  ns) light pulses at 355 nm provided by a Nd:YAG Laser.

## **5.6 Simulation of EPR, ENDOR and HYSCORE spectra**

Simulations of the EPR (both CW and pulse) and pulse ENDOR spectra were carried out by home-written routines based on 'pepper' and 'salt' functions of the EasySpin

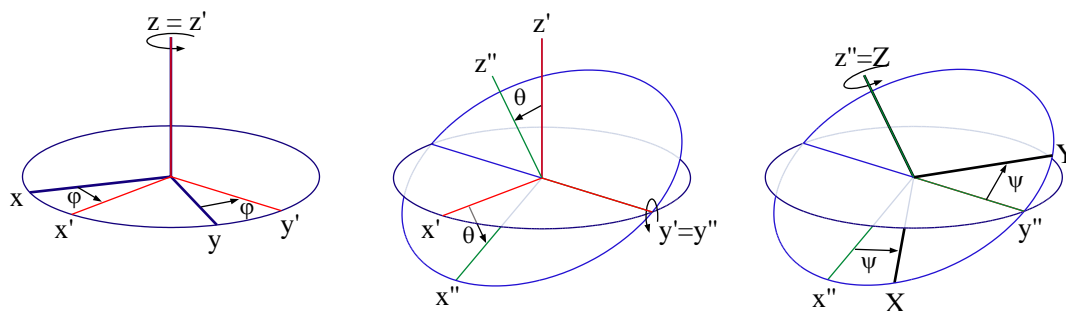


**Figure 5.2:** Rotation of the axes system  $[x, y, z]$  given by Euler angles  $(\varphi, \theta, \psi)$ .

package for the MatLab<sup>TM</sup> programming environment.

For all simulations of EPR (CW and pulse), ENDOR and HYSCORE spectra the following spin Hamiltonian has been used (see chapter 4):

$$\mathcal{H} = \mathcal{H}_{ze} + \mathcal{H}_{zn} + \mathcal{H}_{hf} + \mathcal{H}_q \quad (5.1)$$

Simulation of all HYSCORE spectra was performed by home-written routines for MatLab<sup>TM</sup> assuming ideal rectangular MW pulses according to theoretical formulas 4.22 and 4.24. Since direct calculation of the 2D modulation pattern is very time-consuming, the calculations were carried out in the frequency domain in analogy to those discussed previously [87]. The calculated frequencies and amplitudes of the crosspeaks were assembled to an 2D spectrum in the frequency domain. For the case of several nuclear spins interacting with the electron spin, the product rule according to equation 4.25 has been used. In this case the frequencies and the amplitudes of all 'combination' peaks were calculated within the loop over the possible orientations and added to the frequency domain spectrum. Then, this spectrum is transferred to the time domain using the inverse discrete Fourier transformation. After eliminating the negative time parts and simulating the lineshapes (based on gaussian lineshape), the time-domain data were transformed back to the frequency domain.

Orientations selected by MW pulses were calculated taking into account only the electron Zeeman interaction assuming that the HF splitting is much smaller in comparison with  $g$ -anisotropy. This is a good approximation for the investigated system for both the X- and Q-band frequency ranges. In all simulations, the Euler angles are given according to the 'y'-convention. The so-called "y-convention," illustrated in figure 5.2. In this

convention, the rotation given by Euler angles  $(\varphi, \theta, \psi)$ , where the first rotation is by an angle  $\varphi$  about the z-axis, the second is by an angle  $\theta$  about the  $y'$ -axis, and the third is by an angle  $\psi$  about the  $z''$ -axis (again). There are several possible rotations, all of which give the same result:  $R(\varphi, \theta, \psi) = R(\varphi + \pi, -\theta, \psi + \pi) = R(\varphi - \pi, -\theta, \psi - \pi)$

## 5.7 UV/Vis experiments

All the investigated states were generated on the same sample in order to allow a direct comparison of spectra. Absorbance spectroscopy measurements were done on a UNICAM UV2 UV/Vis spectrometer against distilled water at room temperature. For the UV/Vis measurements, described in chapter 9, the UV/Vis cells Hellma 114-QS, 1400 $\mu$ l with 10 mm path length were used. In order to prevent an oxidative damage these UV/Vis cells were sealed by a plastic cap with additional 'teflon' tape on it. All manipulations with sample were performed via the anaerobic 'glove-box'.



---

# 6

## The H<sub>ox</sub>-CO state of the H-cluster

---

This chapter presents the investigation of the CO-inhibited oxidized state (H<sub>ox</sub>-CO) of the active site of the [FeFe] hydrogenase from *D. desulfuricans*. Figure 6.1 shows the schematic representation of the H-cluster in the H<sub>ox</sub>-CO state, as it was proposed from earlier X-ray and IR studies [26, 36] of [FeFe]-hydrogenase from both *C. pasteurianum* and *D. desulfuricans*. In the work, presented here the electronic structure of the H-cluster in the H<sub>ox</sub>-CO state has been investigated using pulse EPR spectroscopy on the <sup>13</sup>C- (CO) and <sup>57</sup>Fe-labeled H-cluster. Investigation of the <sup>57</sup>Fe HF couplings provide information about the overall electronic structure of the H-cluster. A more specific information about the electronic structure of the bi-nuclear can be obtained from investigation of the HF couplings of the <sup>13</sup>C nuclei of the CO ligands. The CO ligands of the H-cluster are thought to play an important role in the catalytic process of hydrogen evolution. Study of the nuclear spin interactions of the <sup>14</sup>N may provide additional details about the spin-density distribution over CN ligands of the bi-nuclear subcluster.

### 6.1 EPR spectra of non-labeled samples

According to the latest CW EPR investigation of the H<sub>ox</sub>-CO state of the H-cluster from *D. desulfuricans*, the X-band CW EPR spectrum of this state has slight rhombicity of the signal [38]. In order to verify this observation, pulse Q-band EPR spectra were recorded by detection of the free-induction decay (FID) after "hard" MW pulse. Figure 6.2 presents a comparison of EPR spectrum, obtained at X-band (CW) with Q-band (FID-detected). While the X-band spectrum shows only a small asymmetry of the high-field component of the spectrum, two high-field components of the spectrum are clearly resolved in the Q-band spectrum. These measurements confirm the rhombic contribution to the g-tensor of the H<sub>ox</sub>-CO state. Both simulations, presented in figure 6.2, were obtained using the following g-values:

$$g_1 = 2.065, g_2 = 2.007, g_3 = 2.001.$$

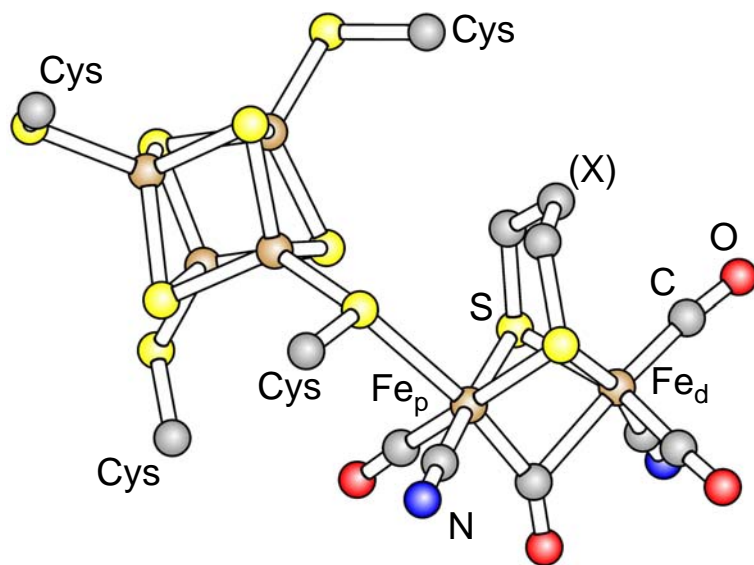


**Figure 6.1:** Schematic 3D representation of the H-cluster in the  $\text{H}_{\text{ox}}\text{-CO}$  state. Coordinates of the H-cluster were obtained from structure of the [FeFe]-hydrogenase from *D.desulfuricans* [26] (Protein Data Bank entry **1c4a**).

To date, there is no information available about the positioning of the  $g$ -tensor in the structure of the H-cluster, nor have any assignments of these values to the principal axes of the  $g$ -tensor have been made. In this study, the determined principal values will be numerated with decreasing  $g$ -values as presented above.

## 6.2 Investigation of the $^{57}\text{Fe}$ HF couplings

### 6.2.1 Broadening effect in the EPR spectrum

In this section we discuss the results of the investigation of the  $^{57}\text{Fe}$  hyperfine (HF) couplings by various pulse EPR methods. In contrast to the non-enriched samples, pulse EPR measurements of the  $^{57}\text{Fe}$  enriched samples reveal quite large modulations of the electron spin echo signal. Conventional ESE detected methods of recording EPR spectra results in large distortions of the signal. Therefore the FID-detected EPR method has been used in order to obtain Q-band spectra. The comparison presented in figure 6.3 shows that the presence of the  $^{57}\text{Fe}$  isotopes significantly broaden the EPR spectrum of the  $\text{H}_{\text{ox}}\text{-CO}$  state which indicates strong  $^{57}\text{Fe}$  HF interactions. Previously reported Mössbauer and ENDOR investigations of the  $^{57}\text{Fe}$  -enriched H-cluster in the  $\text{H}_{\text{ox}}\text{-CO}$  state in [FeFe]

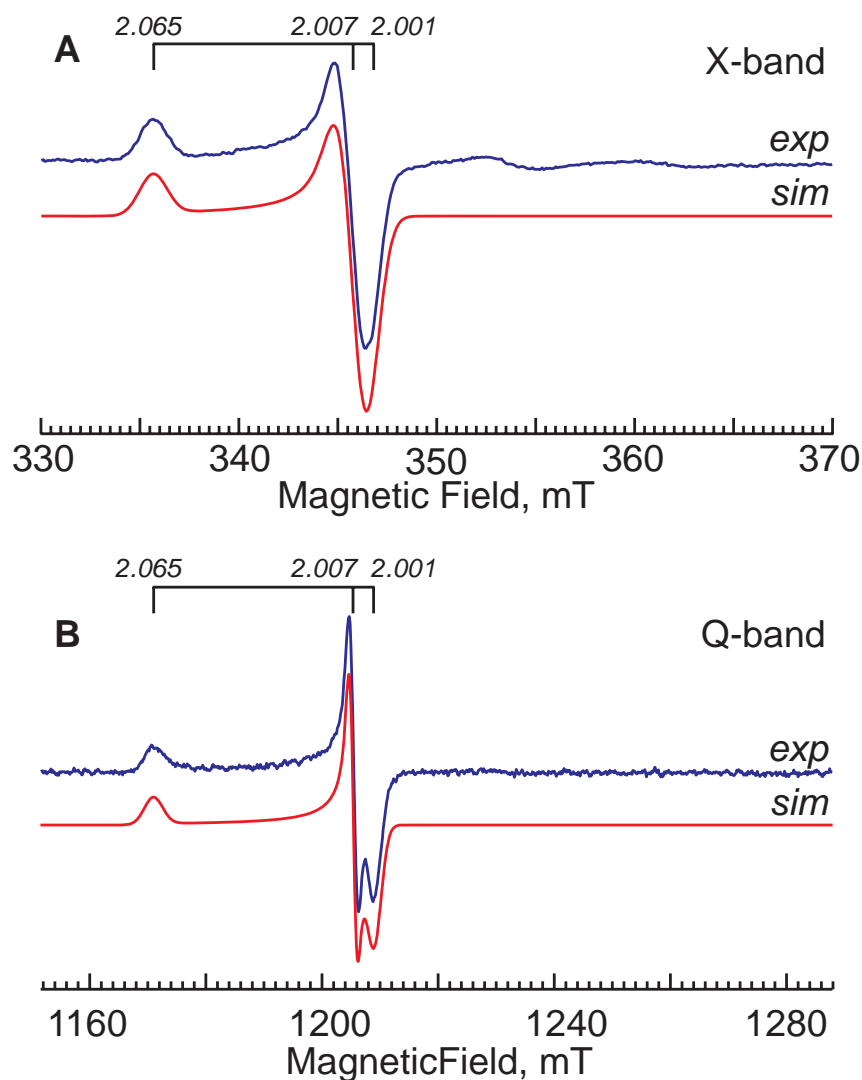


**Figure 6.2:** X- and Q-band EPR spectra of the H-cluster in the  $H_{ox}$ -CO state and the respective simulations. Experimental details: **A.** X-band CW EPR spectrum, temperature, 35K;  $0.2 \mu\text{W}$  (60dB); 9.7134GHz, Mod.Freq., 100 kHz; Mod.Amp., 0.5 mT; Time Const. 40.96 ms; Conversion time, 81.92 ms; **B.** Q-band pseudo-modulated FID-detected EPR spectrum, temperature, 15K;  $t_{mw}$ , 400 ns; MW power, 16dB att; Pseudo-modulations performed using a peak-to-peak modulation amplitude of 1.0 mT. Both experimental spectra plotted in the same  $g$ -scale. Signals at high magnetic field of the X-band EPR spectrum (marked by asterix) are due to reduced dipolar coupled F-clusters and contaminating signals of the material of the resonator.

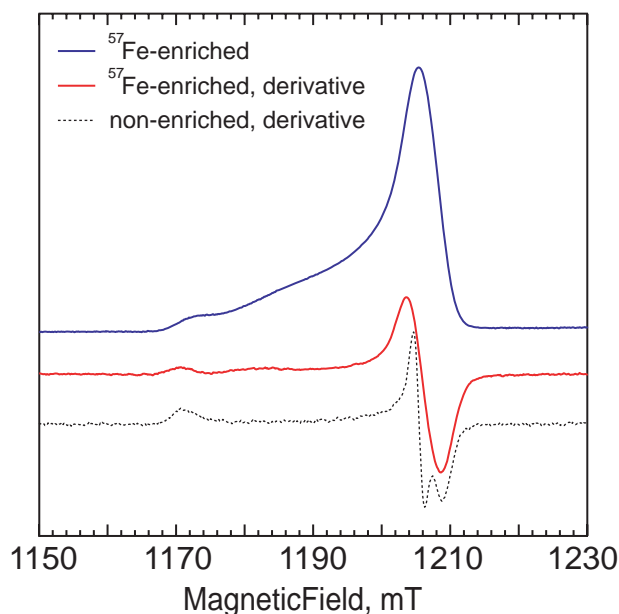


**Figure 6.3:** FID-detected EPR spectrum of the  $^{57}\text{Fe}$ -enriched H-cluster in the  $\text{H}_{\text{ox}}\text{-CO}$  state (solid lines) in comparison with spectrum of non-enriched enzyme (dashed line). Experimental conditions: temperature, 15 K; microwave frequency 33.86 GHz; microwave pulse length ( $t_{\text{mw}}$ ), 400 ns. The first derivative spectra were obtained using pseudo-modulations procedure with a peak-to-peak modulation amplitude of 1 mT.

hydrogenase of the *D.desulfuricans* and in the hydrogenase II (uptake) of *C. pasteurianum* (*C.p.II*) showed four HF interactions in the range of 30 MHz [48, 49, 52]. However, due to splitting of the EPR lines as a result of  $^{57}\text{Fe}$  HF interactions is not resolved, determination of HF coupling constants is very complicated and unreliable. In the following section, more advanced EPR techniques have been applied to extract parameters of the  $^{57}\text{Fe}$  HF interactions.

### 6.2.2 Pulse ENDOR study

One of the most powerful methods to obtain information about strong HF couplings is pulse ENDOR. In this study the Davies ENDOR sequence, introduced in chapter 4, was used. In this method the NMR transitions are detected via observation of the changes in polarization of the observed EPR transition. Figure 6.4 shows the Q-band  $^{57}\text{Fe}$  orientation-selective Davies ENDOR spectra for the  $\text{H}_{\text{ox}}\text{-CO}$  state measured at various field positions. Since the EPR spectrum is almost axial, for the static magnetic field corresponding to  $g = 2$ , the MW pulses select all orientations corresponding to both  $g_1$

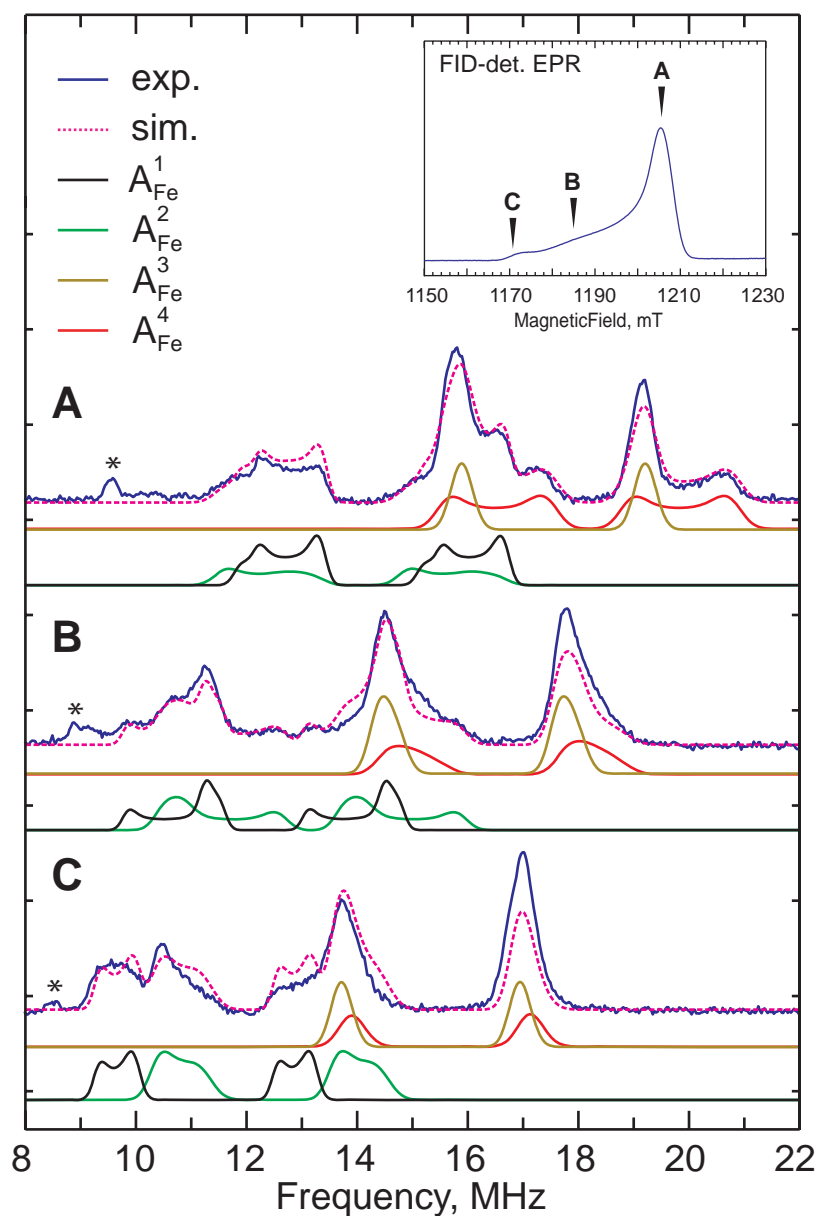


**Figure 6.4:** Q-band Davies ENDOR spectra of the  $^{57}\text{Fe}$ -enriched [FeFe]-hydrogenase in the H<sub>ox</sub>-CO state. The blue solid lines represent experimental data. The dashed magenta lines represent simulations of the ENDOR spectra. The colored solid lines below each experimental spectrum are the components of the simulation corresponding to different HF couplings (see Table 6.1). Experimental details: all spectra recorded at 15K with  $45\mu\text{s}$  RF pulse using random acquisition; **A.**  $B_0 = 1205.4\text{mT}$  ( $g_2$ ); **B.**  $B_0 = 1185.7\text{mT}$  (intermediate position); **C.**  $B_0 = 1173.0\text{mT}$  ( $g_1$ ). Asterisks (\*) marks artifacts due to the experimental setup (harmonics of the RF frequency). The EPR spectrum in the insert is identical to the spectrum presented in figure 6.3.

and  $g_2$ , thereby limiting orientation selectivity. Additional ENDOR spectra were recorded for an intermediate position as well as for  $g_1$  (figure 6.4). For these measurements a 45  $\mu\text{s}$  RF pulse of 300W was used. This length was selected from the recorded dependence of the ENDOR efficiency on the length of an RF pulse (Rabi-nutation). As described in chapter 4, in the case of a nuclear spin  $I = 1/2$ , a strong HFI ( $|A| > |2\nu_I|$ ) in the ENDOR signal appears as a doublet centered at  $|A/2|$ , and split by double the Larmor frequency  $\nu_{^{57}\text{Fe}}$  ( $\nu_{^{57}\text{Fe}}=1.652$  MHz at 1.2T). Several of these (partly overlapping) doublets can be recognized in the orientation selective ENDOR spectra. Since the lineshapes in the ENDOR spectra are quite complicated (even for the "single-crystal" type orientation  $g_1$ ), a straightforward analysis of the spectra is difficult. Therefore, a complete simulation of the ENDOR spectra was performed in order to extract the HF coupling constants (hfccs). A simulation assuming four strong HF couplings showed good agreement with the experimental data presented in figure 6.4. These parameters used for these simulations are summarized in Table 6.1 ( $A_{Fe}^1 - A_{Fe}^4$ ).

In order to confirm the obtained parameters, X-band Davies-ENDOR spectra were also recorded and simulated by the same set of HFI parameters. As can be verified in figure 6.5, the obtained simulation parameters also reproduce the X-band Davies ENDOR spectra very well. The X-band  $^{57}\text{Fe}$  ENDOR spectrum, however, has a much lower spectral resolution and suffers from overlap with the  $^1\text{H}$ -ENDOR signal. The figure also includes spectrum of the Q-band proton ENDOR, measured at  $g_2$ . In general, ENDOR spectroscopy is not providing information about the signs of the HF couplings. If nuclear spin relaxation processes are slower than the repetition rate of the pulse sequence, it is possible to observe "polarized" ENDOR spectrum as it was described by Epel et al. [94]. However, in these studies such effects were not observed.

In this work the Q-band pulse TRIPLE spectroscopy was used in order to determine the relative signs of the  $^{57}\text{Fe}$  HF couplings as shown in figure 6.6. To make a proper analysis, the TRIPLE spectra were subtracted from the ENDOR spectrum, recorded using the same experimental conditions. However, it turns out that difference TRIPLE spectra obtained using the sequential recording of TRIPLE and ENDOR spectra can also give rise to artifacts. In order to obtain a single TRIPLE spectrum with sufficient quality, it had to be accumulated for 2-3 hours. After this time the experimental conditions may have change slightly (e.g. phase drifting). Therefore the recording of an ENDOR spectrum prior to the TRIPLE experiment will not provide a valuable reference for the difference TRIPLE spectra. In this study a 2D TRIPLE method [95, 96] with a 5 point second dimension has

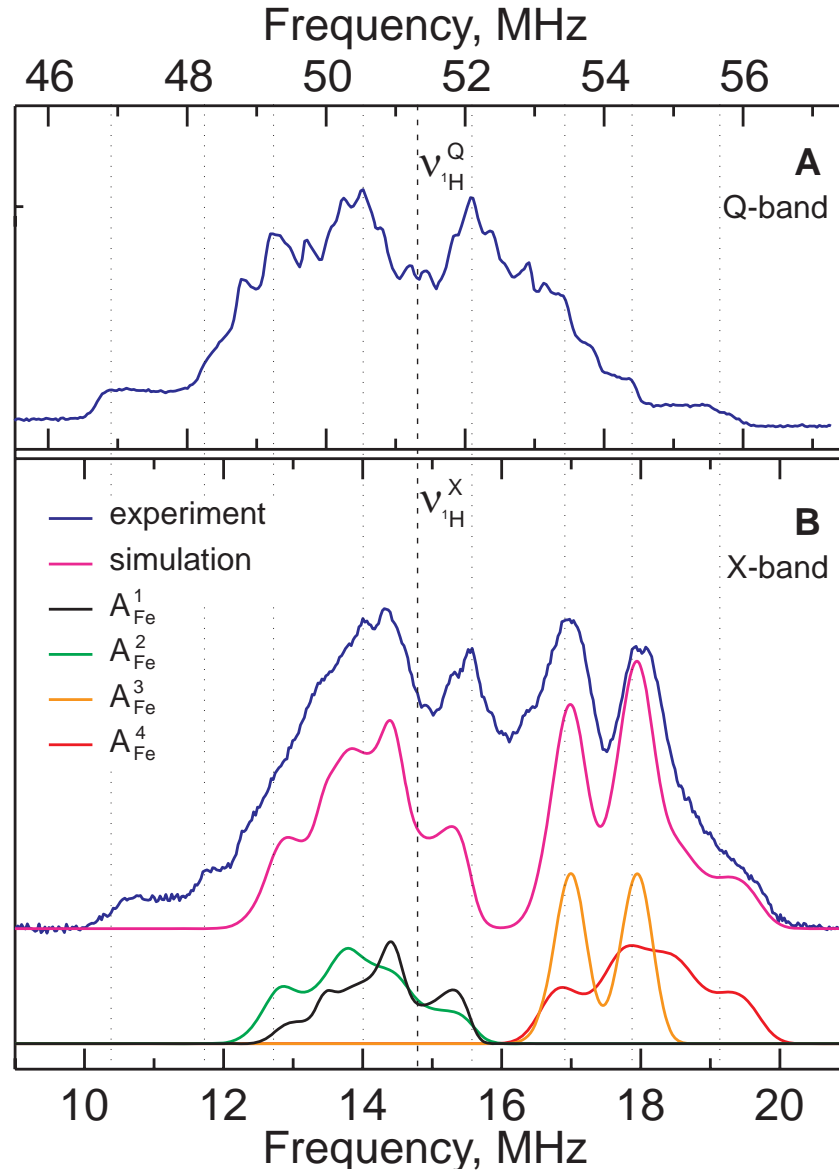


**Figure 6.5:** X-band Davies ENDOR spectrum (**B**) of the  $^{57}\text{Fe}$ -enriched [FeFe]-hydrogenase in the H<sub>ox</sub>-CO state together with interpretation in comparison with Q-band  $^1\text{H}$  Davies ENDOR spectrum (**A**). Simulation of the X-band Davies ENDOR spectrum has been performed using parameters  $A_{Fe}^{1-4}$  from table 6.1. Experimental details: **A.** temperature, 15K;  $t_{rf}$ , 19  $\mu\text{s}$ ; magnetic field, 1205 mT ( $g_2$ ); MW freq., 33.850GHz ( $\nu_{1H}^Q = 51.30\text{MHz}$ ) **B.** temperature, 15 K;  $t_{rf}$ , 7  $\mu\text{s}$ , magnetic field, 345 mT ( $g_2$ ), MW freq., 9.7473 GHz ( $\nu_{1H}^X = 14.69\text{MHz}$ ).

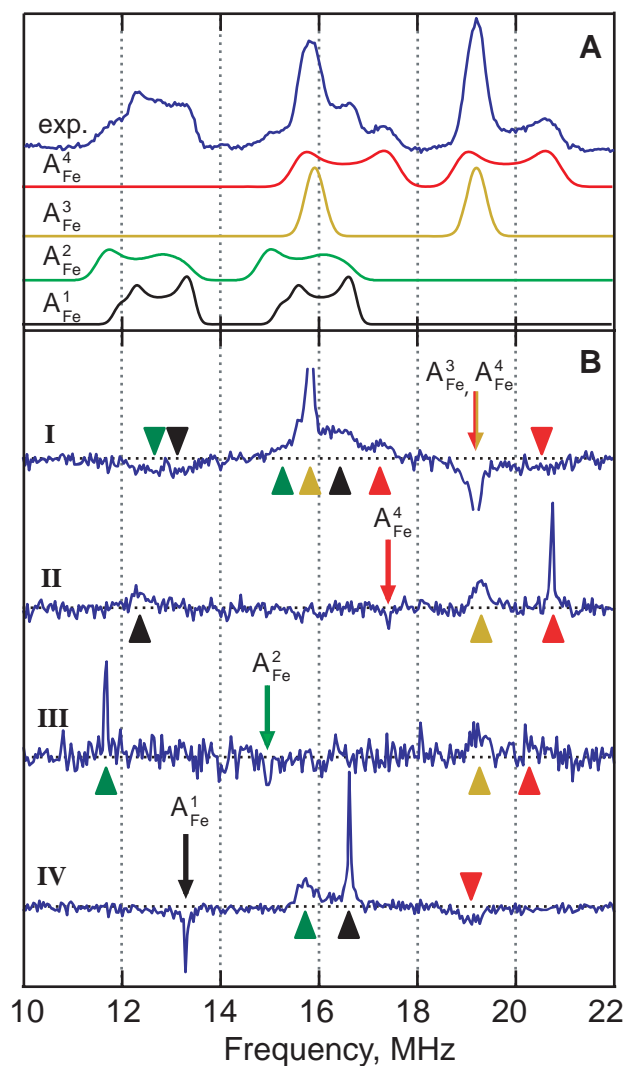


**Figure 6.6:** Q-band TRIPLE spectra of the  $^{57}\text{Fe}$ -enriched H-cluster in the  $\text{H}_{\text{ox}}\text{-CO}$  state. **A.** Q-band Davies ENDOR spectrum, taken at  $g_2$  (similar to the one, presented in figure 6.4, spectrum A) with simulated components  $A_{\text{Fe}}^1 - A_{\text{Fe}}^4$  from table 6.1. **B.** Difference TRIPLE Q-band spectra for various pump frequencies (second RF pulse), **I**: 19.19MHz; **II**: 17.40MHz; **III**: 15.00MHz; **IV**: 13.29MHz. The arrows in the plot indicate these frequencies. The color of the arrows corresponds to the HFI components of the ENDOR spectrum (spectrum **A**), which were excited. Experimental conditions: temperature, 15K; magnetic field, 1205.4mT ( $g_2$ ), length of the RF pulses, 45  $\mu\text{s}$ . The TRIPLE spectra were obtained within a 2D experiment (overall 5 traces). For one of the traces the pumping RF pulse was set to a non-resonant frequency of 25MHz. This trace was used as reference to obtain the four TRIPLE difference spectra. The random scan acquisition procedure was used in both dimensions. The triangles in **B** assign the peaks in the difference TRIPLE spectra to the HF couplings of the ENDOR spectrum using the same color code as in **A**.

been used. The first four traces of the 2D TRIPLE spectrum correspond to frequencies of the second RF pulse (pumping), resonant with <sup>57</sup>Fe nuclear spin transitions. The last value of 25MHz (for the 5<sup>th</sup> trace) is not resonant with any nuclear spin transitions and therefore this slice should be identical to a "normal" ENDOR spectrum and can be used as a reference to obtain the difference "TRIPLE" spectra (top plot in figure 6.6). The time to record a single trace in this pseudo-2D spectrum is approximately 2 min (50 shoots per point with a repetition time of 2ms). Therefore, all possible drifts of the experimental conditions are negligible on this time scale and can be considered to be averaged out in the 2D spectrum. Difference TRIPLE spectra obtained by this method are sufficiently free of any artifacts, which allow to consider even very small peaks as reliable. As well as for the 1D ENDOR experiments described above, the 2D TRIPLE spectra were obtained using random acquisition.

Difference TRIPLE spectra should reveal only signals of nuclear spin transitions originating from the same electron spin manifold ( $m_S$ ) as the nuclear spin transition excited by the first RF pulse [78]. However, according to calculations, presented in section 4.4 this may be different under certain conditions. It is possible to observe peaks, which belong to the nuclear spin transitions in the opposite electron spin manifold if the electron spin relaxation rates are comparable with length of the pulse sequence. This effect becomes more prominent with increasing length of the RF pulses and delay between them (see figure 4.11). These peaks have the opposite sign relative to the "direct" TRIPLE effect. In figure 6.6 peaks resulting from the "direct" TRIPLE effect, have negative amplitude, while the peaks due to spin relaxation effects are positive.

Spectrum II in figure 6.6.B has been measured when a NMR transition corresponding to the 4th nucleus ( $A_{Fe}^4$ ) is excited by the pump RF pulse (as shown by the arrow). This spectrum reveals three positive peaks owing to the "indirect" TRIPLE effect. Two of them (assigned to  $A_{Fe}^4$  and  $A_{Fe}^3$ ) appear on one side of the Larmor frequency and one ( $A_{Fe}^1$ ) on the other side. This indicates that the HF tensors  $A_{Fe}^4$  and  $A_{Fe}^3$  have the same sign and  $A_{Fe}^1$  has a different sign. The spectrum, which has been measured upon excitation of NMR transitions of the nuclei 3 and 4 (spectrum I), reveal peaks of both signs. Here peaks of the NMR transitions of nuclei 1 and 2 appeared on the same side of the spectrum, indicating, that the tensors  $A_{Fe}^1$  and  $A_{Fe}^2$  have the same sign. Combining these findings the following relative signs of the <sup>57</sup>Fe hfcc were elucidated:

$$\text{sign}(A_{Fe}^1) = \text{sign}(A_{Fe}^2) = -\text{sign}(A_{Fe}^3) = -\text{sign}(A_{Fe}^4)$$

Two additional TRIPLE spectra (III and IV) measured at different pumping RF frequency also confirm this conclusion.

This finding is consistent with the  $[2\text{Fe}]_{\text{H}}-[4\text{Fe}4\text{S}]_{\text{H}}$  exchange model described above in chapter 2. Therefore it is suggested, that these four  $^{57}\text{Fe}$  HF couplings represent the four iron nuclei in the  $[4\text{Fe}4\text{S}]_{\text{H}}$  subcluster. Since formally the unpaired electron resides on the bi-nuclear subcluster, one should expect to also observe HF couplings from these  $^{57}\text{Fe}$  nuclei. These may be smaller than of the cubane [64]. However, no signals have been found in the low frequency region using ENDOR spectroscopy. On the other side, the optimum length of the RF pulse is increasing with decreasing frequency. The optimum length of the RF pulse (for the Q-band setup) for measurements in region below 10 MHz is more than 150  $\mu\text{s}$  (see chapter 7). In this timescale a relaxation effects are already sufficient to decrease the ENDOR efficiency significantly. Thus it is difficult to detect very weak HF couplings. Instead, ESEEM spectroscopy is rather sensitive to small and anisotropic HF couplings and may be better suited for this study.

### 6.2.3 HYSORE study

In order to verify the occurrence of weaker  $^{57}\text{Fe}$  HF interactions in the  $\text{H}_{\text{ox}}\text{-CO}$  state Q-band HYSORE experiments were performed at various positions of the magnetic field. The HYSORE method has been chosen instead of 1D ESEEM methods because of enhanced spectral resolution and the ability to separate signals from nuclei with different HF couplings. The results of these measurements are shown in figure 6.7 together with their interpretation. As described in chapter 4, crosspeaks in HYSORE spectra corresponding to a weak hyperfine coupling ( $|A| < |2\nu_I|$ ) appear in the  $(++)/(-)$  quadrants while strong couplings ( $|A| > |2\nu_I|$ ) appear in the  $(+ -)/(- +)$  quadrants. Two  $^{57}\text{Fe}$  HF couplings can be derived from the experimental spectra. The HF parameters used in the simulations are presented in Table 6.1 (parameters  $A_{\text{Fe}}^5$  and  $A_{\text{Fe}}^6$ ). Due to the blind-spot effect, ridges belonging to strong HF interactions appear with long  $\tau$  values, while peaks corresponding to weak HF interactions are more prominent in HYSORE spectra with small  $\tau$  ( $< 350\text{ns}$ ). Here spectra, with  $\tau$ , optimized for the observation of both ridges at the same time are presented. The HYSORE spectra at the higher field position ( $g = 2.007$ ) reveal two  $^{57}\text{Fe}$  HF couplings: one crosspeak pair corresponding to a weak interaction in the  $(++)$  domain and one in the  $(+ -)$  domain, which corresponds to a strong HF interaction. The measurements at the  $g_1$  position show only one  $^{57}\text{Fe}$  ridge in the  $(++)$  quadrant, which belongs to a small hyperfine coupling. Simulations of these

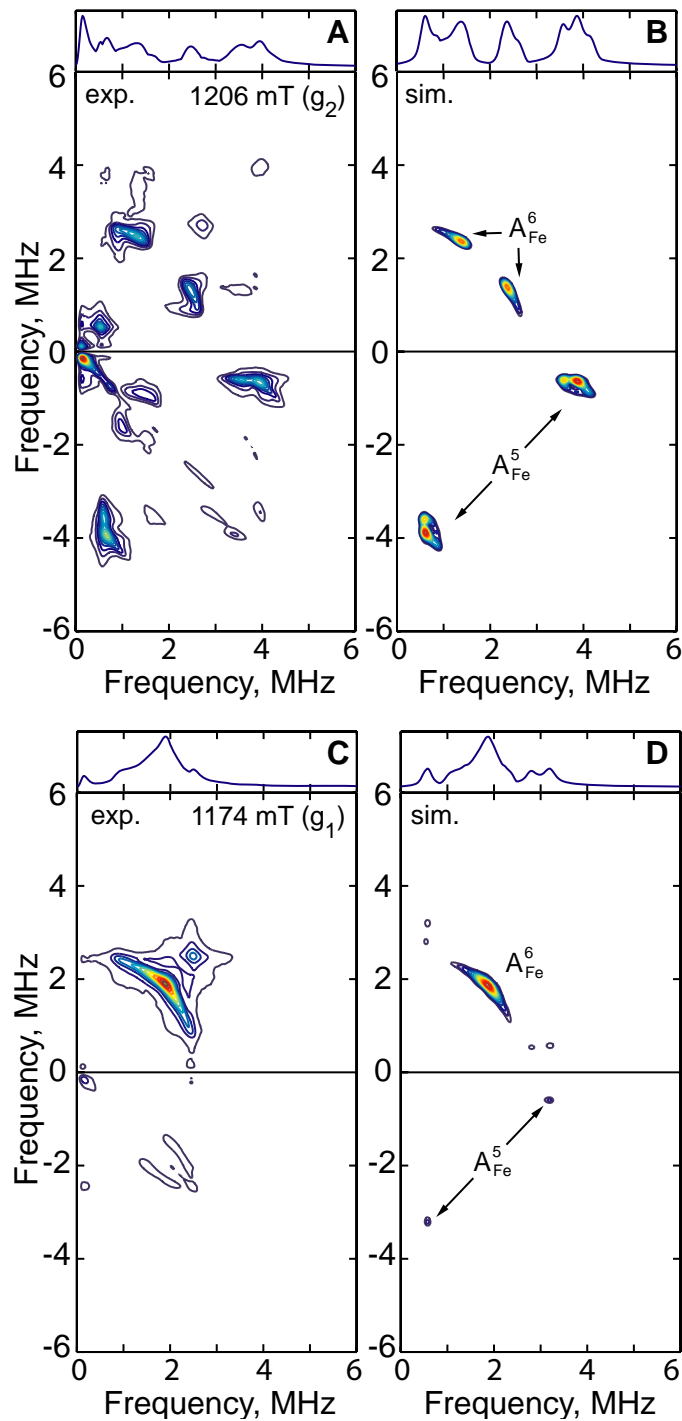


**Figure 6.7:** Q-band HYSCORE spectra of [FeFe]-hydrogenase in the  $H_{ox}$ -CO state at different magnetic field: **A.** 1206 mT ( $g_2$ ); **C.** 1174.0 mT (close to  $g_1$ ) and simulated spectra (**B,** **D**) using parameters  $A_{Fe}^5$  and  $A_{Fe}^6$  from Table 6.1. Experimental conditions: temperature, 20 K; length of all microwave pulses, 40 ns;  $\tau = 352$  ns; microwave frequency, 33.884 GHz.

## 6.2 Investigation of the $^{57}\text{Fe}$ HF couplings

**Table 6.1:** HF interaction parameters of the  $^{57}\text{Fe}$  nuclei, found for the H-cluster in the  $\text{H}_{\text{ox}}\text{-CO}$  state.

	sign	$A_{xx}$ MHz	$A_{yy}$ MHz	$A_{zz}$ MHz	$A_{iso}$ MHz	$[\varphi, \theta, \psi]$ degree
$A_{Fe}^1$	-	27.8 (2)	21.8 (2)	30.3 (2)	26.7 (2)	$[6, 110, n.d.] \pm 5$
$A_{Fe}^2$	-	26.7 (2)	23.8 (2)	30.2 (2)	27.0 (2)	$[76, -93, n.d.] \pm 7$
$A_{Fe}^3$	+	35.4 (1)	35.0 (1)	30.4 (2)	33.6 (2)	$[-(90), 185, n.d.] \pm 5$
$A_{Fe}^4$	+	34.5 (2)	38.4 (2)	30.7 (2)	34.5 (2)	$[90, 5, n.d.] \pm 20$
$A_{Fe}^5$	n.d.	5.3 (1)	4.5 (1)	2.2 (1)	4.0 (1)	$[110, 25, 44] \pm 10$
$A_{Fe}^6$	n.d.	2.1 (1)	2.1 (1)	-1.7 (1)	0.8 (1)	$[n.d., 30, 90] \pm 10$

\* Values in parantheses are uncertainties in units of the last significant digit.

correlation peaks are shown in figure 6.7 for the positions of the external magnetic field corresponding to the principal  $g$ -values. Their simulations show, that the intensity of the peaks, corresponding to the stronger HF coupling at  $g_1$  is much smaller then those of the weak HF coupling. The effect of suppression of crosspeaks of nuclear spin with small modulation depth in the presence of deep modulations due to the other coupled nuclear spin, recently described by Stoll et al.[88], can also explain observations of only signals of one nuclear spin in the  $g_1$  HYSCORE spectrum.

In addition to the ridges already mentioned above, the Q-band HYSCORE spectra also show weak background signals. They could originate from  $^{14}\text{N}$  (of the CN ligands) and their combination frequencies. However, measurements of the X-band HYSCORE spectra of various samples (see following section 6.3) do not reveal similar ridges. Therefore it cannot be excluded, that there is some contamination in the sample.

### 6.2.4 Assignment of the HF couplings to the iron nuclei

In this study two pairs of strong HF couplings with different signs have been found ( $A_{Fe}^{1-4}$  in table 6.1). According to the theoretical model, described in chapter 1 one expects to find two pairs of strong  $^{57}\text{Fe}$  HF couplings with opposite signs for the case of strong  $[2\text{Fe}]_{\text{H}}\text{-}[4\text{Fe}4\text{S}]_{\text{H}}$  exchange. Therefore, these couplings are assigned to the  $[4\text{Fe}4\text{S}]_{\text{H}}$  subcluster. This conclusion is also supported by earlier Mössbauer studies on *C. pasteurianum* [52] and *D. vulgaris* Hildenborough [60], which have shown similar hfccs and a similar assignment. The two rather small HF couplings ( $A_{Fe}^{5,6}$  in table 6.1) found by

HYSCORE spectroscopy are assigned to the bi-nuclear subcluster.

From the study presented in chapter 7 as well as from earlier studies it is known, that in the case of the H<sub>ox</sub> state the [2Fe]<sub>H</sub>-[4Fe4S]<sub>H</sub> exchange interaction is weaker than in the H<sub>ox</sub>-CO state. In order to increase the exchange interaction, it is necessary to shorten the exchange pathway or, in other words, shift unpaired spin towards the [4Fe4S]<sub>H</sub> subcluster. It has been found in this study, that the unpaired electron is more localized on one of the iron nuclei of the bi-nuclear subcluster. Therefore it seems likely that the larger of the two HF couplings ( $A_{Fe}^5$ ) is associated with the proximal iron which forms the connection to the [4Fe4S]<sub>H</sub> subcluster while the weak almost dipolar HF coupling ( $A_{Fe}^6$ ) should be assigned to the distal iron.

Although there is no clear evidence, which particular HF coupling belongs to which iron nucleus in the 'cubane' subcluster, some indication could be obtained from considering the orientations of the HF tensors in the structure. It should be noted that the uncertainty ranges of the determined Euler angles are moderately large. However they do provide certain constraints, which allow a first attempt to relate the <sup>57</sup>Fe HF tensor orientations to the crystal structure of the H-cluster in the H<sub>ox</sub>-CO state [26]. The alignment of the local axes of the HF tensors was facilitated using a home-written program in MATLAB<sup>TM</sup>. The atomic coordinates were taken from the geometry-optimized structure of the H-cluster in the H<sub>ox</sub>-CO state, presented by Fiedler et al. [97].

The g-tensor was found to be almost axial ( $g_1 = 2.065$ ,  $g_2 = 2.007$ ,  $g_3 = 2.001$ ). Therefore the value  $g_1$  can be assigned to the 'z' component. The orientations of the HFI-tensors can only be partially defined through our experimental analysis (see table 6.1). In addition, there are several combinations of  $\varphi$  (rotation around z axis) and  $\theta$  (rotation around y' axis) which merely permute the order of the principal components, i.e. applying a rotation with  $\varphi = 90^\circ$  and  $\theta = 90^\circ$  results in a cyclic permutation of the principal axes. Finally, the weak HF coupling originating from the bi-nuclear subcluster has axial symmetry, which allows additional rotation freedom by  $\varphi$ . On the other hand the orientation along the z-axis ( $\theta$ ) for each tensor can be determined quite accurately. Since angles of all HF tensors are defined with respect to the principal axes of the g-tensor, it is important to align the g-tensor to the structure first.

Since the electronic structure of the H<sub>ox</sub>-CO state is dominated by the strong exchange interaction between the [2Fe]<sub>H</sub> subcluster and one of the iron atoms of the cubane it is reasonable to assume that the vector connecting the subclusters represents a local symmetry axis defining the 'z' axis of the g-tensor.

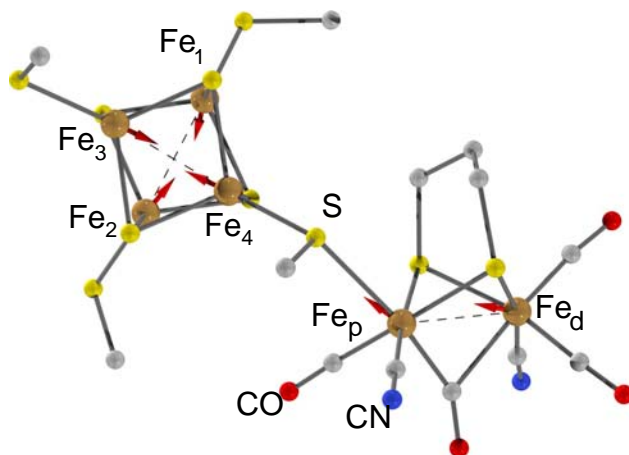


**Figure 6.8:** Schematic representation of the orientation of the  $^{57}\text{Fe}$  HF tensors in the structure of the H-cluster in the  $\text{H}_{\text{ox}}\text{-CO}$  state. The red arrows represent the "z" axis of the  $^{57}\text{Fe}$  HF tensors. The coordinates are taken from the geometry-optimized structure of the H-cluster in  $\text{H}_{\text{ox}}\text{-CO}$  state [97].

It was found that the 'z'-components of the HF tensors of the pair of irons with the largest HF couplings ( $A_{\text{Fe}}^3$  and  $A_{\text{Fe}}^4$ ) in the  $[\text{4Fe4S}]_{\text{H}}$  subunit are almost collinear with each other and with the z-axis of the g-tensor. At the same time, the "z" components of the  $^{57}\text{Fe}$  HF couplings of the  $A_{\text{Fe}}^1 - A_{\text{Fe}}^2$  pair appears to be oriented perpendicular to the other pair. This suggests that the tensor orientations follow the local symmetry of the 'cubane' such that the "z" components of the HF tensor are oriented along the diagonals connecting the iron pairs. There are three ways to combine four irons in the  $[\text{4Fe4S}]_{\text{H}}$  subcluster into two pairs. However, an additional restriction can be derived from the alignment of the HF tensor of the proximal iron ( $A_{\text{Fe}}^5$ ). Because of the strong  $[\text{2Fe}]_{\text{H}} - [\text{4Fe4S}]_{\text{H}}$  exchange interaction, the "z" axis of this tensor should be collinear with the  $\text{Fe}_p\text{-S}_{\text{cys}}$  bond. This is confirmed by recent DFT calculations [97]. Since this HF tensor was determined with good accuracy (all three Euler angles were defined), its alignment can decrease the number of possibilities for the arrangement of the g-tensor in the molecular structure and therefore help in the assignment of the HF tensors to the irons in the 'cubane'. Combination of all these arguments suggests that the pair of strong HF couplings ( $A_{\text{Fe}}^3$  and  $A_{\text{Fe}}^4$ ) are belonging to the other pair  $\text{Fe}_3\text{-Fe}_4$  and thus the pair of HF tensors ( $A_{\text{Fe}}^1$  and  $A_{\text{Fe}}^2$ ) to  $\text{Fe}_1\text{-Fe}_2$  (see figure 6.8).

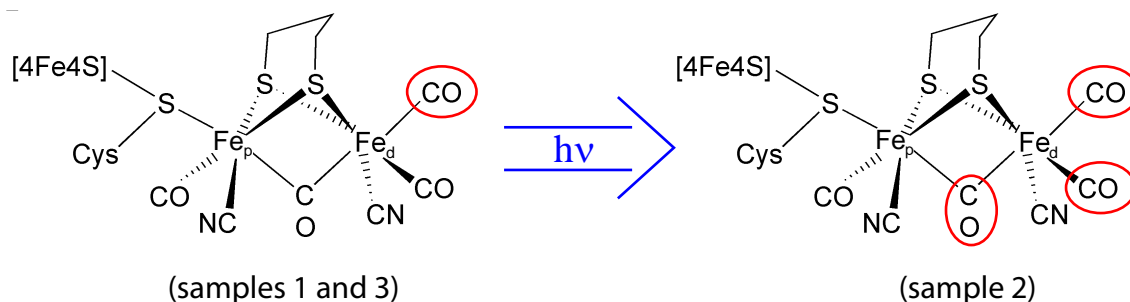


**Figure 6.9:** Effect of illumination of singly  $^{13}\text{C}$  labeled H-cluster in H<sub>ox</sub>-CO state, according to recent investigation of this process by CW EPR and IR spectroscopy [38, 47]. Red circles represent CO ligands, labeled by  $^{13}\text{C}$  isotopes.

### 6.3 Investigation of the $^{13}\text{C}$ HF couplings of the CO ligands

#### 6.3.1 Labeling by $^{13}\text{C}$ isotope

In this section the investigation of the  $^{13}\text{C}$  HF couplings of the CO ligands is presented. Labeling of the H-cluster by  $^{13}\text{C}$  isotopes has been performed using a property of the H-cluster, described recently by Albrach et al [38, 47]. It was shown, that if the H<sub>ox</sub>-CO state with the  $^{13}\text{C}$  labeled external CO bond is illuminated at temperature of 2<sup>o</sup>C, the IR bands corresponding to the other two CO ligands of the distal iron (Fe<sub>d</sub>) are changing. Therefore it was concluded, that the two intrinsic CO ligands to the Fe<sub>d</sub> were exchanged with the extrinsic  $^{13}\text{CO}$ , whereas the terminally-bound CO on Fe<sub>p</sub> was unaffected (see figure 6.9). After illumination for 4 hours under 95% H<sub>2</sub> and 5%  $^{13}\text{CO}$  atmosphere FT-IR measurements reveal labeling of all CO ligands of the distal iron with 56% efficiency.

For this study, several samples were prepared. The first sample has been prepared under  $^{13}\text{CO}$  atmosphere and therefore has only the external CO labeled. The second sample has been first prepared in the same manner, as sample 1. Then it was illuminated using the procedure described by Albracht et. al [47](at a temperature of 2<sup>o</sup>C (on ice) for 4 hours). Both samples were provided by Prof. Albracht and were used for X-band measurements. Sample 3 has been prepared separately. As isolated enzyme was activated using H<sub>2</sub> gas (continuous flushing for 15 min) and then converted to the oxidized state by flushing with Ar gas for 15min. After that it was placed under  $^{13}\text{CO}$  atmosphere for 20min. Thus, the singly  $^{13}\text{C}$ -labeled H<sub>ox</sub>-CO state similar to the sample 1 was obtained. This sample was used for Q-band experiments.

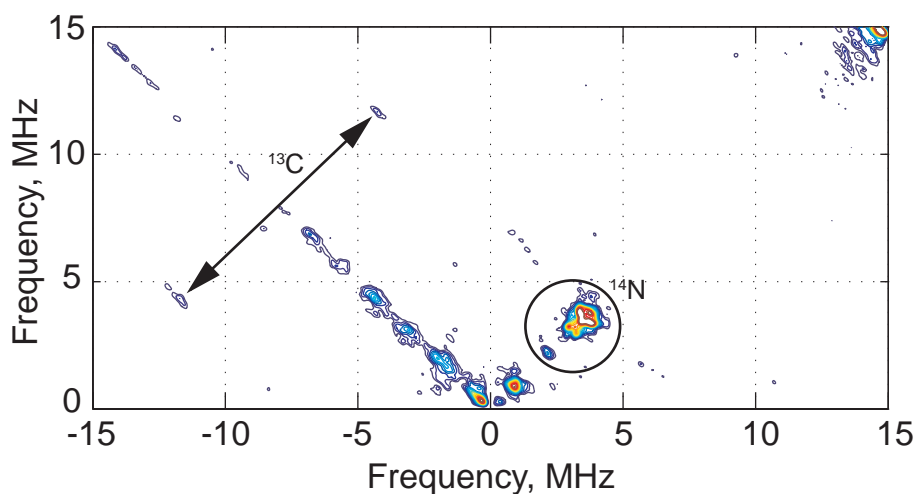


**Figure 6.10:** X-band HYSCORE spectrum of the  $^{13}\text{C}$ -enriched H-cluster in the  $\text{H}_{\text{ox}}\text{-CO}$  state (sample N1) measured at  $g_2$ . The enzyme in the active form has been flashed with  $^{13}\text{CO}$  gas in order to obtain the  $\text{H}_{\text{ox}}\text{-CO}$  state. No illumination has been performed. Experimental details: temperature, 15K; MW freq., 9.7607GHz; magnetic field, 346.9 mT;  $\tau = 120$  ns;  $t_{\text{mw}}^{\pi/2} = 8$  ns.

### 6.3.2 HYSCORE measurements

X-band HYSCORE spectroscopy turned out to be most suitable for the observation of the  $^{13}\text{C}$  HF couplings, since in 1D spectra (i.e. ENDOR and 3pulse ESEEM) the signals from  $^{13}\text{C}$  nuclei are overlapping with quite broad  $^1\text{H}$  signals as well as with spectra of  $^{14}\text{N}$  nuclei.

In figure 6.10 the obtained HYSCORE spectrum of sample 1 is presented. All spectra, shown in this section are zoomed to a maximum frequency of 15 MHz, excluding the  $^1\text{H}$  signals from the plot in order to simplify the presentation. All experiments were done at a temperature of 20K using the shortest possible  $\tau$  value of 120 ns. The HYSCORE spectra of sample 1 show only one pair of ridges in the (+-) quadrant in the 2D spectra, which can be assigned to  $^{13}\text{C}$ . These ridges are more prominent at high magnetic field ( $g_3, g_2$ ). They shift to higher frequency at lower magnetic fields and completely vanish at low field ( $g_1$ ). This indicates a large anisotropy of the HF tensor. From these measurements, the HF coupling constants were estimated to be about 16 MHz (at  $g_3, g_2$ ) and up to 19MHz (at  $g_1$ ). However, since at the low magnetic field position ( $g_1$ ), these peaks could not be observed this estimation is only approximate.

The second sample, with the redistributed  $^{13}\text{CO}$  ligands at the distal iron, reveals in

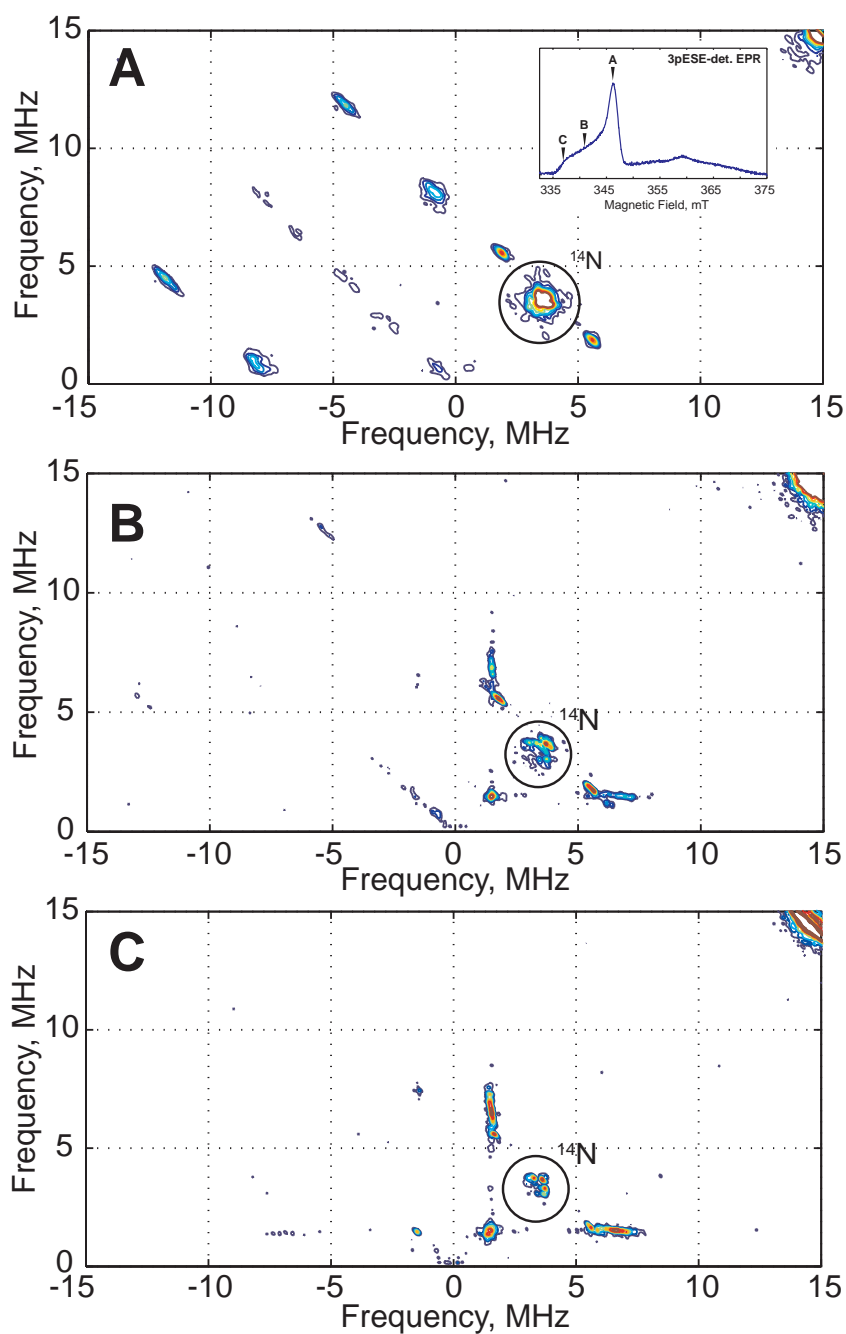


**Figure 6.11:** X-band HYSCORE spectra of the  $^{13}\text{C}$ -enriched H-cluster in the H<sub>ox</sub>-CO state (sample 2). After inhibition of the enzyme in the H<sub>ox</sub> state by  $^{13}\text{CO}$  gas, the sample has been illuminated for 4 hours at 20°C. Experimental details: temperature, 15K;  $\tau = 120\text{ns}$ ; **A:** Frequency, 9.758 GHz; magn.field, 346.5 mT ( $g_2$ ); **B:** Frequency, 9.747GHz; magn.field, 341.5 mT; **C:** MW freq., 9.757Hz; magn.field, 338.2 mT ( $g_1$ ). Ridges, assigned to the  $^{14}\text{N}$  nuclei are marked with circles. The insert in plot A represents the X-band 3-pulse-ESE- detected EPR spectrum of the H<sub>ox</sub>-CO state, measure at the same experimental conditions as the HYSCORE spectra.

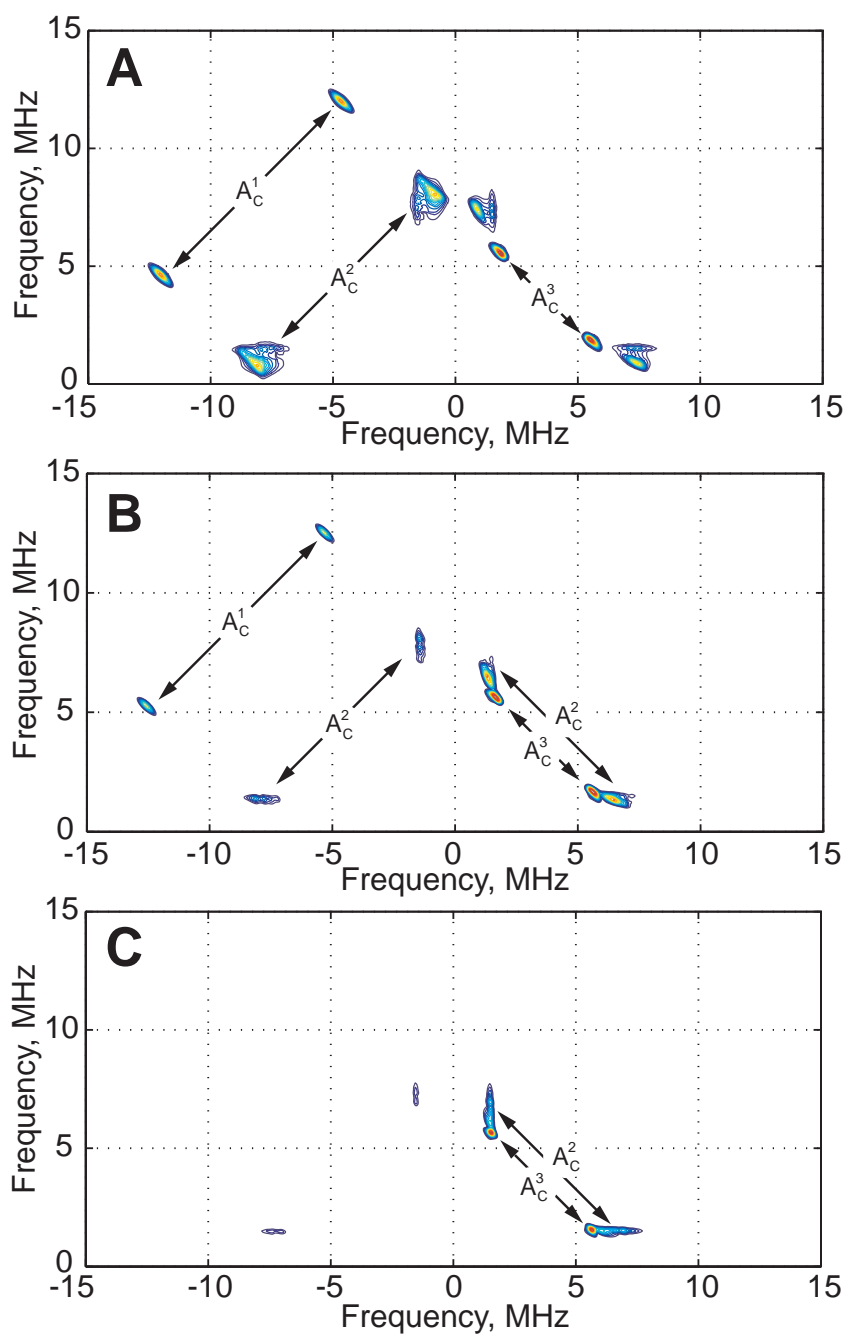


**Figure 6.12:** Simulated HYSORE spectra of the  $^{13}\text{C}$ -enriched H-cluster in the  $\text{H}_{\text{ox}}\text{-CO}$  state, calculated using parameters  $A_c^{1-3}$  from table 6.2. Simulation parameters according to experimental conditions:  $\tau = 120\text{ns}$ ; Frequency, 9.75 GHz; **A:** magn.field, 346.5 mT ( $g_2$ ); **B:** magn.field, 341.5 mT; **C:** magn.field, 338.2 mT ( $g_1$ ).

total 3 different pairs of ridges in the X-band HYSCORE spectra, which can be assigned to <sup>13</sup>C nuclei as expected from earlier IR studies. In addition to the coupling, which was already observed in sample 1, two additional pairs of signals were found. The HYSCORE spectrum, measured at the  $g_2$  position of the magnetic field (figure 6.11) clearly shows all three pairs of ridges separately. However, in the  $g_1$  position the strong HF coupling ( $A_C^1$ ) is too large to be observed while two other nuclei reveal ridges in the same part of the spectrum. This makes the interpretation of the experimental data less accurate. To improve the interpretation, measurements at an intermediate position of the magnetic field were performed (figure 6.11/6.12,B). In this spectrum all ridges are visible and separated, which increases the accuracy of the determined HF couplings. Since,  $g_2$  and  $g_3$  are not resolved in the X-band EPR spectrum the "hard" MW pulses select almost all orientations in the region of  $g_2$  and  $g_3$ . Therefore, additional measurements at  $g_3$  were omitted. In addition to the observed <sup>13</sup>C signals, further ridges along the diagonal of the (++) quadrant were found and assigned to <sup>14</sup>N nuclei. These peaks have been found in all X-band HYSCORE spectra of the H-cluster in the H<sub>ox</sub>-CO state (for all measured samples). The position of the ridges suggests a weak anisotropic HF interaction. The value of the quadruple interaction ( $K$ ) was estimated to be around 1 MHz, which is similar to what was found for cyanide ligands of low-spin irons [98]. The dipolar part of the HF interaction was estimated to be approximately 0.5 MHz. However, due to the poor spectral resolution a detailed analysis of these peaks was not been performed.

### 6.3.3 Q-band ENDOR measurements

In order to verify a value of the  $A_C^1$  HF coupling constant Q-band Davies ENDOR experiments have been performed. At Q-band frequency, signals from <sup>13</sup>C nuclei are well separated from those of <sup>14</sup>N and <sup>1</sup>H nuclei, making the interpretation much easier. Figure 6.13 shows the results of the ENDOR study on sample 3 (only the external CO ligand is <sup>13</sup>C labeled). At the low field position ( $g_1$ ) the S/N ratio of the obtained ENDOR spectrum is quite low. Moreover, the spectrum contains several broad artifacts despite the use of random acquisition. Therefore, spectra at several intermediate positions of the magnetic field were recorded in order to increase the precision of the determined hfcc. Figure 6.13 presents these spectra together with simulations using parameters  $A_C^1$  from table 6.2.

### 6.3.4 Assignment

The resulting HF coupling constants, obtained from the combined study presented above are summarized in table 6.2. It is well known that, if the active enzyme is placed

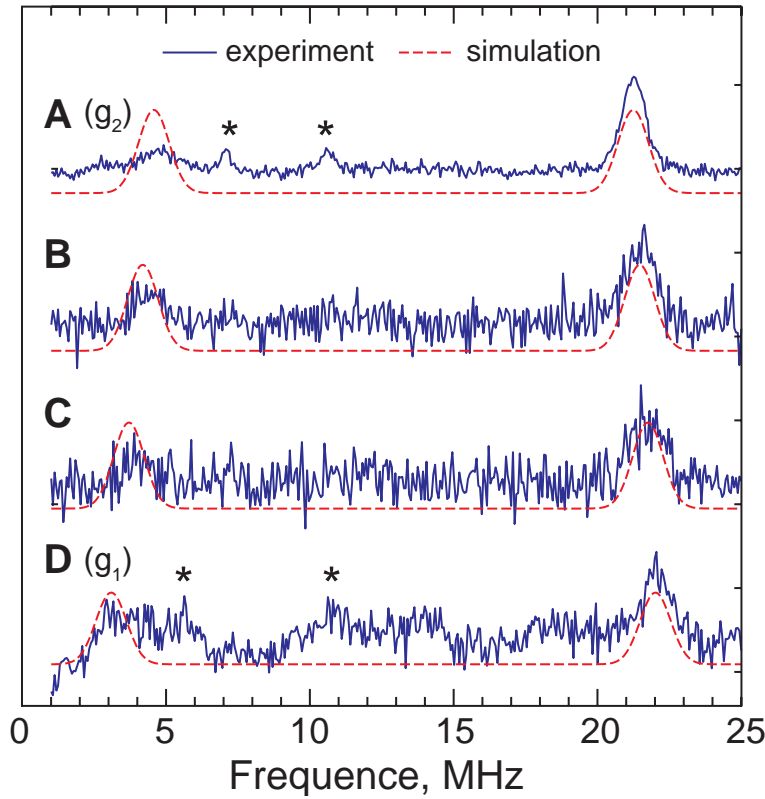


**Figure 6.13:** Q-band ENDOR spectra of the  $^{13}\text{C}$ -enriched H-cluster in the  $\text{H}_{\text{ox}}$ -CO state (sample 3), measured at various positions of the external magnetic field. Experimental conditions: temperature, 15 K;  $t_{rf} = 45\mu\text{s}$ ;  $t_{mw}^{inv} = 100\text{ns}$ ; magnetic field, **A**. 1205.0 mT ( $g_2$ ); **B**. 1193.9 mT; **C**. 1182.9 mT; **D**. 1171.8 mT ( $g_1$ ). Simulation has been performed using set of parameters  $A_C^1$  from table 6.2. Asterisks (\*) marks artifacts due to experimental setup.

**Table 6.2:** Parameters of the HF interaction of the  $^{13}\text{C}$  nuclei, found for the  $\text{H}_{\text{ox}}$ -CO state of the H-cluster.

	$A_{xx}$ (MHz)	$A_{yy}$ (MHz)	$A_{zz}$ (MHz)	$A_{iso}$ (MHz)	$[\varphi, \theta, \psi]$ (deg)
$A_C^1$	16.6 (2)	16.6 (2)	19.0 (2)	17.4 (2)	$[0, 0, 0] \pm 60$
$A_C^2$	10.3 (3)	8.4 (3)	4.0 (3)	7.7 (3)	$[0, 20, 0] \pm 30$
$A_C^3$	3.2 (3)	3.5 (3)	4.7 (3)	3.8 (3)	$[30, 0, 0] \pm 30$

\* Values in parantheses are uncertainties in units of the last significant digit.

under CO containing atmosphere, carbon monoxide blocks the external site of the distal iron [34, 38, 47]. Since the strongest HF coupling ( $A_C^1$ ) has been detected in both illuminated and non-illuminated  $^{13}\text{C}$ -labeled samples, it has been assigned to the external CO ligand of the distal iron  $\text{Fe}_d$ , (see figure 6.1). For two other HF couplings ( $A_C^2$  and  $A_C^3$ ) no direct assignment could be done. However, some conclusions can be made from the size and symmetry of these two HF couplings.

As it follows from table 6.2, HF coupling  $A_C^2$  is relatively strong and quite anisotropic with a rhombic character, while  $A_C^3$  is much weaker and mostly axial. In previous section it has been shown, that the iron nuclei in the bi-nuclear subcluster carry spin-density in non equal proportions. Hence the nuclear spin of the  $^{13}\text{C}$  of the bridging CO ligand most probably experiences not equal HF interaction in directions of the  $\text{Fe}_p$  and  $\text{Fe}_d$ . Consequently it is logical to assume, that the observed 'rhombic'  $^{13}\text{C}$  HF coupling ( $A_C^2$ ) corresponds to carbon in the bridging CO ligand while the almost 'axial'  $^{13}\text{C}$  HF coupling ( $A_C^3$ ) must be assigned to the intrinsic CO ligand of the distal iron.

## 6.4 Discussion

### 6.4.1 The spin-coupling model

The signs and magnitudes of the determined  $^{57}\text{Fe}$  HF couplings have been analyzed using a theoretical model assuming that a single center with spin  $S = 1/2$  is exchanged coupled to one of the iron atoms of the diamagnetic  $[\text{4Fe-4S}]^{2+}$  cluster [52, 60]. The  $[\text{4Fe-4S}]^{2+}$  cluster consists of two pairs of high spin Fe(II) and Fe(III) centers. Each Fe(II)Fe(III) pair, with delocalized valences, in the 'cubane' has a total spin of  $9/2$  [63, 64]. The strong coupling between the two pairs leads to a  $S = 0$  ground state (singlet) for the  $[\text{4Fe-4S}]_{\text{H}}^{2+}$  cluster with an  $S = 1$  excited state (triplet) at energy distance  $\Delta$ . The exchange coupling ( $j$ ) of the  $S = 1/2$  center to one of the iron atoms of the 'cubane' cluster leads to a mixing of the ground (singlet) and first excited (triplet) states of the 'cubane' (S-T mixing). The strength of this mixing, and consequently the HF coupling of the iron nuclei of the 'cubane', depends on the ratio  $j/\Delta$ . The model predicts that the signs of the HF interactions corresponding to the two Fe(II)Fe(III) pairs are opposite. This is exactly what has been found in this study for the couplings observed in the H<sub>ox</sub>-CO state (see table 1) using TRIPLE experiments. The H<sub>ox</sub>-CO state is characterized by a strong S-T mixing (caused by an increased electronic exchange coupling) leading to  $^{57}\text{Fe}$  HF couplings, which are a factor of three larger than those of the H<sub>ox</sub> state (see next chapter). It should

be noted that our observations also indicate that the exchange-coupling model described above needs some refinements in order to fully describe the electronic structure of the H cluster. Firstly, the model is not taking into account the presence of the distal iron, which apparently also carry some spin density. Secondly, the fact that the four observed HF couplings from the 'cubane' are all different shows that the symmetry of the  $[4\text{Fe-4S}]_{\text{H}}^{2+}$  subcluster is lower than  $D_{2d}$ , which is the starting assumption for the spin coupling model of the  $[4\text{Fe-4S}]^{2+}$  cluster [63].

#### 6.4.2 Oxidation states of the iron atoms in $[2\text{Fe}]_{\text{H}}$ -subcluster

In the literature there is still some debate about the possible redox states of the bi-nuclear iron cluster in the various catalytic states. Inorganic model systems of the bi-nuclear subcluster [61] show that in the completely reduced state the Fe(I)Fe(I) arrangement is very stable. These findings have also been confirmed by quantum chemical calculations [57, 62]. On the other hand, the Mössbauer studies on the H cluster suggest a Fe(II)Fe(II) arrangement although a Fe(I)Fe(I) configuration could not be completely ruled out [60]. The current data clearly indicate that the proximal iron atom must be formally paramagnetic in order to give rise to the extensive electron exchange interaction with the  $[4\text{Fe4S}]_{\text{H}}$  subcluster. At the same time, IR studies [38, 47] have shown that the CO stretch vibration of the CO bound to the proximal iron is not sensitive to any manipulation to the H-cluster, i.e. it remains at  $1964\text{ cm}^{-1}$  in the  $\text{H}_{\text{ox}}$  and the  $\text{H}_{\text{red}}$  state as well as the  $\text{H}_{\text{ox}}$ -CO state. This indicates that the redox transition when going from the  $\text{H}_{\text{ox}}$  to the  $\text{H}_{\text{red}}$  state occurs at the distal iron. This would make sense if the reaction with molecular hydrogen is initiated at the open coordination site of  $\text{Fe}_d$ . Since the proximal iron is paramagnetic in the  $\text{H}_{\text{ox}}$  and  $\text{H}_{\text{ox}}$ -CO state its redox state can only be Fe(I), since in the Fe(III) case the reduction of the H cluster would have to take place at the proximal iron under change of redox state which would be inconsistent with the IR data. Therefore, combining the ENDOR, HYSCORE, Mössbauer and IR data enables us to conclude that during the catalytic cycle the bi-nuclear subcluster shuttles between the  $\text{Fe(I)}_p\text{Fe(I)}_d$  and  $\text{Fe(I)}_p\text{Fe(II)}_d$  state.

# 7

## The H<sub>ox</sub> state of the H-cluster

---

Figure 7.1 shows the schematic structure of the H-cluster in the H<sub>ox</sub> state, which has been proposed by X-ray crystallography together with IR studies of the active site of [FeFe] hydrogenase from both *D. desulfuricans* and *C. pasteurianum* [25, 26, 32]. Besides nitrogens on the cysteines, coordinating [4Fe4S]<sub>H</sub> subcluster there are two nitrogen atoms in the H-cluster. These are from CN ligands of the Fe atoms in bi-nuclear subcluster.

Investigation of the electronic structure of the H<sub>ox</sub> state has been performed by studying interactions of two types of nuclei: <sup>57</sup>Fe and <sup>14</sup>N. The <sup>57</sup>Fe HF couplings in the H-cluster of the [FeFe] hydrogenase from *C. pasteurianum* were investigated extensively by various EPR and Mössbauer methods in the past [48, 49, 52]. Comparison of the <sup>57</sup>Fe HF couplings of this active site with those of the hydrogenase from *D. desulfuricans*, which is studied here, can provide an idea about possible differences between the H-clusters. In order to improve the knowledge about the distribution of the unpaired electron over the bi-nuclear subcluster of the H-cluster, a study of the <sup>14</sup>N nuclear spin couplings has been performed. The obtained information about electronic structure of the H-cluster can be used as an input parameters for theoretical investigations such as DFT.

Recently it has been proposed that the dithiol bridging ligand also contains a nitrogen atom ('X' in the figure 7.1) i.e. HS-CH<sub>2</sub>-NH-CH<sub>2</sub>-SH [35, 99]. This suggestion is based on the similarity of the Ni coordination of the active site of Ni-Fe hydrogenase and nitrogen of the DTN of the H-cluster. Indeed, from mechanistic considerations it is preferable that nitrogen is the central atom in the dithiol ligand because it would form a secondary amine that is able to extract the proton resulting from the heterolytic cleavage of H<sub>2</sub>.

### 7.1 CW EPR spectra of non-labeled samples

Figure 7.2 shows a comparison of the typical EPR spectrum of the "H<sub>ox</sub>" sample with the spectrum of the H<sub>ox</sub>-CO state and the reduced enzyme (H<sub>red</sub>). The H<sub>ox</sub> state shows a well known rhombic EPR spectrum ( $S = 1/2$ ) characterized by the principal g-values:

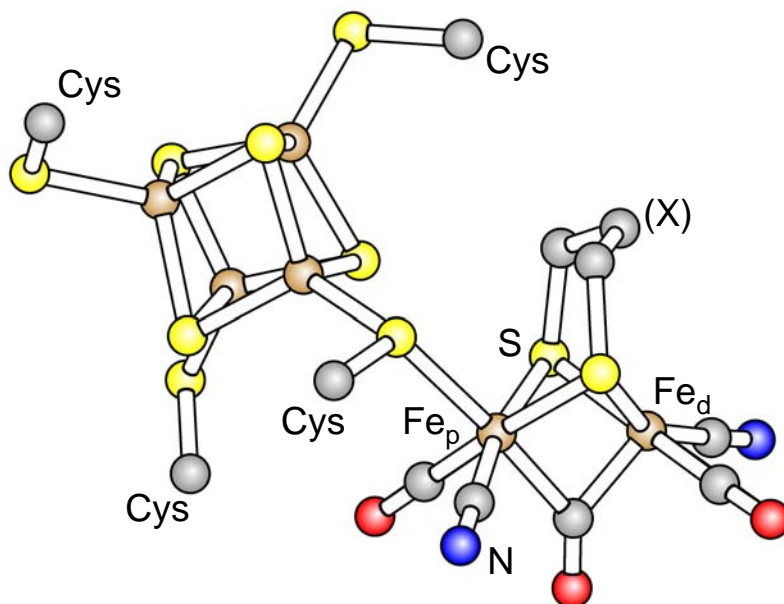


**Figure 7.1:** Schematic representation of the H-cluster in the  $H_{ox}$  state. Coordinates of the H-cluster were obtained from structure of the [FeFe]-hydrogenase from *D.desulfuricans* [25] (Protein Data Bank entry **1hfe**).

$g_1 = 2.100$ ,  $g_2 = 2.040$ ,  $g_3 = 1.999$  [24, 48, 50]. In the reduced state the H-cluster is EPR silent and the observed EPR signals is owing to the reduced dipolar-coupled F-clusters [38, 50]. Therefore it can be used to disentangle the spectrum of the " $H_{ox}$ " sample. As follows from the analysis, the spectrum of the sample with the [FeFe] hydrogenase in the  $H_{ox}$  state shows some contaminating signals with characteristic  $g$ -values similar to the ones of the  $H_{ox}$ -CO state as well as a signal of quite complicated shape resulting from the dipolar-coupled reduced F-clusters.

Albracht et al. [38, 47] have recently shown that oxidative and light damage to the protein leads to "cannibalism" among the H-clusters in which the CO ligands of damaged H-clusters are captured by intact ones leading to the formation of CO-inhibited ( $H_{ox}$ -CO) species.

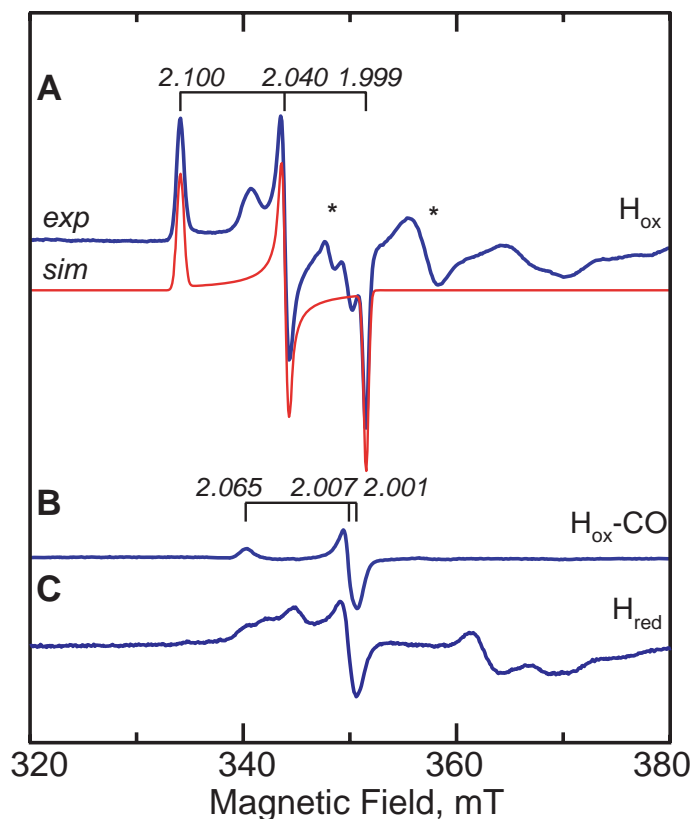


**Figure 7.2:** CW EPR spectra of the enzyme from *D. desulfuricans* in the  $H_{ox}$  (A),  $H_{ox}$ -CO (B) and  $H_{red}$  (C) states. Panel A consists of the experimental spectrum together with simulation using the principal g-values, presented on the top of the plot. All spectra were taken using unsaturated conditions. Experimental conditions: **A**) temperature, 40K; MW freq., 9.825GHz; MW power,  $63.26\mu W$  (35dB); mod.amp., 3G; mod.freq. 100kHz. **B**) temperature, 40K; MW freq., 9.530GHz; MW power,  $20\mu W$  (40dB); mod.amp., 5G; mod.freq. 70kHz. **C**) temperature, 20K; MW freq., 9.638GHz; MW power, 2mW (20dB); mod.amp., 7.46G; mod.freq. 100kHz. The X-axes of the spectra B and C are adjusted to spectrum A, in order to provide a direct comparison. Spectra A and B were obtained on the X-band ELEXSYS E580 spectrometer in continuous-wave mode. Spectrum C was obtained using the X-band ELEXSYS E500 CW EPR spectrometer.

## 7.2 Investigation of the $^{57}Fe$ HF couplings

### 7.2.1 Pulse ENDOR study

Labeling of the enzyme was facilitated by growing the organism in a  $^{57}Fe$ -enriched medium, as described in the "material and methods". Figure 7.3 shows the Q-band FID-detected EPR spectrum of the active oxidized state ( $H_{ox}$ ) of the  $^{57}Fe$ -enriched H-cluster recorded at 15K. To facilitate comparison with CW EPR spectra the pseudo-

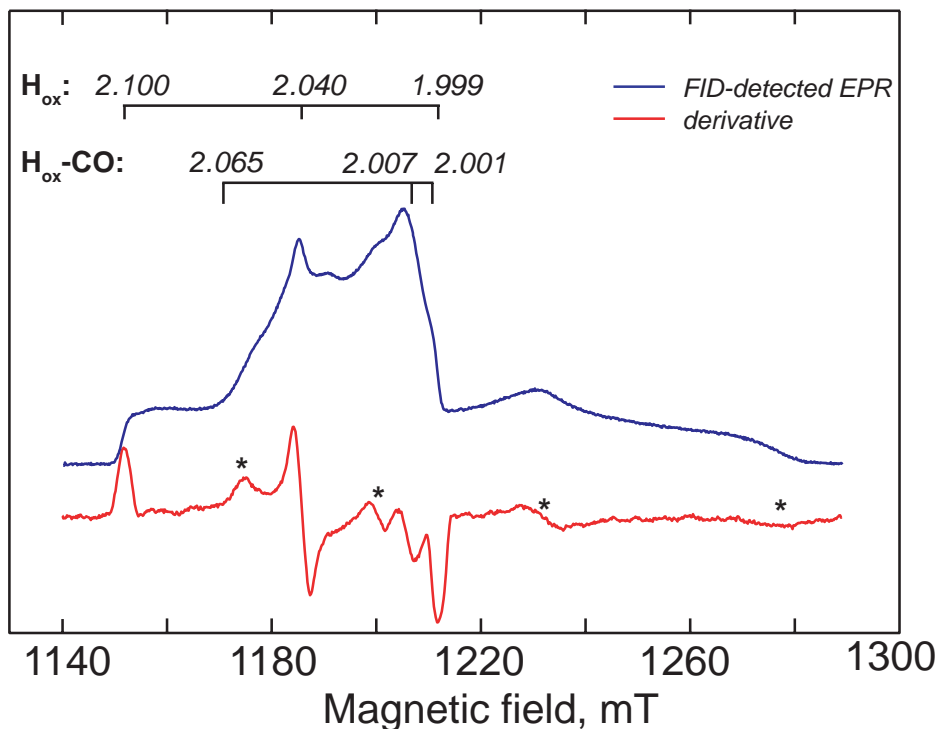


**Figure 7.3:** Q-band FID detected EPR spectrum of the H-cluster in the  $H_{ox}$  state and its derivative (pseudomodulation). Asterisks (\*) indicate contaminating signals from dipolar-coupled F-clusters. Experimental conditions: temperature, 20 K; MW freq., 33.86 GHz; length of the MW pulse  $t_{mw}$ , 500 ns. The pseudo-modulated spectrum has been obtained using a modulation amplitude of 1.0 mT.

modulated spectrum is also shown. As observed at X-band frequency, the pulse Q-band EPR spectrum of the  $H_{ox}$  state reveal three overlapping components, attributed to  $H_{ox}$ ,  $H_{ox-CO}$  and reduced F-clusters.

From the investigation of the  $^{57}\text{Fe}$  HF couplings in the active site of the [FeFe] hydrogenase II (uptake) from *C.pasteurianum*, it was expected to find strong HF couplings around 8 and 17 MHz [48, 49, 52, 100]. Therefore, the Davies ENDOR sequence was used as a main method for the investigation of the  $^{57}\text{Fe}$  HF couplings in the  $H_{ox}$  state. Because of better spectral resolution and good separation from the  $^1\text{H}$  signals, the experiments were performed at Q-band. The Q-band Davies ENDOR spectra reveal two separate sets of peaks which can be attributed to  $^{57}\text{Fe}$  nuclei (frequency range of 1-20 MHz), as it is shown in figure 7.4. These spectra have been obtained using the settings, optimized for observations of the high frequency peaks (around 19 MHz). In the

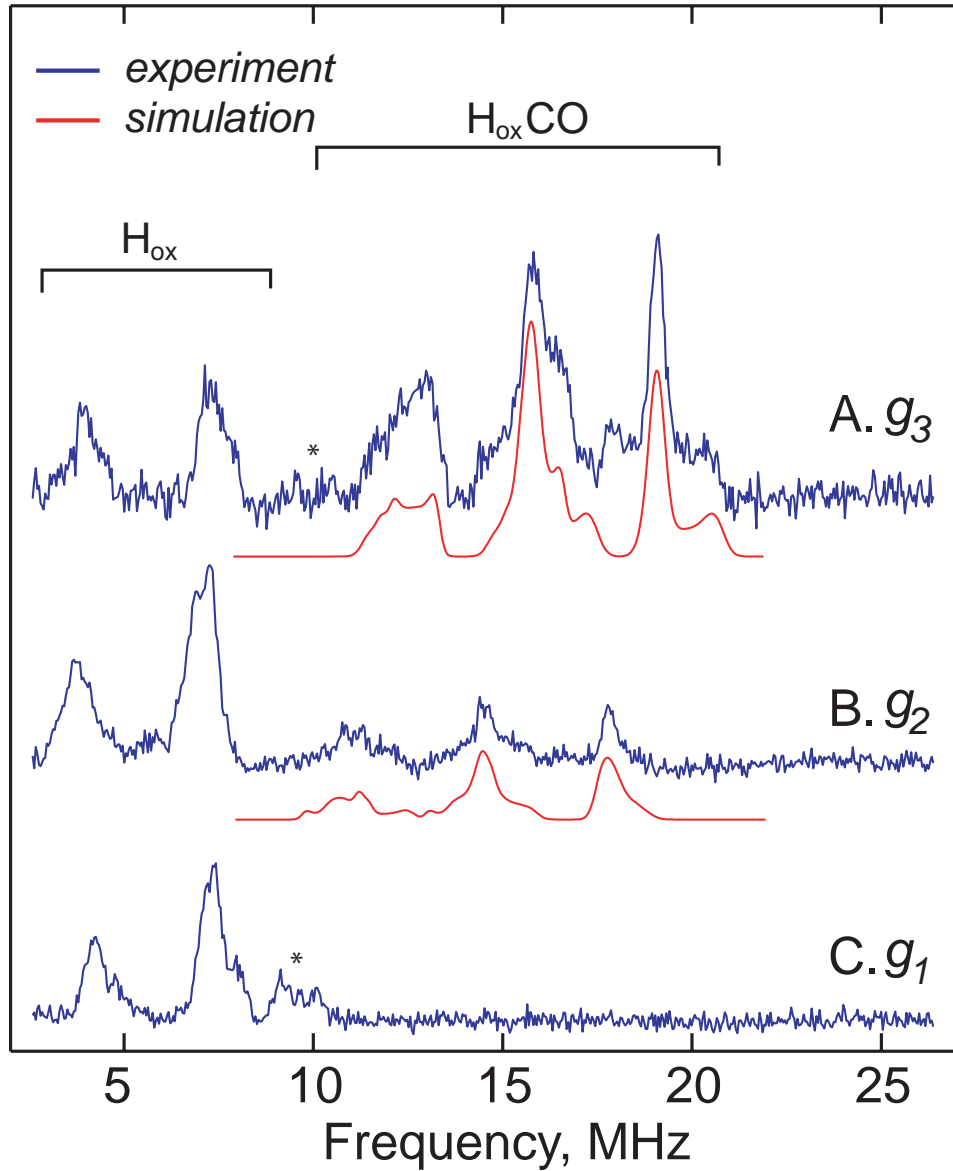


**Figure 7.4:** Q-band Davies ENDOR spectra of  $^{57}\text{Fe}$ -enriched [FeFe] hydrogenase in the  $H_{ox}$  state, recorded at 15 K at different field positions. All spectra were taken using  $t_{rf} = 40\mu\text{s}$  (optimum for high frequency region), MW frequency, 33.857GHz. **A:**  $B_0 = 1207\text{mT}(g_3)$ ; **B:**  $B_0 = 1186\text{mT}(g_2)$ ; **C:**  $B_0 = 1153\text{mT}(g_1)$ . Red lines represent simulation of the Davies ENDOR spectra of the  $H_{ox}$ -CO state using parameters  $A_{Fe}^{1,2,3,4}$  from table 6.1. Asterisks (\*) in the spectra indicates artifacts due to the experimental setup.

high frequency part (10-20 MHz), the spectra are similar to those presented in figure 6.4 (the  $^{57}\text{Fe}$  -enriched  $\text{H}_{\text{ox}}$ -CO state). These peaks have maximum intensity at a magnetic field around  $g = 2.00$ , which corresponds to the maximum of the EPR absorption line for the  $\text{H}_{\text{ox}}$ -CO state (see figure 7.2) and vanishes with decreasing magnetic field. At  $g = 2.10$  these peaks could not be detected anymore, while the low frequency peaks in an ENDOR spectrum are still present. Although it cannot be excluded that the  $\text{H}_{\text{ox}}$  state shows  $^{57}\text{Fe}$  ENDOR signals in the high frequency range it seems unlikely since all observed features could be explained using the  $\text{H}_{\text{ox}}$ -CO data. In figure 7.4 these spectra are shown together with simulation of the high frequency part, calculated using the parameters of the spin Hamiltonian for the  $^{57}\text{Fe}$  -enriched  $\text{H}_{\text{ox}}$ -CO state from table 6.1. This analysis confirms that the contaminating signal is due to the  $\text{H}_{\text{ox}}$ -CO species and thus supports the "cannibalization" effect discussed earlier [38]. The low frequency region (1-10MHz) of the ENDOR spectra of the  $^{57}\text{Fe}$  enriched  $\text{H}_{\text{ox}}$  state shows two peaks with a complex lineshape, separated by the double Larmor frequency of the  $^{57}\text{Fe}$  nuclei, indicative of the strong HF coupling case ( $2\nu_L < |A|$ ). Since these peaks are not present in the spectra of the  $\text{H}_{\text{ox}}$ -CO state, they have been assigned to the  $\text{H}_{\text{ox}}$  state. Measurements at higher RF frequency reveal no other signals accept from  $^1\text{H}$  nuclei in the frequency range 40-60MHz. In order to gain resolution and quality of the ENDOR spectra additional measurements at Q- and X-band, specifically focused on these peaks, have been performed. In figure 7.5 the resulting spectra are shown.

Due to the rather short electron spin  $T_1$  relaxation time the optimum length of the RF  $\pi$  pulse (determined as  $150 \mu\text{s}$  at 7 MHz) did not give a satisfactory signal-to-noise ratio (S/N). As a compromise a pulse length of 100-110  $\mu\text{s}$  (110-120  $\mu\text{s}$  delay between inversion and detection) was chosen. For the X-band ENDOR measurements an RF  $\pi$  pulse of approximately 10  $\mu\text{s}$  was required. The low frequency peaks represent an  $^{57}\text{Fe}$  HF coupling of roughly 11 MHz. The lineshape of these peaks is however quite complicated and a detailed analysis indicates that these spectra consist of at-least two pairs of doublets. Since the intensity of the two doublets differs about a factor of 2, it was assumed that they are due to two sets of  $^{57}\text{Fe}$  HF couplings in the occupation ratio 1:2.

Calculated spectra, presented in figure 7.5, have been obtained using two sets of parameters  $A_{Fe}^{1,2}$  (see table 7.1). Both HF couplings have a small anisotropy. The X-band ENDOR spectra reveal only one moderately broad bell-shaped peak at 11 MHz almost without any structure. Using the same Q-band ENDOR simulation parameters for simulation of the X-band spectra show a more complex lineshape than experimentally

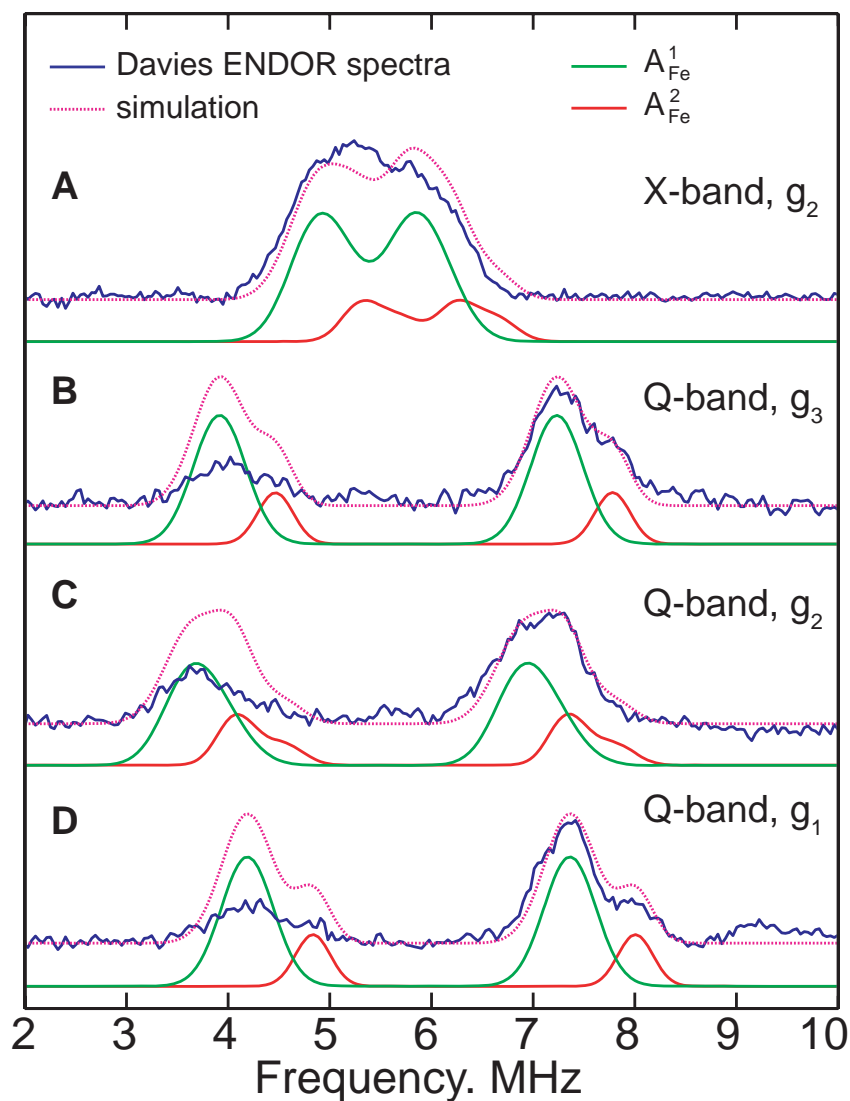


**Figure 7.5:** The X-band (**A**) and Q-band (**B,C,D**) Davies ENDOR spectra of  $^{57}\text{Fe}$ -enriched [FeFe] hydrogenase in the  $H_{ox}$  state, recorded at temperature of 15K. **A.**  $t_{rf} = 10\mu s$ ; the magnetic field was set to 340 mT ( $g_2 = 2.04$ ), microwave frequency, 9.74 GHz. **B.**  $B_0 = 1153mT(g_1)$ ;  $t_{rf} = 110ms$ ; **C.**  $B_0 = 1186mT(g_2)$ ;  $t_{rf} = 110\mu s$ ; **D.**  $B_0 = 1207mT(g_3)$ ,  $t_{RF} = 100ms$ ; **B,C,D:** microwave frequency, 33.86 GHz. All Q-band ENDOR spectra were obtained with random acquisition. The blue curves represent experimental data. The red curves are the simulations of the ENDOR spectra using parameters  $A_{Fe}^1$  and  $A_{Fe}^2$  presented in Table 7.1. The components of the simulations are indicated with green ( $A_{Fe}^1$ ) and red ( $A_{Fe}^2$ ) lines.

**Table 7.1:** HF interaction parameters of the  $^{57}\text{Fe}$  nuclei, found for the H-cluster in the  $\text{H}_{\text{ox}}$  state.

	$A_{xx}$ (MHz)	$A_{yy}$ (MHz)	$A_{zz}$ (MHz)	$A_{iso}$ (MHz)	$[\varphi, \theta, \psi]$ (deg)
$A_{Fe}^1$	$11.2 \pm 0.2$	$10.4 \pm 0.2$	$11.6 \pm 0.2$	$11.6 \pm 0.2$	$[0, 0, 0] \pm 30$
$A_{Fe}^2$	$12.3 \pm 0.3$	$11.4 \pm 0.3$	$12.9 \pm 0.3$	$12.4 \pm 0.2$	$[0, 0, 0] \pm 30$

observed (see figure 7.5). This probably indicates, that there are more than two non-equivalent HF couplings, which result in a more averaged lineshape of the X-band ENDOR spectrum. However, both X- and Q-band ENDOR spectra have not enough spectral resolution to disentangle possible subspectra. Therefore, despite of the very good fit of the simulation at Q-band, the estimated uncertainty range is relatively high (see table 7.1). In order to understand the electronic structure of the H-cluster in the  $\text{H}_{\text{ox}}$  state it is important to clarify the number of  $^{57}\text{Fe}$  nuclei taking part in the  $^{57}\text{Fe}$  ENDOR spectra. Due to several reasons (e.g. difference in the nuclear relaxation rates) the intensities of ENDOR lines, belonging to different nuclei may differ from each other. This makes the analysis of the number of interacting  $^{57}\text{Fe}$  nuclei directly from the ENDOR intensity quite unreliable. Therefore, another method has to be used to resolve this question as discussed below.

### 7.2.2 Lineshape analysis of CW EPR spectra

Another way to detect the presence of HF couplings is the comparison of the CW EPR spectra of samples with and without enrichment by a certain isotope. The precision of this method of determination can vary from very accurate (in a case of very strong HF couplings) to completely unreliable. However, since the magnitude of the  $^{57}\text{Fe}$  HF coupling constants is already known from the ENDOR study, this method can be used to determine the number of coupled  $^{57}\text{Fe}$  nuclear spins with high precision.

Because the rhombic EPR spectrum of the  $\text{H}_{\text{ox}}$  state shows partial overlap with contaminating signals of the  $\text{H}_{\text{ox}}$  -CO state and the dipolar-coupled reduced [4Fe4S] clusters (see figure 7.2), the lineshape analysis of the complete CW EPR spectrum is complicated. However a precise determination of the HF coupling constants by this method is not important. Thus, it is sufficient to merely analyze the 'low-field' component of the rhombic spectrum which is free from overlap with other species. For this purpose, the spectrum of the  $^{57}\text{Fe}$ -enriched H-cluster in the  $\text{H}_{\text{ox}}$  state was measured using the same experimental conditions as the non-enriched sample. Then the spectrum of the non-

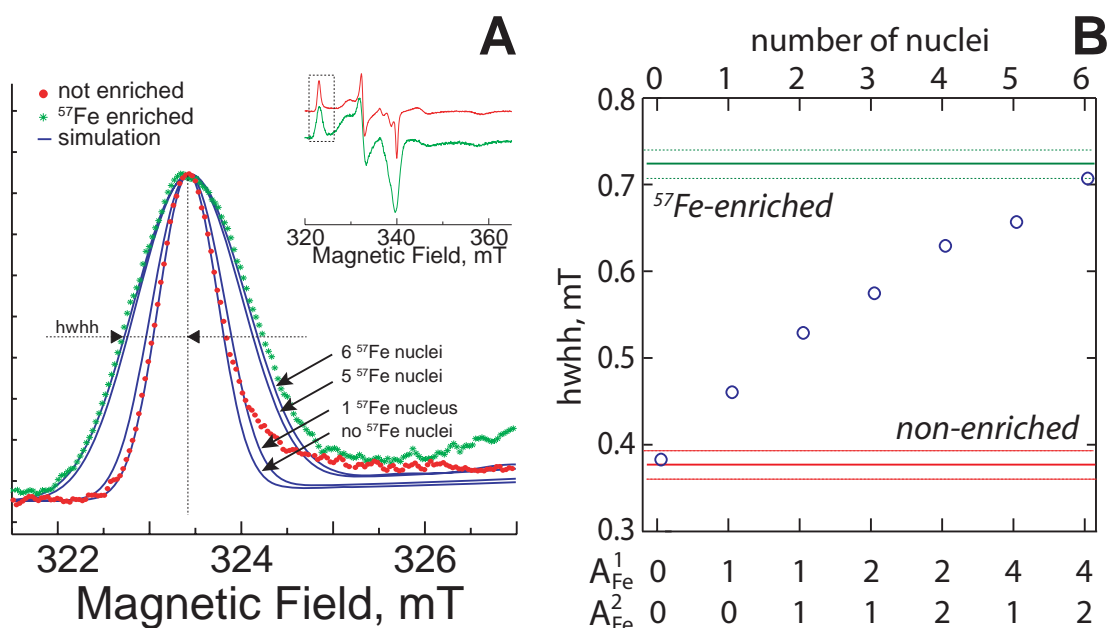


**Figure 7.6:** Analysis of the line-broadening of CW EPR spectra of the  $H_{ox}$  state due to  $^{57}\text{Fe}$  HF interactions. Both experimental spectra were taken under the same conditions: temperature, 50 K; microwave power 20 mW; microwave frequency, 9.5968 GHz; modulation amplitude, 0.3 mT with 100 kHz modulation frequency; time constant, 40.96 ms; conversion time 81.92 ms. **A.** Comparison of the "g<sub>1</sub>" component of the experimental spectra (green and red) with theoretical spectra (blue), calculated with different number of  $^{57}\text{Fe}$  nuclei. **B.** Dependence of the hwhh (half width on half height) parameter of the 'z'-component of the EPR spectrum on the number of coupled  $^{57}\text{Fe}$  nuclei. Dashed lines represent the uncertainty range in the hwhh determination. For the simulation the parameters  $A_{\text{Fe}}^{1,2}$  from table 7.1 have been used.

enriched H-cluster in the  $H_{ox}$  state was simulated.

Simulation has been performed using 'pepcalc' routine from the EasySpin package [101] for MatLab<sup>TM</sup>. Following basic input parameters for the lineshape simulation has been obtained:

```

g-value (Sys.g):                [2.10, 2.040, 1.999];
isotropic magnetic-field
domain linewidth (Sys.lw):       0.1 mT;
g strain (Sys.gStrain):         [0.0049, 0.0043, 0.003];
Number of orientations on
quarter of meridian (Opt.nKnots): 40;
Basic line shape (Opt.LineShape): 'Gaussian';

```

This parameters were then used as a base parameters for the simulation of the EPR spectrum of the  $^{57}\text{Fe}$ -enriched sample. The calculations of the line broadening were performed using  $^{57}\text{Fe}$  HF coupling constants obtained from the Q-band ENDOR experiments. In this simulation only the number of interacting  $^{57}\text{Fe}$  nuclei was varying while all other parameters were fixed.

Figure 7.6 shows the comparison of the  $g_1$  components of the CW EPR spectra of the native and the  $^{57}\text{Fe}$ -enriched  $\text{H}_{\text{ox}}$  state of the H-cluster. The same plot includes a simulation of the EPR lineshape accounting different numbers of nuclei.

As it is shown in figure 7.6, the best fit of the CW EPR experimental spectrum of the  $^{57}\text{Fe}$  enriched H-cluster in the  $\text{H}_{\text{ox}}$  state requires the inclusion of 6 nuclei: four nuclei with HF coupling constants  $A_{\text{Fe}}^1$  (about 11 MHz) and two HF couplings  $A_{\text{Fe}}^2$  (approximately 12 MHz). The width of the EPR spectrum calculated using one nuclei with  $A_{\text{Fe}}^2$  and four with  $A_{\text{Fe}}^1$  is clearly smaller than experimental spectrum.

The fact that six rather similar HF couplings have been found indicates the profound distribution of the unpaired spin density in the bi-nuclear subcluster.

### 7.2.3 Assignment

In the interpretation of the ENDOR spectra (figure 7.5), the doublet, corresponding to the larger coupling  $A_{\text{Fe}}^2$ , has approximately half the amplitude of the one corresponding to the smaller HF coupling ( $A_{\text{Fe}}^1$ ). According to the coupling model introduced in chapter 1, lowering the exchange interaction between  $[\text{4Fe4S}]_{\text{H}}$  and  $[\text{2Fe}]_{\text{H}}$  will lead to smaller effective HF couplings of the iron nuclei in the  $[\text{4Fe4S}]_{\text{H}}$  subcluster. As it follows from equation (2.1), in this case, the difference between the HF couplings of the different  $[\text{Fe(II)-Fe(III)}]$  pairs in the 'cubane' should decrease with decreasing exchange coupling ( $J$ ). Therefore, it is expected to find four almost identical  $^{57}\text{Fe}$  HF couplings for the irons in the  $[\text{4Fe4S}]_{\text{H}}$  subcluster. From these arguments it follows that the coupling  $A_{\text{Fe}}^1$  should originate from the four iron nuclei in the 'cubane', while the two larger HF couplings correspond to iron nuclei in the binuclear subcluster ( $[\text{2Fe}]_{\text{H}}$ ). The  $^{57}\text{Fe}$  HF couplings of the iron nuclei in  $[\text{2Fe}]_{\text{H}}$  are not resolve and are thus likely to be more or less the same.

The fact that both iron nuclei of the binuclear subcluster reveal the same HF couplings indicates a substantial distribution of the unpaired spin over this subcluster. This conclusion can also be proved via investigation of the electron spin distribution over ligands of the irons (CO and CN).

### 7.3 Investigation of the $^{14}N$ nuclear spin couplings

A second source for information of the electronic structure in the  $H_{ox}$  state is the hyperfine and quadrupole couplings of  $^{14}N$ . As it is shown in figure 7.1 there are at least two nitrogen atoms in the system, i.e. the cyanide ligands of the iron nuclei. The main aim of this study is to resolve the hyperfine and quadrupole interaction of  $^{14}N$  nuclei and therefore gain additional information about the distribution of unpaired spin density over  $[2Fe]_H$  subcluster.

X-band ESEEM experiments are usually very sensitive to  $^{14}N$  HF interactions. Therefore, further investigation was done using hyperfine sublevel correlation spectroscopy (HYSCORE). Figures 7.7, 7.8 and 7.9 show X-band HYSCORE spectra measured for different positions of the magnetic field together with their interpretation. Since the HYSCORE spectra are very sensitive to the value of  $\tau$  (so-called blind-spot behavior), several measurements were performed with different  $\tau$  for each position of magnetic field. It was found, that for  $\tau = 180ns$  spectra were obtained with maximum information. In all spectra, steps of  $t_1$  and  $t_2$  were chosen as long as possible, giving best resolution in the low frequency region, but still avoiding folding of the  $^1H$  signals <sup>1</sup>.

From earlier investigations of various systems CN coordinated to iron complexes in the low-spin state, like  $Fe(CN)_6^{3-}$  [98], it is expected that the  $^{14}N$  HF interaction is very anisotropic and the quadrupole interaction is rhombic. Moreover, in most of the cases the HF and quadrupole tensor principal axes are not collinear with the g-tensor axes, which makes the analysis more complicated. Therefore a direct extraction of the spin-Hamiltonian parameters from the position of the ridges in the spectra is not possible in the case of frozen-solution samples. Thus a complete simulation of the HYSCORE spectra has been performed to obtain parameters of the  $^{14}N$  HF and quadrupole interaction.

The experimental spectra, taken at the "single-crystal" positions ( $g_1$  and  $g_3$ ), show broad ridges. This indicates, that the  $^{14}N$  HF couplings are quite anisotropic and are not collinear with the g-tensor. As it follows from the complexity of the HYSCORE spectrum for  $B_0 \parallel g_1$ , there are certainly more than one  $^{14}N$  nucleus that give rise to the ESE modulations. A detailed investigation of the X-band spectra reveals the presence of two  $^{14}N$  nuclei substantially different by both hyperfine and quadrupole couplings. Table 7.2 shows the spin Hamiltonian parameters, used for these simulations. The simulated

<sup>1</sup>If steps for  $t_1$  and  $t_2$  are bigger than the half period of the modulations owing to a  $^1H$  nuclear spin, than the Fourier transformation of the obtained time-domain data would reveal peaks with frequency lower than the true frequency of the modulations, i.e. folding of the signal.

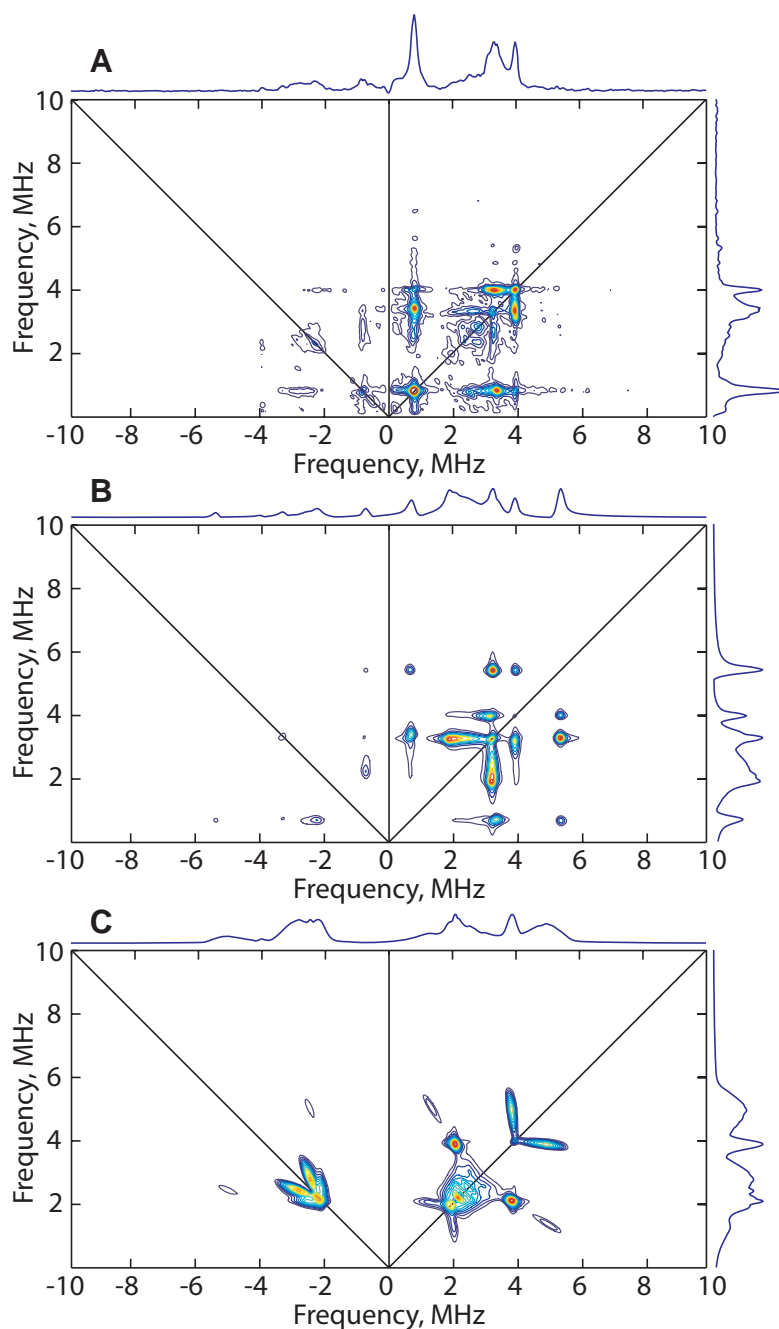


**Figure 7.7:** X-band HYSORE spectrum (A) of the non-enriched enzyme in the  $\text{H}_{\text{ox}}$  state recorded at  $g_1$  with its simulation (B, C). Experimental conditions:  $T=20\text{K}$ ; MW freq,  $9.548\text{GHz}$ ;  $t_{\pi/2} = 12\text{ns}$ ;  $t_{\pi} = 16\text{ns}$ ;  $\tau = 180\text{ns}$ ,  $B_0 = 324.8\text{mT}(g_1)$ . Theoretical spectra were calculated using parameters from table 7.2 B:  $A_N^1$ ,  $Q_N^1$  and C:  $A_N^2$  and  $Q_N^2$ .

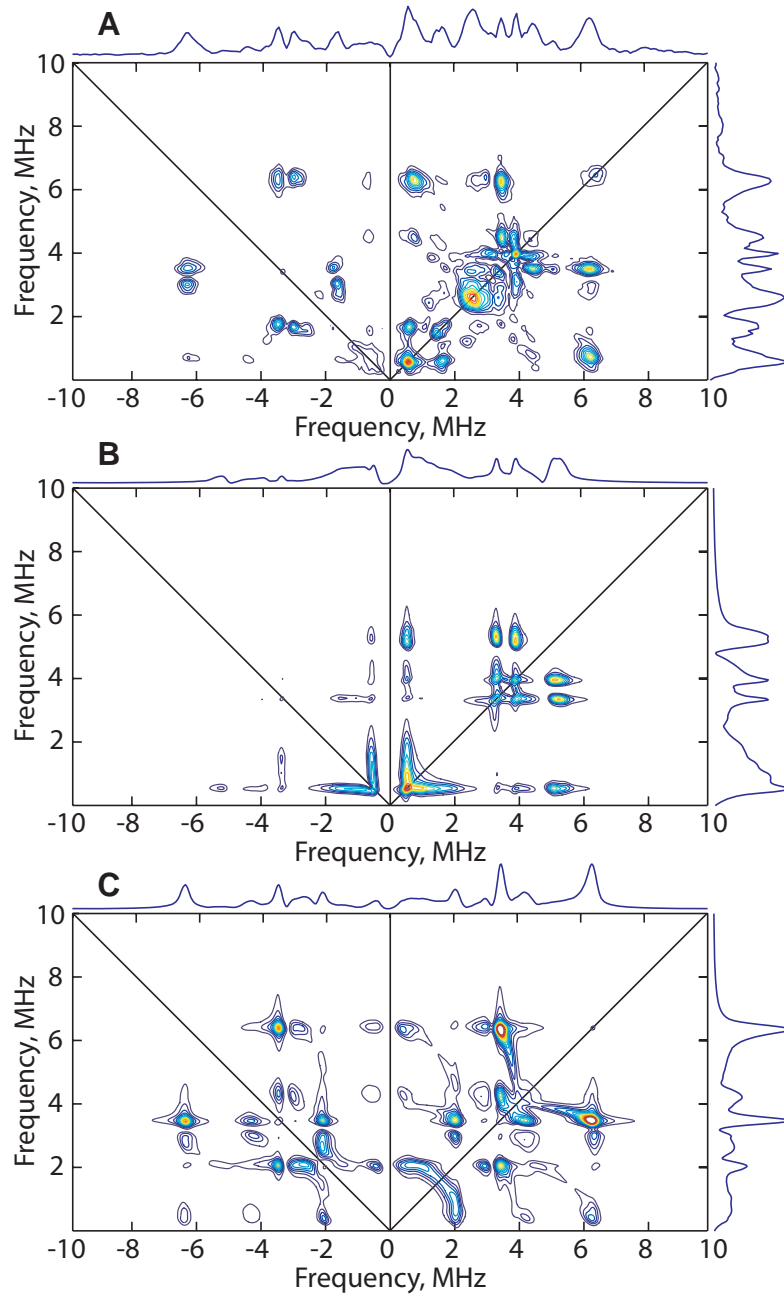


**Figure 7.8:** X-band HSCORE spectrum (A) of the non-enriched enzyme in the  $H_{ox}$  state recorded at  $g_2$  with its simulation (B, C). Experimental conditions:  $T=20K$ ; MW freq,  $9.548GHz$ ;  $t_{\pi/2} = 12ns$ ;  $t_{\pi} = 16ns$ ;  $\tau = 180ns$ ,  $B_0 = 334.4mT(g_2)$ . Theoretical spectra were calculated using parameters from table 7.2 B:  $A_N^1$ ,  $Q_N^1$  and C:  $A_N^2$  and  $Q_N^2$ .

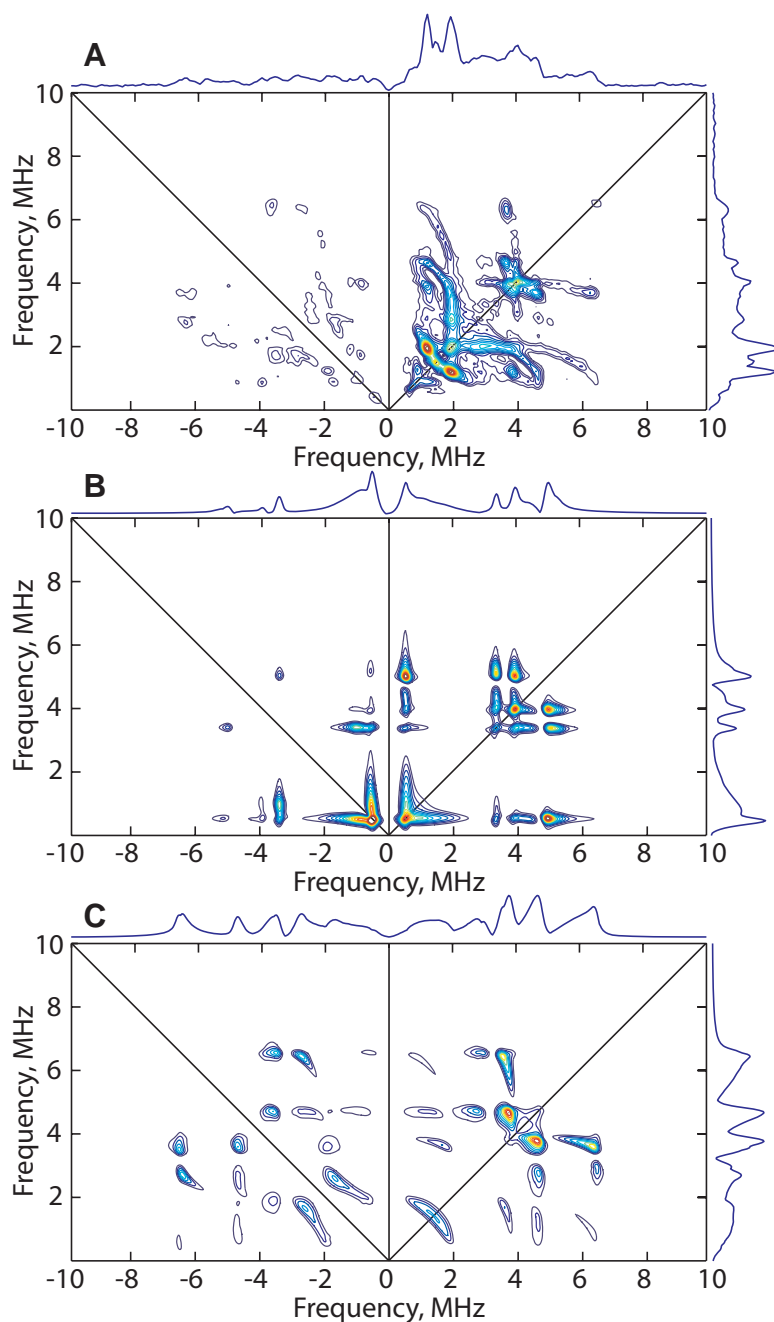


**Figure 7.9:** X-band HYSORE spectrum (A) of the non-enriched enzyme in the  $\text{H}_{\text{ox}}$  state recorded at  $g_3$  with its simulation (B, C). Experimental conditions:  $T=20\text{K}$ ; MW freq,  $9.548\text{GHz}$ ;  $t_{\pi/2} = 12\text{ns}$ ;  $t_{\pi} = 16\text{ns}$ ;  $\tau = 180\text{ns}$ ,  $B_0 = 340\text{mT}(g_3)$ . Theoretical spectra were calculated using parameters from table 7.2 **B:**  $A_N^1$ ,  $Q_N^1$  and **C:**  $A_N^2$  and  $Q_N^2$ .

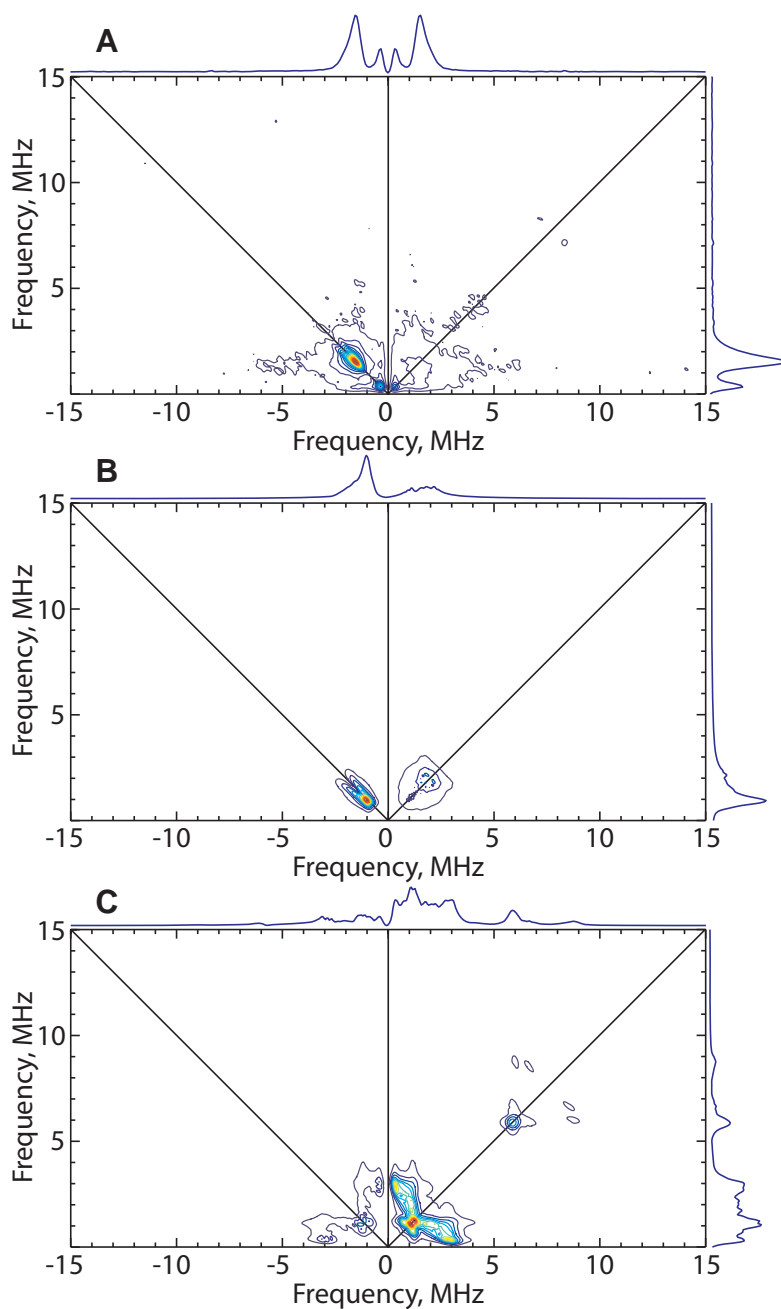


**Figure 7.10:** Q-band HYSORE spectrum (A) of the non-enriched enzyme in the  $H_{ox}$  state recorded at  $g_1$  with its simulation (B, C). Experimental conditions: Temperature, 20K; MW freq, 33.865GHz;  $t_{\pi/2} = 32ns$ ;  $t_{\pi} = 64ns$ ;  $\tau = 300ns$ ,  $B_0 = 1154mT(g_1)$ . Theoretical spectra were calculated using parameters from table 7.2 **B**:  $A_N^1$ ,  $Q_N^1$  and **C**:  $A_N^2$  and  $Q_N^2$ .

### 7.3 Investigation of the $^{14}\text{N}$ nuclear spin couplings

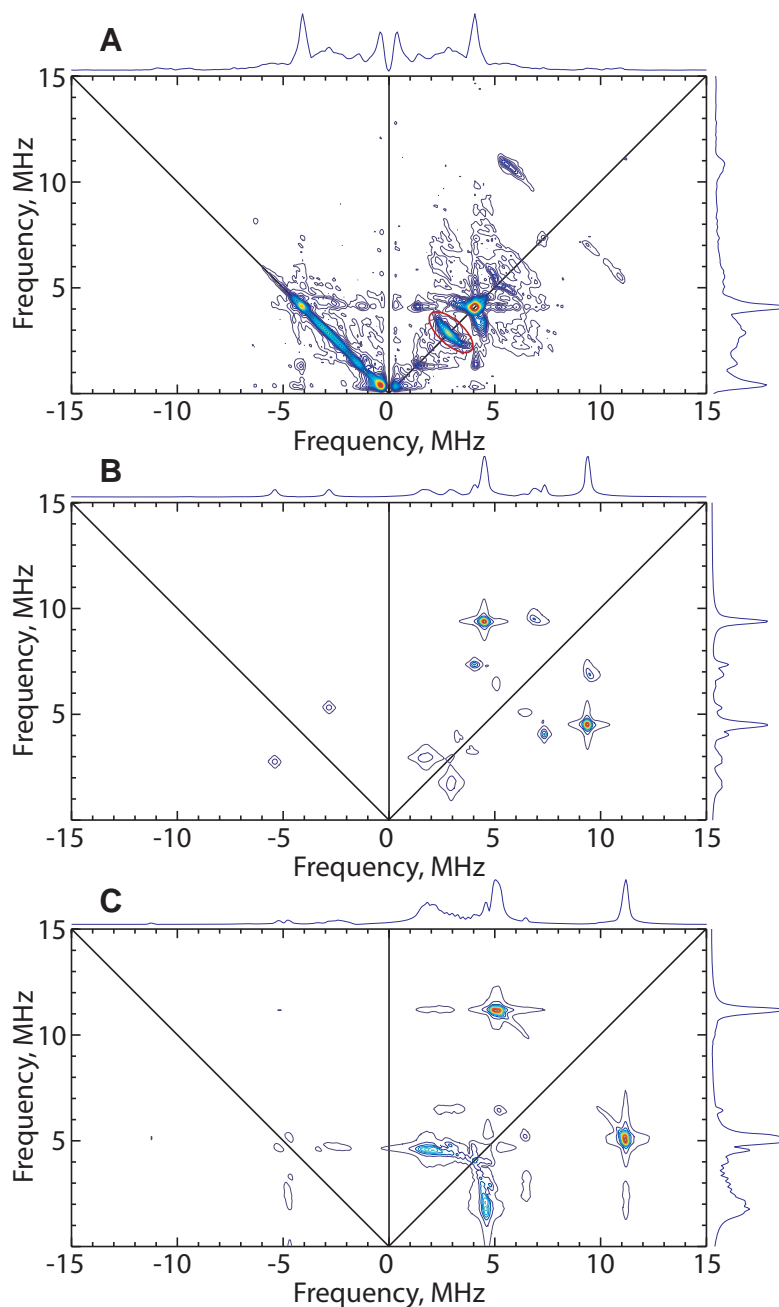


**Figure 7.11:** Q-band HYSORE spectrum (A) of the non-enriched enzyme in  $\text{H}_{\text{ox}}$  state recorded at  $g_2$  with its interpretation (B, C). Experimental conditions: Temperature, 20K; MW freq, 33.865GHz;  $t_{\pi/2} = 32\text{ns}$ ;  $t_{\pi} = 64\text{ns}$ ;  $\tau = 260\text{ns}$ ,  $B_0 = 1185\text{mT}(g_2)$ . Theoretical spectra were calculated using parameters from table 7.2 B:  $A_N^1$ ,  $Q_N^1$  and C:  $A_N^2$  and  $Q_N^2$ . The signal marked by the red circle can not be interpreted using these parameters indicating this originates from a third  $^{14}\text{N}$  nuclei (DTN).

**Table 7.2:** Parameters of the spin Hamiltonian, related to the  $^{14}\text{N}$  nuclei in the H-cluster in  $H_{ox}$  state. All constants are in MHz units and angles in degree.

<i>Hyperfine interaction</i>							
	$A_{xx}$	$A_{yy}$	$A_{zz}$	$ A_{iso} $	$\varphi$	$\theta$	$\psi$
$A_N^1$	$1.0 \pm 0.3$	$1.7 \pm 0.5$	$1.4 \pm 0.3$	$1.36 \pm 0.4$	$-40 \pm 20$	$0 \pm 20$	$0 \pm 10$
$A_N^2$	$3.8 \pm 0.2$	$3.5 \pm 0.2$	$-0.2 \pm 0.2$	$2.36 \pm 0.2$	$0 \pm 10$	$22 \pm 10$	$0 \pm 10$
<i>Quadrupole interaction</i>							
	K	$\eta$	$\varphi$	$\theta$	$\psi$		
$Q_N^1$	$1.21 \pm 0.01$	$-0.21 \pm 0.05$	$40 \pm 30$	$-10 \pm 20$	$0 \pm 10$		
$Q_N^2$	$0.96 \pm 0.01$	$-0.3 \pm 0.05$	$0 \pm 20$	$5 \pm 10$	$0 \pm 10$		

spectra **B**, presented in figures 7.7, 7.8 7.9 are generated using parameters  $A_N^1, Q_N^1$  from table 7.2, while spectra **C** are calculated using parameters  $A_N^2, Q_N^2$ . The theoretical spectra fit the experimental data very well. However, for some of the parameters, the uncertainty range is rather large.

In order to confine the parameter space further, measurements at Q-band frequency were performed. The Q-band HYSCORE spectra reveal rather simple spectra as shown in figures 7.10 and 7.11. The simulations, calculated with parameters from the X-band HYSCORE spectra, fit experimental data quite well. Moreover, due to a better orientation selectivity of the Q-band spectra, the precision is significantly increased. In the experimental Q-band HYSCORE spectra some additional ridges were observed which are not simulated using parameters  $A_N^1, Q_N^1$  and  $A_N^2, Q_N^2$  (table 7.2) These ridges are located along the diagonal of the (++) quadrant close to the Larmor frequency of the  $^{14}\text{N}$  nucleus (3.65 MHz at 1185 mT). This indicates that the respective HF interaction is rather weak and quadrupole coupling is also relatively small (estimated to be around 0.35 MHz). The shape of these ridges also indicates an anisotropic character of the HF coupling. Therefore it is suggested, that there may be a third  $^{14}\text{N}$  nucleus present. However, due to the limited resolution of these ridges in the HYSCORE spectra, further (ENDOR) studies are needed at higher magnetic fields to extract the nuclear spin interaction parameters. The only possible origin of this signal is the di-thiol ligand<sup>2</sup>, which had been recently suggested to contain nitrogen [35, 42, 43] (DTN). Therefore this experimental observation can be considered as a first evidence of nitrogen containing di-thiol ligand in the bi-nuclear

<sup>2</sup>Though there are nitrogens in the cysteins (coordinating  $[4\text{Fe}4\text{S}]_{\text{H}}$  subcluster), it seem quite unlikely to observe them, because of their remoteness

subcluster.

## 7.4 Summary and Discussion

### 7.4.1 Electronic structure

For the  $H_{ox}$  state six similar  $^{57}\text{Fe}$  HF couplings were found (see table 7.1). This leads to the conclusion, that the unpaired spin in the bi-nuclear cluster is delocalized. This conclusion is also supported by the study of the  $^{14}\text{N}$  HF interactions (see table 7.2). According to this study, two moderately strong  $^{14}\text{N}$  HF couplings with constants of  $A_{iso}=1.36$  MHz and 2.36 MHz were observed and assigned to the CN ligands of the  $\text{Fe}_d$  and  $\text{Fe}_p$  iron atoms. The results presented here seem to indicate, that for the  $H_{ox}$  state the unpaired spin is distributed almost equally over the two irons in the bi-nuclear cluster while in the  $H_{ox}\text{-CO}$  state, the unpaired spin is rather shifted towards the proximal iron (see chapter 6). This conclusion disagrees with recent theoretical investigations of the electronic structure on models of the H-cluster in the  $H_{ox}$  and the  $H_{ox}\text{-CO}$  states by Fiedler et. al [97]. These authors suggest that in the  $H_{ox}$  state most of the unpaired spin density is localized at the distal iron, while in the  $H_{ox}\text{-CO}$  state it is more distributed over the bi-nuclear subcluster. However it should be noted, that the authors modeled only the bi-nuclear subcluster. The discrepancy with experimental results indicates, that in order to create a correct theoretical electronic model of the H cluster one should calculate the complete system including the  $[4\text{Fe}4\text{S}]_H$  subcluster.

In the same article [97], the authors also present results on the geometry optimization of the whole 6Fe H-cluster in the  $H_{ox}$  and the  $H_{ox}\text{-CO}$  states. This reveals that placing an additional CO ligand at the distal iron leads to an increase of the  $\text{Fe}_p\text{-Fe}_d$  distances from 2.56 Å for  $H_{ox}$  to 2.71 Å for  $H_{ox}\text{-CO}$ , as well as a shift of the bridging CO ligand towards the proximal iron. Therefore it can be concluded that adding a CO ligand weakens the coupling between the two irons leading to a stronger localization of the spin density, in this case towards the proximal iron. This, in turn, increases the exchange interaction between the unpaired spin in the bi-nuclear subcluster with the 'cubane' as is observed experimentally.

### 7.4.2 Comparison with earlier spectroscopic studies

The investigation of the  $^{57}\text{Fe}$  HF couplings of the H-cluster reveal controversies with previous results obtained from the investigation of the H-cluster from *D.vulgaris* (Hildenborough) by Mössbauer spectroscopy [60]. While the Mössbauer studies reveal

**Table 7.3:** Comparison of g-values of the  $H_{ox}$  and the  $H_{ox}$ -CO states of various enzymes

	$H_{ox}$			$H_{ox}$ -CO		
	$g_1$	$g_2$	$g_3$	$g_1$	$g_2$	$g_3$
<i>D.desulfuricans</i> (this study)	2.100	2.040	2.000	2.065	2.007	2.001
<i>C.pasteurinaum</i> , hydrogenase I [51, 102]	2.10	2.04	2.00	2.07	2.01	2.01
<i>C.pasteurinaum</i> , hydrogenase II [49]	2.078	2.027	1.999	2.032	2.017	1.997

two sets of  $^{57}\text{Fe}$  HF couplings, which differ by a factor of 2 (8.5 MHz and 16.4 MHz), the investigation presented here reveals two quite similar sets of HF couplings (isotropic values of 11.1 and 12.4 MHz). The small couplings in the Mössbauer investigation were attributed to the  $[4\text{Fe}4\text{S}]_H$  subcluster, while the HF coupling constant of 16.4 MHz was assigned to the one of the irons in the bi-nuclear cluster. The other iron nucleus in the  $[2\text{Fe}]_H$  subcluster is suggested to have no HF interaction. However, it should be noted that the Mössbauer spectra are difficult to analyze due to the many parameters involved as well as the large number of overlapping signals (overall 14 iron nuclei, *D. desulfuricans*). Moreover, due to the usage of a electrochemical method of obtaining the different states there is a mixture of two states ( $H_{ox}$  and  $H_{red}$ ) present in the sample at the potential -310mV, used for study of the  $H_{ox}$  state. Therefore, despite the advanced analysis of the spectra, performed by the authors, there remains the possibility of the existence of several different sets of parameters of the spin Hamiltonian, which produce similar Mössbauer spectra. On the other hand, earlier ENDOR studies of the H-cluster in  $[\text{FeFe}]$  hydrogenase type II, from *C. pasteurianum* by Telser et al [49], did not suffer from these problems and the obtained values of the HF couplings should be regarded as reliable. It therefore cannot be excluded that the electronic structure of the H-cluster in *C.p.II* differs from that in *D. desulfuricans*. This idea is also supported by fact that from these two organisms characteristic g-values of the EPR spectra of the H-cluster are different (see table 7.3).

Nevertheless, in general, the finding of a lower  $[2\text{Fe}]_H$ - $[4\text{Fe}4\text{S}]_H$  exchange interaction in comparison with the  $H_{ox}$ -CO state is confirmed.



---

# 8

## Photo-dissociation of the $H_{ox}$ -CO state

---

Investigation of the relation between structural properties of the active site of the [FeFe] hydrogenase and the reactions, going on during the catalytic cycle is very important for understanding the functions of the H-cluster. The dissociation of the CO ligands by light excitation provides a convenient means for studying the naturally occurring ligand exchange processes. The CO bonding geometry is likely to change during the catalytic cycle [12, 38, 103]. It is also known that several CO ligands of the bi-nuclear subcluster are very sensitive to the illumination by light (see Introduction). In this chapter the study of photolytic processes in the H-cluster in the  $H_{ox}$ -CO state is presented. The main goal of this study is to understand, how the properties of the H-cluster change with changing the CO bonding geometry. Another problem which will be addressed is, the investigation of the kinetics of the photo-dissociation processes and its relation to the physical properties of the H-cluster.

### 8.1 Light-induced states

The EPR spectrum of the oxidized CO-inhibited state ( $H_{ox}$ -CO) of the H-cluster at 40K is shown in figure 6.2. This spectrum characterized by the principal  $g$ -values  $g_1 = 2.065$ ,  $g_2 = 2.007$ ,  $g_3 = 2.001$  as resolved in the Q-band EPR study, presented in chapter 6. In figure 8.1 a plot of the changing EPR signal during illumination at 40K is presented. As follows from this figure, the signal from the  $H_{ox}$ -CO state is decreasing under illumination, while some other signals appear. Figure 8.2 represents a typical spectrum, appearing after illumination at 40 K for 2 hours. Two light-induced species were identified from the EPR spectra. One of the additional species ( $L_1$ ) has an EPR spectrum, characterized by principal  $g$ -values, similar to the well known rhombic signal of the  $H_{ox}$  state (2.10, 2.04, 2.00). In earlier studies of the photo-dissociation of the  $H_{ox}$ -CO state by CW EPR [51, 104] and IR spectroscopy [38, 105] it was suggested, that this species is the  $H_{ox}$  state, characterized by the vacant external coordination site of the distal iron. EPR spectroscopy with its advanced techniques can provide a solid proof of this assignment by comparing

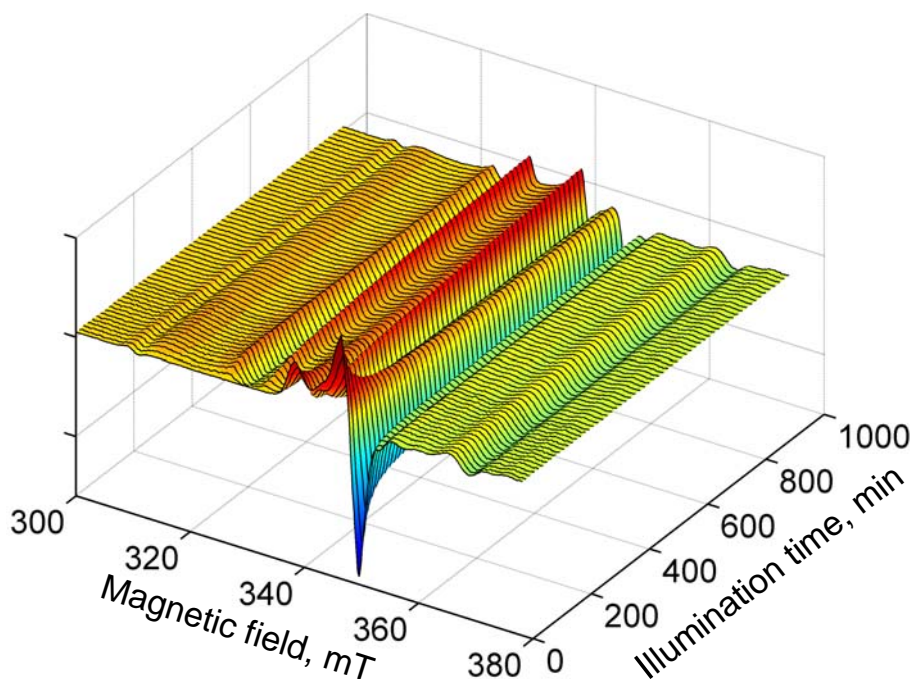


**Figure 8.1:** Typical changes in a CW EPR spectrum of the  $H_{ox}$ -CO state upon illumination. Experimental conditions: laser power, 8.5 mJ/pulse, wavelength, 531 nm; temperature, 40K; MW power, 20  $\mu$ W (40 dB att.); Mod. Amp, 5 G; Time const., 40 ms; MW freq., 9.780 GHz

the electronic structure of this state with that of the  $H_{ox}$ .

In order to clarify the origin of this light induced state, Q-band Davies ENDOR measurements on the  $^{57}\text{Fe}$ -enriched enzyme were performed at field positions, corresponding to the spectrum of the  $L_1$  state. The results are shown in figure 8.3. The  $^{57}\text{Fe}$  Davies ENDOR spectra of this state, recorded at two magnetic fields are identical to those, obtained from the  $H_{ox}$  state. These observations therefore, confirm the original assignment of the  $L_1$  state to the  $H_{ox}$  state of the H-cluster with vacant external site of distal iron ( $\text{Fe}_d$ ) (figure 8.4).

The additional rhombic EPR signal ( $L_2$ ) has principal  $g$ -values (2.226, 2.135, 2.051). According to an IR study on [FeFe] hydrogenase from *D. vulgaris* [104]<sup>1</sup> and a recent IR study on [FeFe] hydrogenase from *D. desulfuricans*. [38], this species has most probably lost the bridging CO ligand in the  $[2\text{Fe}]_H$  subunit, while the external CO ligand is still present (figure 8.4). However it was not clarified, if the bridging CO ligand is completely lost or if just one of the bonds is broken. The detailed characterization of the second

<sup>1</sup>It has a primary structure identical to *D. desulfuricans*.

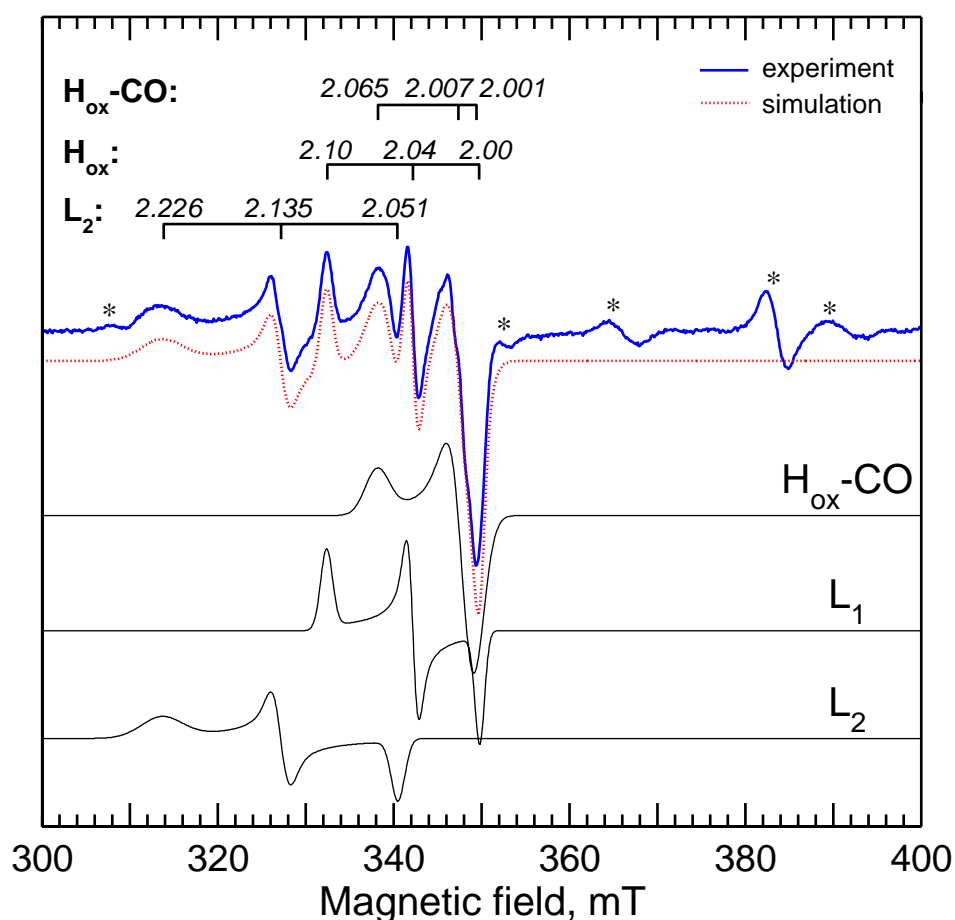


**Figure 8.2:** CW EPR spectrum typically resulting from illumination (2 hours) of the  $H_{ox}$ -CO state. Experimental conditions: laser power, 8.5 mJ/pulse, wavelength, 531 nm; temperature, 40K; MW power, 20  $\mu$ W (40 dB att.); Mod. Amp, 5 G; Time const., 40 ms; MW freq., 9.780 GHz. Asterisks (\*) indicate contaminating signals of the 'background' signals of the material of the dielectric resonator itself.

light induced state  $L_2$  is the subject of a separate study performed by CW and pulse EPR methods, presented below in chapter 9.

Illumination of the [FeFe] hydrogenase I from *Clostridium pasteurianum* at similar temperature described by Kowal et al. [51] also shows two light-induced states. Based on the characteristic g-values of the signal, one of these has been assigned to the  $H_{ox}$  state. The second light-induced EPR signal was also assigned to an oxidized H-cluster, lacking the bridging CO ligand but with an external CO ligand present. However this EPR signal

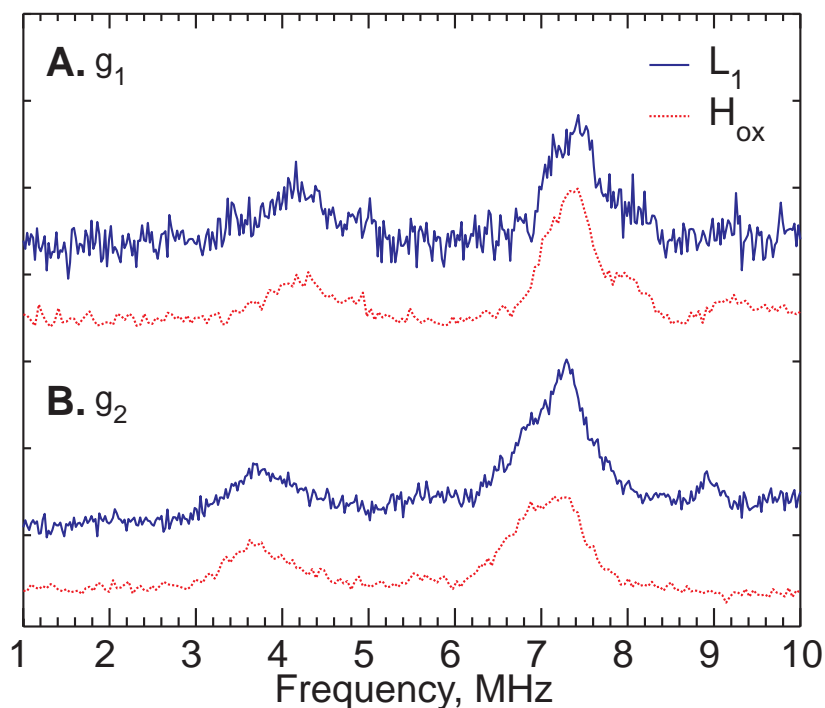


**Figure 8.3:** Comparison of the Q-band Davies ENDOR spectra of the  $L_1$  species with ENDOR spectra of the  $H_{ox}$  state (identical to the ones presented in figure 7.5). Experimental conditions: temperature, 8 K; MW freq., 33.90 GHz;  $t_{rf}=40\mu s$ ; magnetic field, **A** - 1155 mT; **B** - 1187.3 mT. OPO laser: power, 13mJ/pulse; wavelength, 531 nm, illumination has been stopped after 1 hour

has different  $g$ -values (2.26, 2.12, 1.89). Nevertheless, it is still possible, that the same state of the H-cluster (no bridging CO ligand) was obtained. As it has been suggested in chapter 7, there is a possibility that the active sites of the [FeFe] hydrogenases from *C. pasteurianum* and from *D. desulfuricans* have some difference in geometric and electronic structure, therefore the  $g$ -values can be different.

## 8.2 Photo-dissociation kinetics

### 8.2.1 Processing of the EPR data

In order to process the 2D EPR spectra (more than 100 traces for each photo-dissociation experiment) an automated fitting procedure was developed. As it is shown in figure 8.2, the EPR spectra of all species are partially overlapping and in addition to the "wanted" signals, there are also background signals, originating from the dielectric-ring resonator. To avoid possible mistakes in the automatic fitting due to these artifacts, a

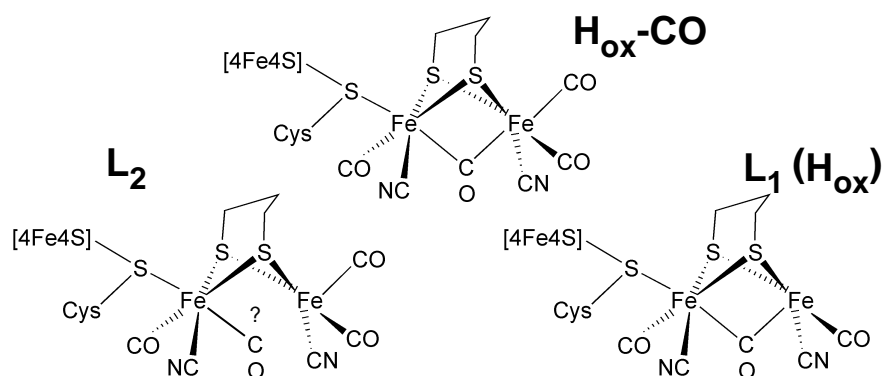


**Figure 8.4:** Suggested structures of the light induced states

special treatment of the experimental data has been performed.

The initial spectrum, i.e. the "base" spectrum, was subtracted from all subsequent spectra, recorded during illumination, thus retaining only spectra changing during illumination. The 'background' signals from the resonator as well as those from the reduced 'cubanes' are thus automatically suppressed. The X-band spectrometer used for this study was found to be stable enough to fully retain the experimental conditions during illumination<sup>2</sup>. This excludes the possibility that this subtraction can cause some artifacts, affecting the final result.

In the next step, all 'difference' EPR spectra were simulated using an automatic fitting routine, using the same set of spin Hamiltonian parameters for each species varying only the intensities of the components. The  $g$ -tensors and linewidth parameters from all species were obtained from a separate fitting of the last spectrum after illumination. After that the calculated spectra were summed with result of simulation of the first spectrum in order to restore original intensity of the "base" ( $H_{ox}$ -CO) signal. In all kinetic plots presented below the intensities are normalized to the intensity of the  $H_{ox}$ -CO state at the beginning of the illumination.

### 8.2.2 Kinetics

Figure 8.5 (first part) shows one of the measured kinetic profiles of the photo-dissociation process during illumination at 531nm. The intensity of the EPR signal of the  $H_{ox}$ -CO species, monotonically decreases during illumination, while the signal from  $H_{ox}$  increases. Quite interesting is the behavior of the  $L_2$  state: this signal rapidly grows

<sup>2</sup>Has been checked after each experiment

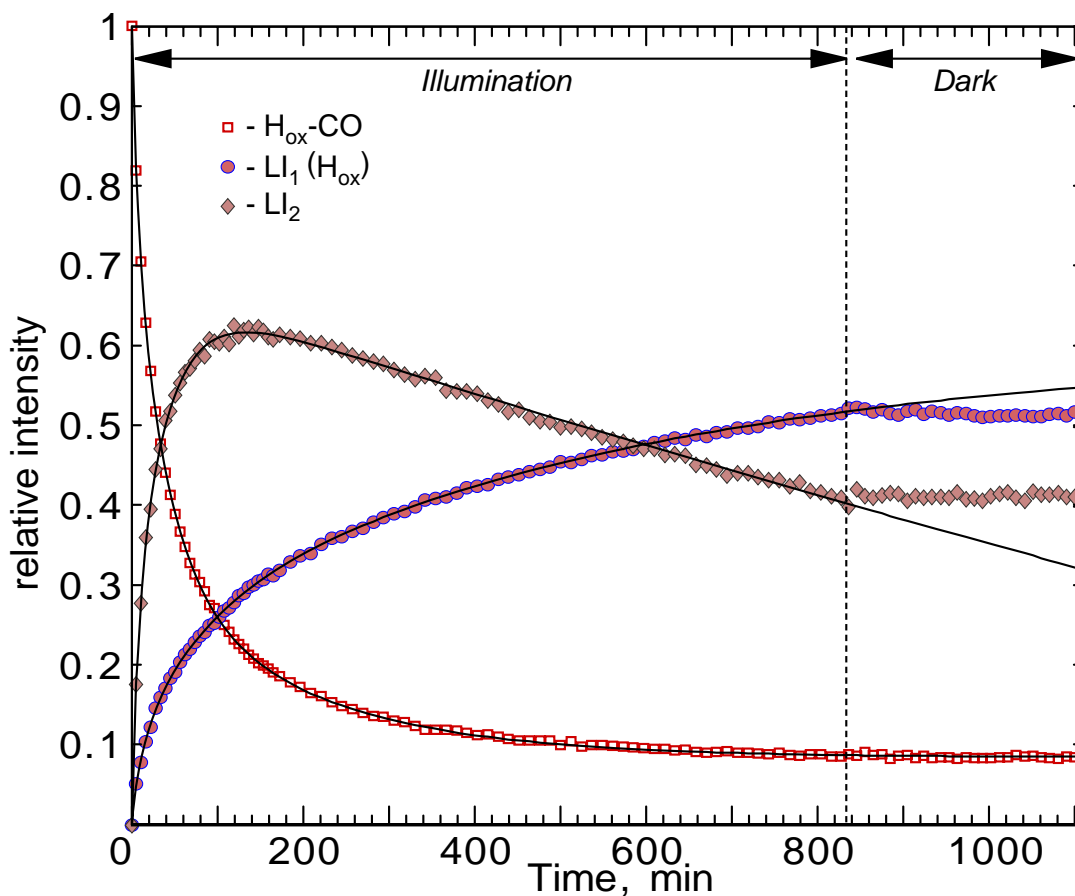


**Figure 8.5:** Changes in intensities of the ERP signals of different states of the H-cluster. Scatter plot - experimental data, solid black lines - fitting with three exponential functions. The dashed line represents the moment when the illumination was stopped. OPO laser: power, 5.4 mJ/pulse; wavelength, 531 nm.

and after a certain point starts to decrease again with a slower rate. It was found that one and two exponential fits do not give reasonable results for the kinetics of any of the species. A satisfactory fit is only possible with 3 or more exponential functions, which indicates the complexity of the pathways in the light-induced reaction. Figure 8.5 includes such a fit, using 3-exponential functions of a form:

$$I(t) = A_1 e^{b_1 t} + A_2 e^{b_2 t} + A_3 e^{b_3 t} + C$$

To check for possible "dark" reactions after illumination, the illuminated sample was left in the dark at the same temperature (40K) for several hours. During this period almost no changes in the EPR signal were detected except for a slight change at the beginning

of the "dark" phase of the experiment (see figure 8.5). However this can be attributed to slight changes in the temperature inside the resonator after switching off the illumination. Moreover, during the pulse EPR measurements, presented in the next chapter, (chapter 9) no changes in the EPR signal were found throughout several days at 5-15 K. However, leaving the sample in the dark at liquid nitrogen (77K) for a week results in the vanishing of the L<sub>2</sub> species and a decrease of the EPR signal of the H<sub>ox</sub> state with recovery of the H<sub>ox</sub>-CO state. But even after one month traces of the H<sub>ox</sub> state are visible in the EPR spectrum. Complete recovery of the H<sub>ox</sub>-CO state was found to be possible only while warming the sample above 150 K. In all experiments presented here incubation of the EPR sample in cold ethanol (200 K) in the dark was used for restoration the H<sub>ox</sub>-CO state after illumination.

It can be concluded that upon illumination the released CO from the H<sub>ox</sub>-CO H-cluster is bounds somewhere nearby the H-cluster and at cryogenic temperatures can not move back to the H-cluster. Illumination of a sample, originally in the H<sub>ox</sub> state did not result in any changes in the EPR spectrum (accept for minor signals corresponding to the photo-dissociation of the contaminating H<sub>ox</sub>-CO state).

### 8.3 Dissociation models and wavelength dependence of the conversion rates

The dependence of the photo-dissociation processes on the excitation wavelength was investigated in the range of 355 to 630 nm. The shortest possible wavelength of the OPO is 420 nm. For illumination at 355 nm the direct beam of the Nd:YAG laser working on the third harmonic of the fundamental frequency was used. In this set of experiments the power of the laser beam was adjusted to the same number of photons per pulse. The number of photons ( $n$ ) is proportional to the power of the beam ( $P$ ) multiplied by the wavelength ( $\lambda$ ):

$$n = a \cdot P \cdot \lambda/h$$

where  $a$  - is a constant, depending on the particular setup and  $h$  - is Planck's constant.

As a reference the number of photons per pulse for a wavelength  $\lambda = 420\text{nm}$  and a power per pulse of  $P_{420} = 5.8\text{mJ}$  has been used, since at this wavelength the output power of the OPO is minimum. Therefore, the necessary power of the beam for an arbitrary

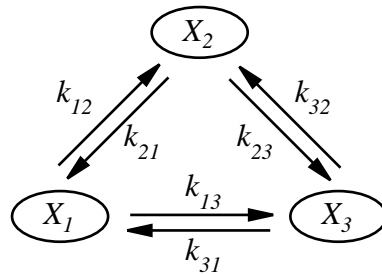
wavelength can be calculated as:

$$P(\lambda) = \frac{P_{420} \cdot 420\text{nm}}{\lambda} \quad (8.1)$$

After each photo-dissociation experiment the H<sub>ox</sub>-CO state was completely recovered by keeping the sample for 10 min in the dark in cold ethanol (200 K). Comparison of the kinetic profiles shows an increase of conversion rates with decreasing excitation wavelength. However, no direct conclusions can be made because the constants obtained by the exponential fit have no direct physical meaning. Therefore, it is necessary to derive a kinetic models, to explain the observed dependences and to interpret the extracted conversion rates.

### 8.3.1 Kinetic models

In order to make a quantitative analysis of the wavelength dependence, several conversion models have been considered. The strategy was to find the simplest possible model, which can explain the experimental data in a reasonable way. It is assumed, that there are no other states accept for H<sub>ox</sub> and L<sub>2</sub> generated during illumination. Then a general conversion scheme of three states to each other was used for the simulation.



Here  $X_i(t)$  are the time dependent concentrations (or amplitudes of the EPR signals) of the different states,  $k_{ij}$  are the rate constant of transformation from the  $i^{th}$  state to  $j^{th}$  state ( $i = 1 : 3; j = 1 : 3$ ). The kinetics of the conversion between the states in this scheme is described by the rate law (master equation):

$$\begin{cases} \frac{\partial X_1(t)}{\partial t} = -(k_{12} + k_{13}) X_1(t) + k_{21} X_2(t) + k_{31} X_3(t) \\ \frac{\partial X_2(t)}{\partial t} = k_{12} X_1(t) - (k_{21} + k_{23}) X_2(t) + k_{32} X_3(t) \\ \frac{\partial X_3(t)}{\partial t} = k_{13} X_1(t) + k_{23} X_2(t) - (k_{31} + k_{32}) X_3(t) \end{cases} \quad (8.2)$$

In photo-dissociation experiments, at the beginning ( $t = 0$ ) there is only one state populated ( $X_1$ ). Therefore, the initial conditions should be:

$$X_1(0) = 1; X_2(0) = X_3(0) = 0$$

Here, for convenience the sum of all states is normalized to '1':  $\sum_i X_i = 1$ .

Solving this system of differential equations yields the kinetic profiles of the conversion between the different states. The simulated kinetic profiles, were obtained using the numerical solution of the linear differential equations, provided by the MatLab<sup>TM</sup> programming environment.

It is important to realize, that due to the incomplete transparency of the sample different parts of it may be illuminated by light with different intensity. Therefore, to be completely correct, the simulation of the kinetic profile should include an integral over the range of intensities of the laser beam. Certainly, this also will increase number of variables. On the other hand, it was found, that the intensity of the illumination has a minor influence on the character of light-induced changes. The comparison of the kinetic profiles, obtained for different power of the OPO laser reveal almost no difference in the kinetic profiles except for a uniform 'stretching' of all curves with decreasing power of the laser (figure 8.6).

In the first model, it is assumed, that there are two ways of converting the H<sub>ox</sub>-CO state into the H<sub>ox</sub> state (figure 8.7,I). The first path is the direct conversion from the H<sub>ox</sub>-CO state to the H<sub>ox</sub> state, which means in fact the removal of the external CO ligand. The second path is indirect and proceeds over an intermediate state ( $L_2$ ). In addition a backward conversion from the H<sub>ox</sub> into the  $L_2$  was allowed in order to improve the fit to the experimental data. As it can be seen in the simulation of the photo-dissociation processes in figure 8.8, this simple model does not fit the experimental data very well. According to this model, the total conversion rate of the H<sub>ox</sub>-CO is the sum of the two conversion rates into light induced states, which is described by one exponential decay function. However, the experiment shows that the EPR signal from the H<sub>ox</sub>-CO state has a more complicated decay.

The kinetic must be more complicated. Therefore, it is concluded, that there are backward conversion processes. In the next model the presence of backward reaction from the H<sub>ox</sub> and  $L_2$  states to the H<sub>ox</sub>-CO state was taken into account (complete conversion scheme). Using this idea two models were found to give almost equal results.

The first of them is presented in figure 8.7,II. In this model, there is no direct conversion from the  $L_2$  state to the H<sub>ox</sub> state ( $k_{23}$  and  $k_{32}$  are zero). Moreover, if these constants

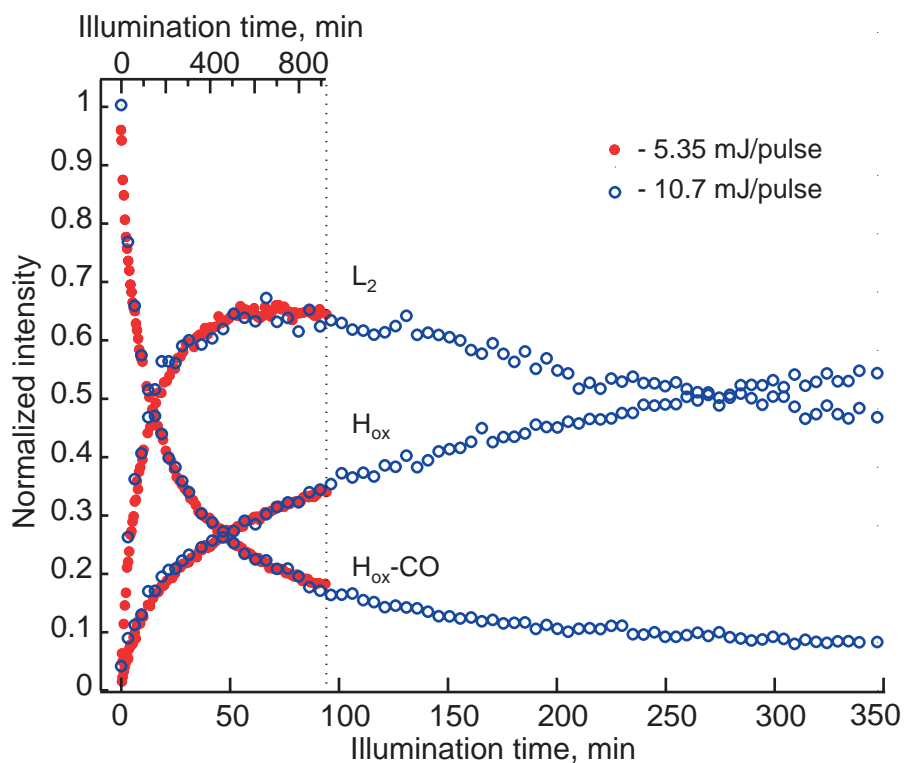


**Figure 8.6:** Comparison of light induced kinetics, obtained for different power of the OPO laser beam: 5.35 mJ/pulse and 10.7 mJ/pulse. Scale on the top (correspond to data with red dots) shrink by factor of 0.09 relative to scale on the bottom of the plot (related to data with blue circles). Experimental conditions: temperature, 40K;  $\lambda = 531$  nm.

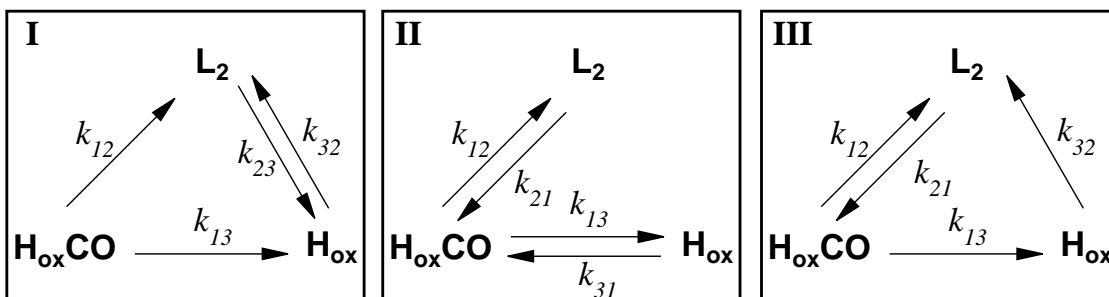


**Figure 8.7:** Considered models of the photo-dissociation pathways

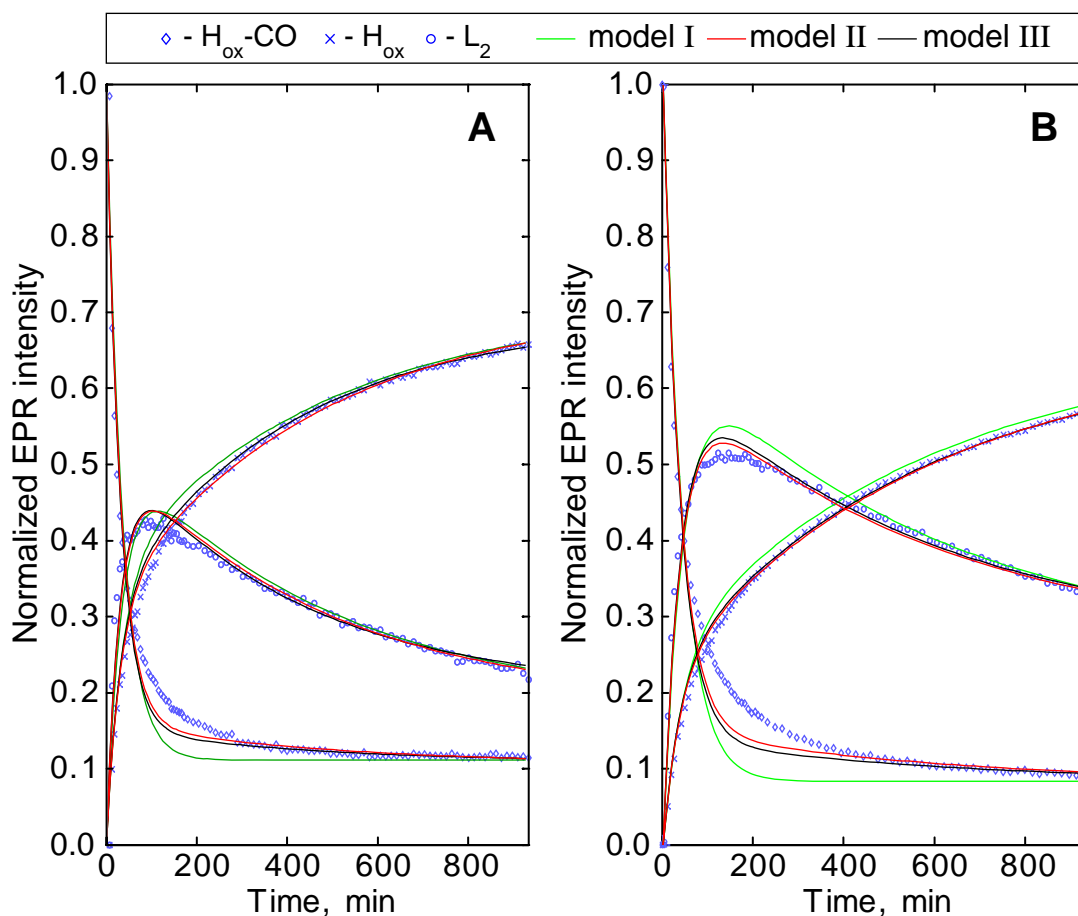


**Figure 8.8:** Dynamic of the light-induced conversions under illumination by OPO laser at 355 nm (**A**) and 531 nm (**B**) together with simulation according to models presented on figure 8.7. Experimental spectra were obtained using the same number of photons per pulse, according to formula 8.1. Experimental conditions: temperature, 40K; MW power, 20  $\mu$ W (40 dB att.); Mod. Amp, 5 G; Time const., 40 ms; MW freq., 9.780 GHz.

would be taken into account the best fit will result in almost zero values for  $k_{23}$  and  $k_{32}$ . This model includes the conversion from the  $H_{ox}$ -CO state to the  $L_2$  state (removing the bridging CO ligand) and a conversion back to the original state ( $H_{ox}$ -CO). At the same time there is a direct conversion of the  $H_{ox}$ -CO state to the  $H_{ox}$  state. It was found, that including a very slow backward conversion of the  $H_{ox}$  state to the  $H_{ox}$ -CO improves the fit.

The third model assumes no backward conversion from the  $H_{ox}$  state to the  $H_{ox}$ -CO but includes a conversion from the  $H_{ox}$  state to the  $L_2$  state (figure 8.7,III). Model II and

III both fit the experimental data quite well but still, the experimentally observed decay of the  $H_{ox}$ -CO state is slower than calculated by these models.

Certainly, further extension of these schemes, for instance, to some sort of four states dynamic will give a better fit to the experimental data. This is possible, because e.g. EPR-silent states or several identical states can be introduced, which will help to improve the fitting. However, on the other hand, merely increasing the number of the parameters will not lead to a better understanding of the photo-dissociation process in the H-cluster. In this study we will limit ourselves to the "three species" models. Model II (figure 8.7) seems to fit the long-time range data slightly better, than model III.

The third model assumes presence of  $H_{ox} \rightarrow L_2$  conversion. If in the  $L_2$  state the former bridging CO ligand is still present as terminal ligand at one of the iron atoms, this conversion requires a simultaneous change of two ligands: dissociation of one of the bonds of the bridging CO bond and reestablishing the external CO ligand. This seems quite improbable. On the other hand the bridging CO bond could be completely removed during illumination. Then the  $H_{ox} \rightarrow L_2$  conversion relates to a switch of the CO ligand from bridging position to the external site of the distal iron. But this process should be equally possible for the light-induced and the original chemically prepared  $H_{ox}$  state, since it does not require additional CO for the photo-reaction. However, illumination of the chemically prepared  $H_{ox}$  state did not reveal any photo-dissociation reaction. Hence, model III seems to be not reliable. Therefore in this study model II will be considered as the most suitable one.

#### 8.3.2 Wavelength dependence

Figure 8.9A presents the dependence of the conversion rates on the wavelength, according to model II. The error bars on the plot represents the estimated uncertainty range according to the variation of rate constants, obtained in different experiments. In total, the number of similar experiments was varying from 1 (no error bar) to 15 (for 355 nm). The obtained conversion constants show a clear rise in all rates with decreasing excitation wavelength below 500 nm. Measurements of kinetic profile at 531 nm reveal a moderate 'jump' of all rates, which was reproduced along several sets of measurements. Remarkably, the rate of  $H_{ox} \rightarrow H_{ox}$ -CO conversion ( $k_{13}$ ) is very small and remains roughly on the same level for all used wavelengths. In order to clarify the origin of this dependence, UV/Vis spectra of different states have been recorded. Figure 8.9B shows the UV/Vis spectra of the as-isolated and the reduced states. To facilitate direct

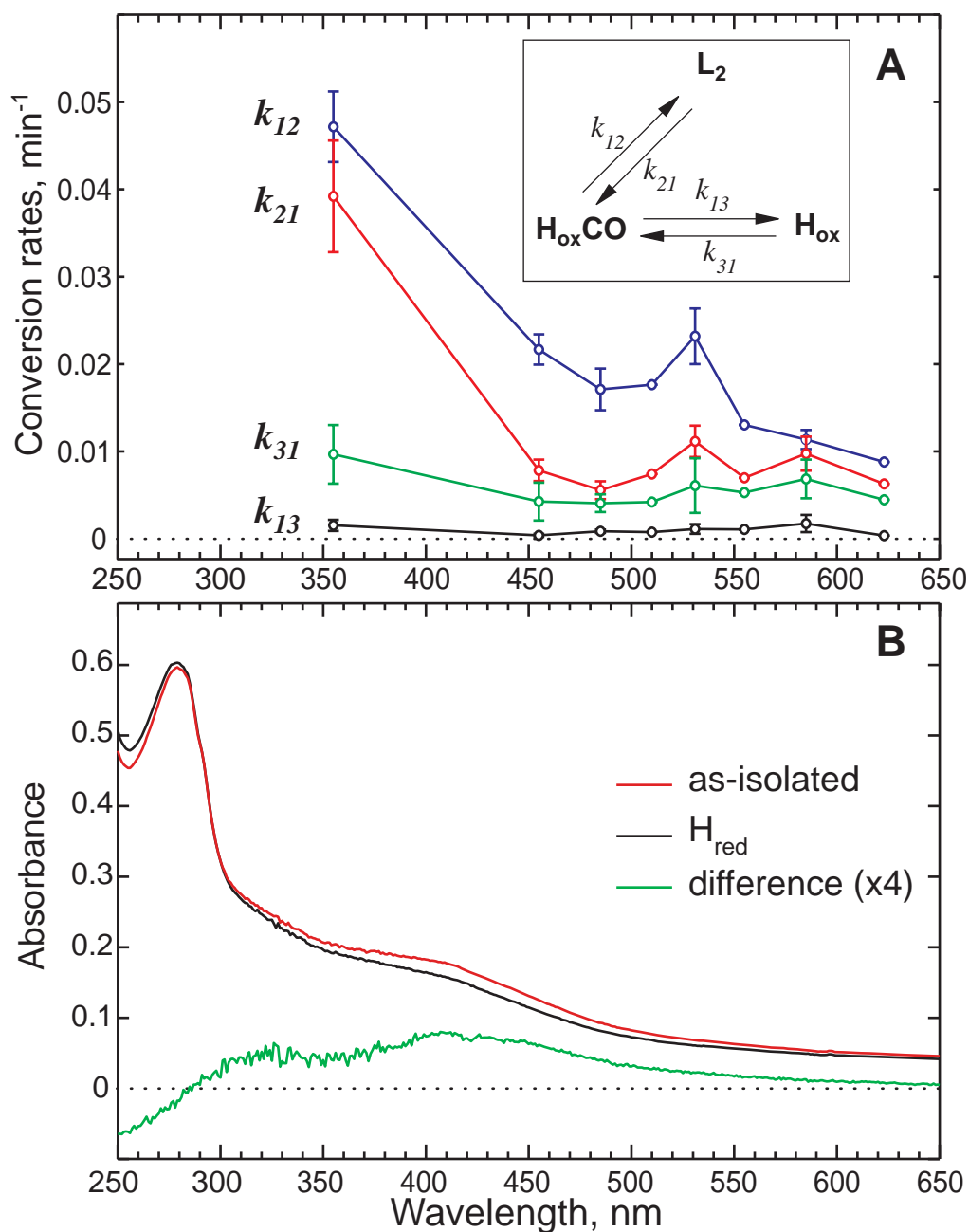


**Figure 8.9:** Wavelength dependence of the photo-dissociation rates **A** and UV-Vis spectra of the [FeFe] hydrogenase in the as-isolated and in the  $H_{red}$  states **B**. UV-Vis spectra were taken at room temperature. Sample of roughly  $16\mu\text{M}$  in  $17\mu\text{L}$  was diluted in 1 mL of distilled water. Photo-dissociation rates were extracted from experimental data using model II as shown in the insert.

## 8.4 Summary and discussion

---

**Table 8.1:** Wavelength dependence of the photo-dissociation rate constants. Rate constants were extracted from the experimental data using model II. Values in parentheses are uncertainties in units of the least significant digit.

$\lambda$ (nm)	$k_{1,2}$ ( $\text{min}^{-1}$ )	$k_{2,1}$ ( $\text{min}^{-1}$ )	$k_{3,1}$ ( $\text{min}^{-1}$ )	$k_{1,3}$ ( $\text{min}^{-1}$ )
355	0.047(4)	0.039(6)	0.010(3)	0.0015(4)
455	0.021(2)	0.007(1)	0.004(2)	0.0004(2)
485	0.017(2)	0.005(1)	0.004(1)	0.0008(2)
510	0.017(-)	0.007(-)	0.004(-)	0.0007(-)
531	0.023(3)	0.011(2)	0.006(3)	0.0011(3)
555	0.013(-)	0.006(-)	0.005(-)	0.0010(-)
585	0.011(1)	0.009(2)	0.007(2)	0.0017(4)
623	0.008(-)	0.006(-)	0.004(-)	0.0003(-)

comparison of UV/Vis spectra, all states were prepared using the same sample. As shown in early study, activation of the protein by  $\text{H}_2$  gas leads to a decrease of the absorption in the region of 300-600 nm, which is attributed to the changes in oxidation state of the iron-sulfur clusters including the H-cluster. The comparison of this signal with the relaxation rates shows some difference in the low wavelength region. This shows, that the conversion rates do not directly correspond to an 'attenuation' of the illumination by the F-clusters. On the other hand, the overall shape of the UV/Vis spectrum fits to the found kinetic rates quite well except for some moderate jump in the rates at 531 nm.

## 8.4 Summary and discussion

It was found in this study that two EPR active states appear during illumination of the enzyme in the  $\text{H}_{\text{ox}}\text{-CO}$  state. One of these states has been identified using ENDOR spectroscopy to be the  $\text{H}_{\text{ox}}$  state, characterized by a missing external CO bond. Fitting of the photo-dissociation kinetic profiles by different models suggests that in contrast to previous investigations, in which the second light-induced state had been described as a minor state, this is a separate state, which plays an important role in the conversion of the  $\text{H}_{\text{ox}}\text{-CO}$  state to the  $\text{H}_{\text{ox}}$  state.

Modelling of the photo-dissociation processes have suggested that there is no direct conversion from the  $\text{L}_2$  state to the  $\text{H}_{\text{ox}}$  state. Using this model, it was found, that the conversion of the  $\text{H}_{\text{ox}}\text{-CO}$  state to the  $\text{L}_2$  state is considerably faster than the conversion

to the  $H_{ox}$  state. It may indicate that the bridging CO bond is not removed completely. However it should be noted that the bonding of the external CO ligand is, in general, stronger. Nevertheless, the fact that the backward transformation from the  $L_2$  state to the  $H_{ox}$ -CO state is the second fastest light-induced process supports the idea about partial dissociation of the bridging ligand.

As was observed experimentally, all transformations (including back conversions) are photo-induced, which indicates, that both light-induced species are stable at cryogenic temperatures. Investigation of the wavelength dependence of the rates shows that of all conversion rates increase with decreasing laser wavelength. Comparison of this wavelength dependence with the UV/Vis spectra reveals general similarity. However the weak peak around 531 nm was not reproduced in the UV/Vis spectra.

According to a study of bi-nuclear model complexes [106], UV-Vis spectra reveal a peak around 320 nm for the complex of  $Fe_2(pdt)(CO)_6$ , which is shifting to 355 nm with the substitution of two carbon monoxide ligands by cyanides ( $Fe_2(pdt)(CO)_4(CN)_2^{2-}$ ) [106]. Using theoretical calculations (DFT), this peak was assigned to HOMO-2  $\rightarrow$  LOMO ( $Fe(t_{2g}) - Fe(\sigma^*)$ ) excitation [97]. Therefore it can be concluded, that the photo-dissociation processes are related to the excitation of the metal-metal bond in the bi-nuclear subcluster.

The theoretical modeling of the catalytic cycle, presented in [12, 59], has shown that one of the possible intermediate states is characterized by the absence of the bridging CO bond while instead an additional terminal CO bond is present at the distal iron. In this state the iron atoms of the bi-nuclear subcluster were modeled to remain in the mixed valence state. Since the  $L_2$  state is characterized by dissociation of the bridging CO bond it seems likely that it has properties similar to the modeled state. Therefore it is very important to undertake a detailed investigation of the electronic structure of the  $L_2$  state. The following chapter presents the first pulse EPR study of the second light induced state.



# 9

---

## The second light induced state

---

Investigation of the second light induced state, discovered during photo-dissociation experiments of the  $H_{ox}$ -CO state [36, 38, 47], is very important for understanding of changes in the electronic structure of the H-cluster due to dissociation of the bridging CO. Moreover, the structure of this state is not yet known. The FT-IR investigation of this state suggests partial or complete dissociation of the bridging CO ligand [36, 38]. The study presented above suggested that the former bridging CO ligand is not completely dissociated but became a terminal ligand of one of the irons in the binuclear subcluster. The key to understanding the structure of the H-cluster in this state is to investigate its electronic structure and compare it with that of the others. Application of the EPR methods, which have already provided an extensive knowledge about the  $H_{ox}$  and the  $H_{ox}$ -CO state, may give important information to answer these structural questions. The work presented below had an aim to resolve the electronic structure of the H-cluster in the  $L_2$  state in great details.

### 9.1 EPR spectra

In the study presented here, the  $L_2$  state was generated by illumination of the  $H_{ox}$ -CO state with laser of 531 nm wavelength at 50 K. The study has been performed mostly at Q-band pulse EPR spectrometer. Photo-dissociation processes were controlled using 2-pulse echo-detection. However, it turned out, that only one signal, namely the  $H_{ox}$ -CO state, can be detected at 50 K. This phenomena due to the difference in relaxation rates for different species. Observation of all three species, involved in the photo-dissociation ( $H_{ox}$ ,  $H_{ox}$ -CO and  $L_2$ ) by pulse EPR methods was found to be possible only for temperatures below 15K, which points to relatively fast relaxation rates in the case of the  $L_2$  state.

Nevertheless, since the kinetics of the photo-dissociation processes have been measured in the previous chapter (see chapter 8), it is possible to estimate the amount of light induced species from the decay of the EPR signal of the  $H_{ox}$ -CO state. As follows from figure 8.5, the maximum intensity of the EPR signal of the  $L_2$  state is achieved when

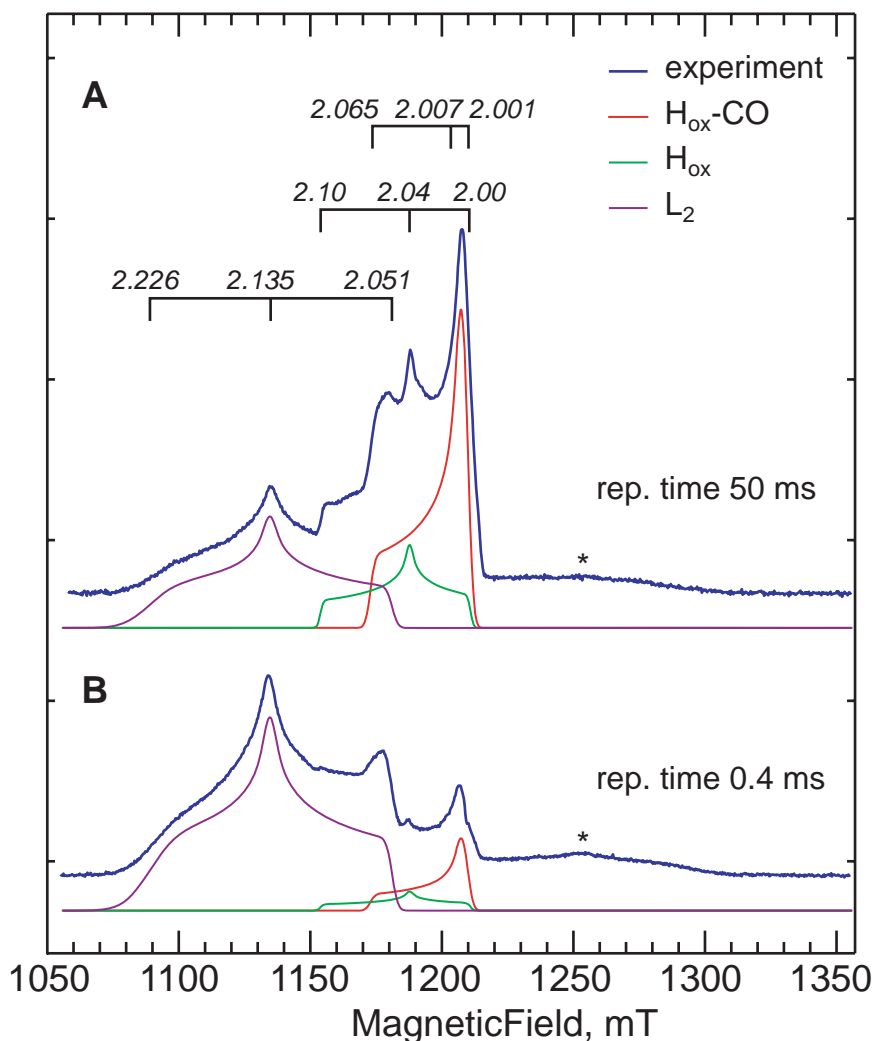


**Figure 9.1:** Q-band FID-detected EPR spectra of the product of illumination of the  $H_{ox-CO}$  state at temperature of 50 K. Measurements has been preformed at temperature of 8 K using different repetition rate. Experimental conditions:  $t_{mw} = 1$  ms **A** rep.time, 50 ms (tuned at 1205.0 mT,  $g_3^{CO}$ ); **B**. rep.time, 0.4 ms (tuned at 1135.0 mT,  $g_2^{L_2}$ ).

the signal of the  $H_{ox-CO}$  state decreases roughly four times. At this moment amount of the obtained  $L_2$  state is maximum. According to this criterion the illumination was stopped when the EPR signal of the  $H_{ox-CO}$  state at 50 K decreased by a factor of four from original signal intensity. In figure 9.1, the EPR spectra, taken after illumination for 45 min at 531 nm with 10 mJ power per pulse, are shown. As has been described in the chapter 8, the  $L_2$  state reveals the following characteristic  $g$ -values (X-band EPR

spectrum):  $g = (2.226, 2.135, 2.051)$ . Measurements at Q-band confirmed this finding. Due to the difference in relaxation rates of the observed states, different parts of the EPR spectrum require different experimental settings (i.e. repetition rate) to obtain maximum amplitudes.

The top spectrum of figure 9.1 was recorded at 8 K under non-saturating conditions, tuned at  $g = 2.00$ . At this temperature, the shortest repetition time which allows detection of an unsaturated  $H_{ox}$ -CO signal, was found to be about  $50 \mu s$ , while for the  $L_2$  signal it is 2 orders of magnitude shorter: about  $0.4 \mu s$ . The bottom spectrum on the figure 9.1 has been measured at these conditions, but then the signals of the other species ( $H_{ox}$  and  $H_{ox}$ -CO) are partially saturated. Since the structure of the  $L_2$  state is not yet known, it is very interesting to study the hyperfine (HF) interactions of this state in greater detail.

## 9.2 Investigation of the $^{57}Fe$ HF couplings

The knowledge about the  $^{57}Fe$  HF couplings is of major importance for resolving the electronic structure of the H-cluster, since the irons carry most of the spin-density. Like in previous investigations of the  $^{57}Fe$  HF couplings in the  $H_{ox}$  and the  $H_{ox}$ -CO states, two complementary methods have been applied: ESEEM (HYSCORE) and ENDOR.

Q-band HYSCORE spectra reveal two pairs of ridges, which can be assigned to  $^{57}Fe$  HF couplings. The experimental spectra are shown in figures 9.2 and 9.3 together with simulations. Similar to the case of the  $H_{ox}$ -CO state, these spectra show one pair of ridges in the  $(++)$  quadrant and one in the  $(+-)$  quadrant of the 2D spectrum. Measurements of HYSCORE spectra at different field positions show, that the weak coupling is almost completely anisotropic. Since position of the other ridges does not change much with varying the external magnetic field, it was concluded that other  $^{57}Fe$  HF coupling is mostly isotropic. Table 9.1 shows the estimated HF constants ( $A_{Fe}^1$  and  $A_{Fe}^2$ ).

In addition, the Q-band HYSCORE spectra also reveal some ridges, for which the

**Table 9.1:** HF interaction parameters, related to the  $^{57}Fe$  nuclei, found for the H-cluster in the  $L_2$  state.

	$A_{xx}$	$A_{yy}$	$A_{zz}$	$ A_{iso} $	$[\varphi, \theta, \psi]$
	MHz	MHz	MHz	MHz	degree
$A_{Fe}^1$	3.3(3)	4.8(5)	3.9(3)	4.0(4)	$[0, 0, 40] \pm 30$
$A_{Fe}^2$	2.7(2)	1.6(4)	-3.3(2)	0.3(3)	$[0, -15, 0] \pm 10$
$A_{Fe}^3$	25(5)	20(1)	20(5)	22(4)	<i>n.d.</i>

\* Values in parentheses are uncertainties in units of the last significant digit.

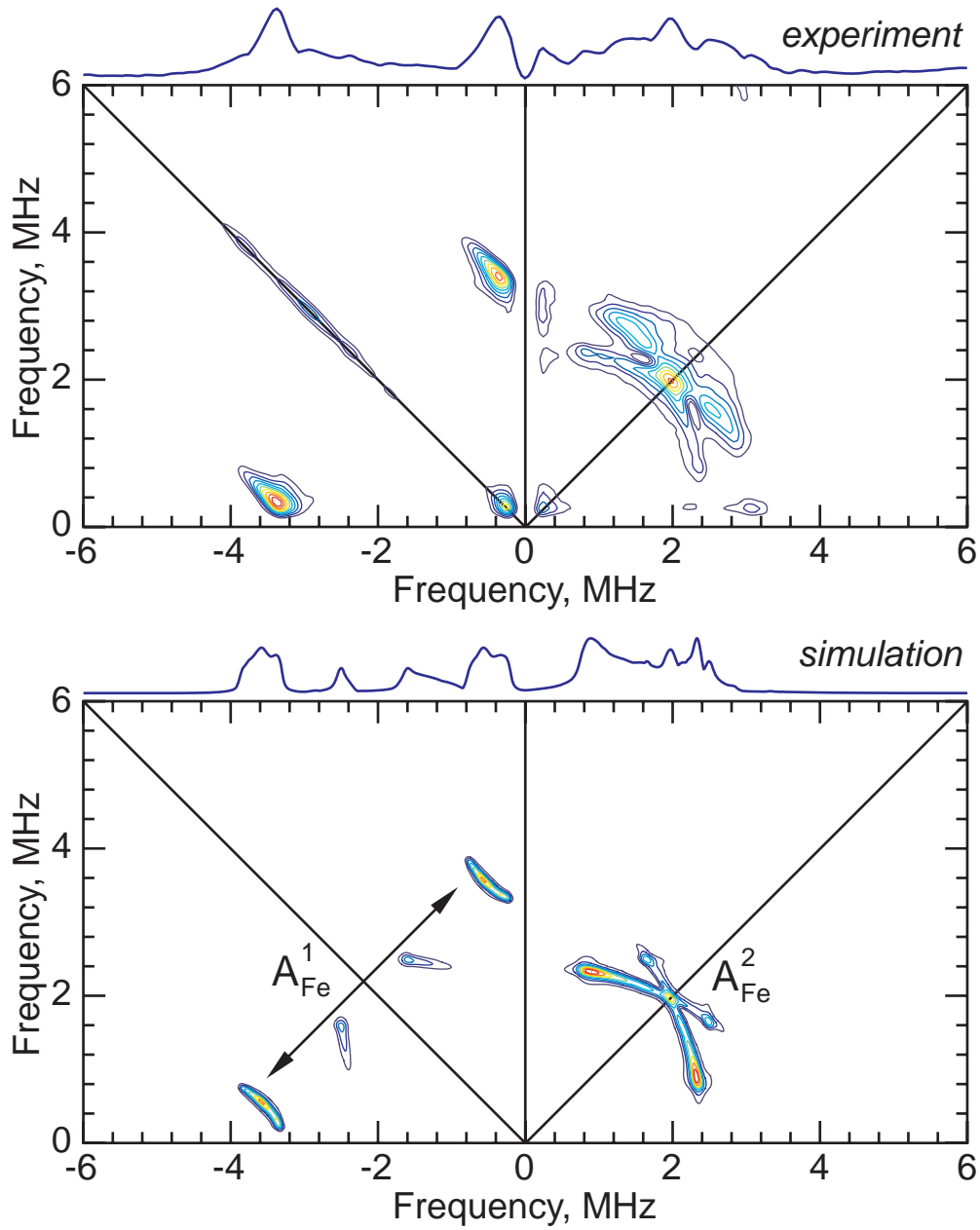


**Figure 9.2:** Q-band HYSORE spectrum of the  $^{57}\text{Fe}$ -enriched H-cluster in the  $L_2$  state, measured at  $B_0 \parallel g_2^{L_2}$  together with a simulation performed using the parameters  $A_{\text{Fe}}^1$  and  $A_{\text{Fe}}^2$  from table 9.1. Experimental conditions: temperature, 6K; MW frequency, 33.88 GHz; magn. field, 1134 mT;  $\tau = 340$  ns; rep.time, 1 ms.

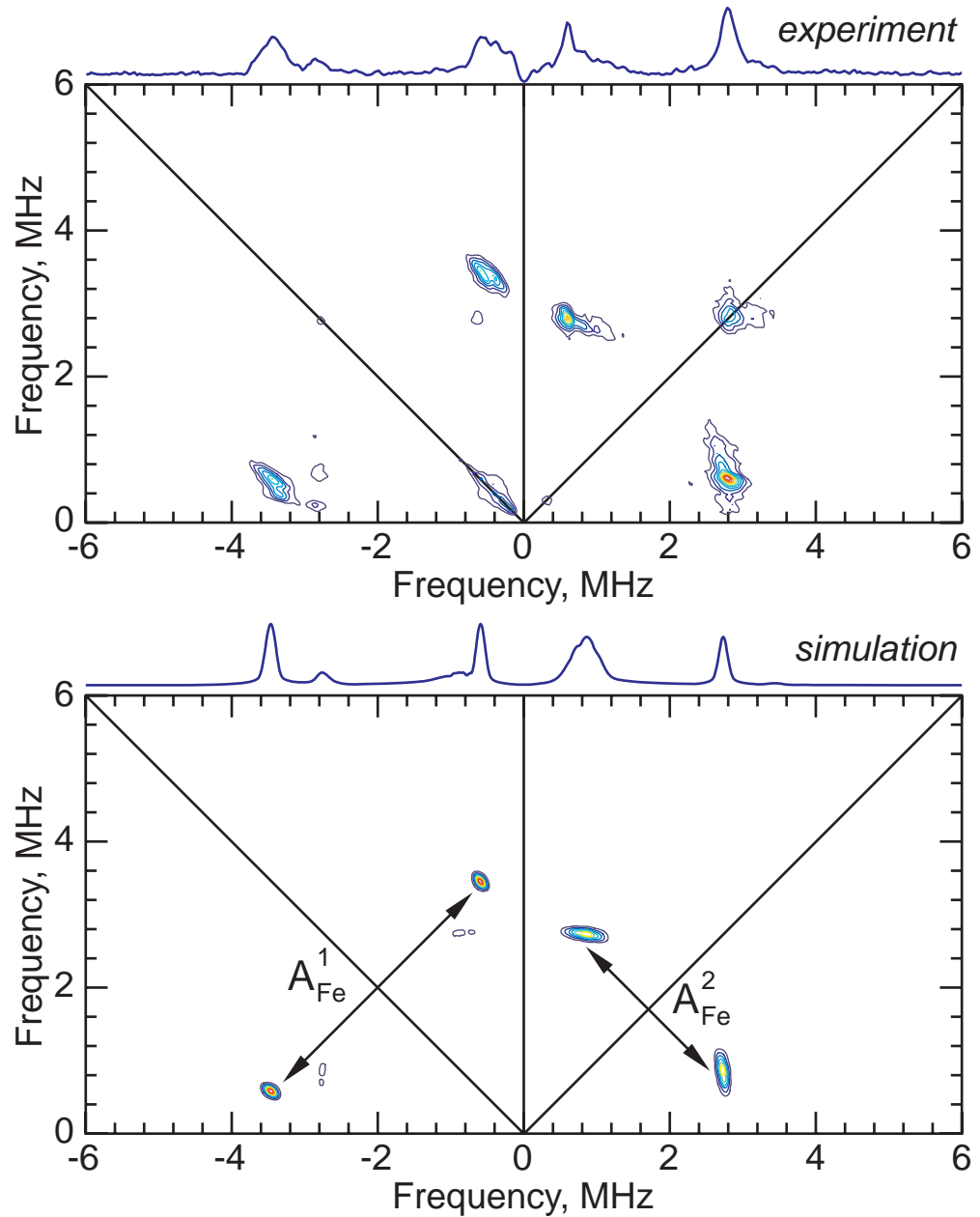


**Figure 9.3:** Q-band HSCORE spectrum of the  $^{57}\text{Fe}$ -enriched H-cluster in the  $L_2$  state, measured at  $B_0 \parallel g_1^{L2}$  together with a simulation performed using the parameters  $A_{\text{Fe}}^1$  and  $A_{\text{Fe}}^2$  from table 9.1. Experimental conditions: temperature, 8K; MW frequency, 33.90 GHz; magn.field, 1085 mT;  $\tau = 320$  ns, rep.time, 0.5 ms.

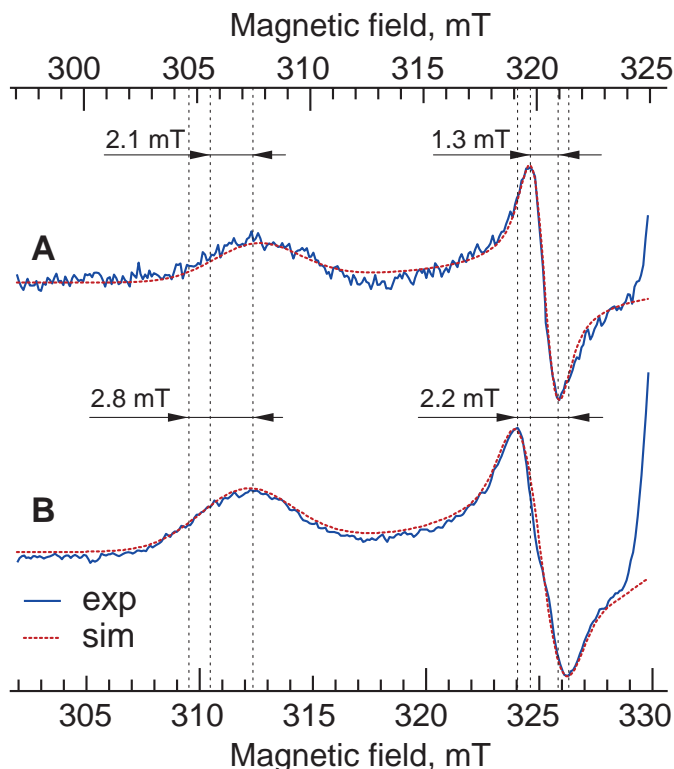


**Figure 9.4:** Low field ( $g_1^{L2}$  and  $g_2^{L2}$ ) components of the X-band CW EPR spectra of the non-enriched **A** and  $^{57}\text{Fe}$ -enriched (**B**) H-cluster in the  $L_2$  state together with simulations. Simulation of the spectrum of the  $^{57}\text{Fe}$ -enriched H-cluster was done using four  $A_{Fe}^3$  HF coupling constants (see table 9.1). Experimental conditions: temperature, 40 K; MW power,  $63.2 \mu\text{W}$  (35 dB att.); mod.amp., 5 G; time const, 40.96 ms; mod.freq., 100 kHz; **A** MW freq., 9.575 GHz; **B** MW freq., 9.711 GHz.

behavior of the magnetic field is not consistent with  $^{57}\text{Fe}$  nuclei. Since in this frequency range no  $^1\text{H}$  signals are expected ( $\nu_{1H} \approx 50$  MHz), these ridges were assigned to  $^{14}\text{N}$  nuclei. Indeed, the HYSCORE spectra at X-band are quite complex, which is typical for  $^{14}\text{N}$  nuclei with HF couplings, close to exact cancellation (see section below).

Despite the successful investigation of  $^{57}\text{Fe}$  HF couplings in the  $\text{H}_{\text{ox}}$  and the  $\text{H}_{\text{ox}}\text{-CO}$  state by ENDOR spectroscopy (chapters 6 and 7), Davies ENDOR measurements of the  $L_2$  state in the range of 5 to 60 MHz did not reveal any traces of  $^{57}\text{Fe}$  nuclei. Failure of this method can be due to the fast spin relaxations.

Another method to verify the presence of strong  $^{57}\text{Fe}$  HF interaction is the investigation of the line broadening due to the presence of the  $^{57}\text{Fe}$  isotope. The EPR spectrum

of the  $L_2$  state suffers from overlap with signals from other species ( $H_{ox}$ -CO and  $H_{ox}$ ). Moreover, since the low-field component of the spectrum is quite broad, only a rough analysis can be done. CW EPR spectra of the non-enriched and  $^{57}\text{Fe}$  labeled enzyme in the  $L_2$  state reveal a broadening of the central component of the spectra by approximately 0.9 mT (peak-to-peak), as it is shown in figure 9.4.

Maximum of 6  $^{57}\text{Fe}$  HF couplings expected to find from the H-cluster. However, accounting 4 equivalent couplings of  $A_{Fe}^1$  and 2 couplings of  $A_{Fe}^2$  is not enough to simulate the line-broadening. Therefore, by analogy with the  $H_{ox}$ -CO state, it was assumed that the HF couplings ( $A_{Fe}^1$  and  $A_{Fe}^2$ ) are correspond to the  $^{57}\text{Fe}$  nuclei in the bi-nuclear cluster. Then there should be four strong HF couplings present, which originate from the  $[4\text{Fe}4\text{S}]_H$  subcluster. Consequently four identical strong HF couplings were taken into account in the simulations of the CW EPR spectrum of  $L_2$ . The best fit to the experimental data is given by simulation with four HF couplings  $A_{Fe}^3 = [25, 20, 20]\text{MHz}$ , one  $A_{Fe}^1$  and one  $A_{Fe}^2$ . However, the overall uncertainty range is quite large. Moreover, the  $A_{Fe}^3$  HF tensor can be not collinear with g-tensor (as it was assumed in simulation).

The extracted  $A_{Fe}^3$  HF coupling is somewhat smaller than ones, observed for the  $H_{ox}$ -CO state. This may point to the relatively weak  $[2\text{Fe}]_H$ - $[4\text{Fe}4\text{S}]_H$  exchange interaction. However, since precision of the determined  $A_{Fe}^3$  HF coupling constants is quite low, this statement needs to be proved.

### 9.3 $^1\text{H}$ ENDOR study

One of the possible evidence of the  $[2\text{Fe}]_H$ - $[4\text{Fe}4\text{S}]_H$  exchange interaction is the magnitude of the  $^1\text{H}$  HF interaction. It is believed that  $^1\text{H}$  ENDOR signals are mostly due to the non-exchangeable  $\beta$ -protons of the Cys of the  $[4\text{Fe}4\text{S}]_H$  subcluster [49, 102]. The strength of the  $^1\text{H}$  HF interactions is directly related to the effective spin-density in the 'cubane'. Consequently it may be used as an indication of magnitude of the exchange interaction between the  $[2\text{Fe}]_H$  and  $[4\text{Fe}4\text{S}]_H$  subclusters<sup>1</sup>. Therefore, a quantitative analysis of the  $[2\text{Fe}]_H$ - $[4\text{Fe}4\text{S}]_H$  exchange interaction in the  $L_2$  state can be done from comparison of the  $^1\text{H}$  ENDOR spectra of the  $L_2$  state with those of the  $H_{ox}$  and  $H_{ox}$ -CO states.

Measurements of the  $^1\text{H}$  ENDOR were performed for all three states ( $H_{ox}$ ,  $H_{ox}$ -CO and  $L_2$ ) of the H-cluster. In order to make a clear comparison the  $H_{ox}$ -CO and  $H_{ox}$  states were

<sup>1</sup> Here it is assumed that the geometry of Cys ligands of the  $[4\text{Fe}4\text{S}]_H$  subcluster are the same in the  $L_2$ ,  $H_{ox}$  and  $H_{ox}$ -CO states.

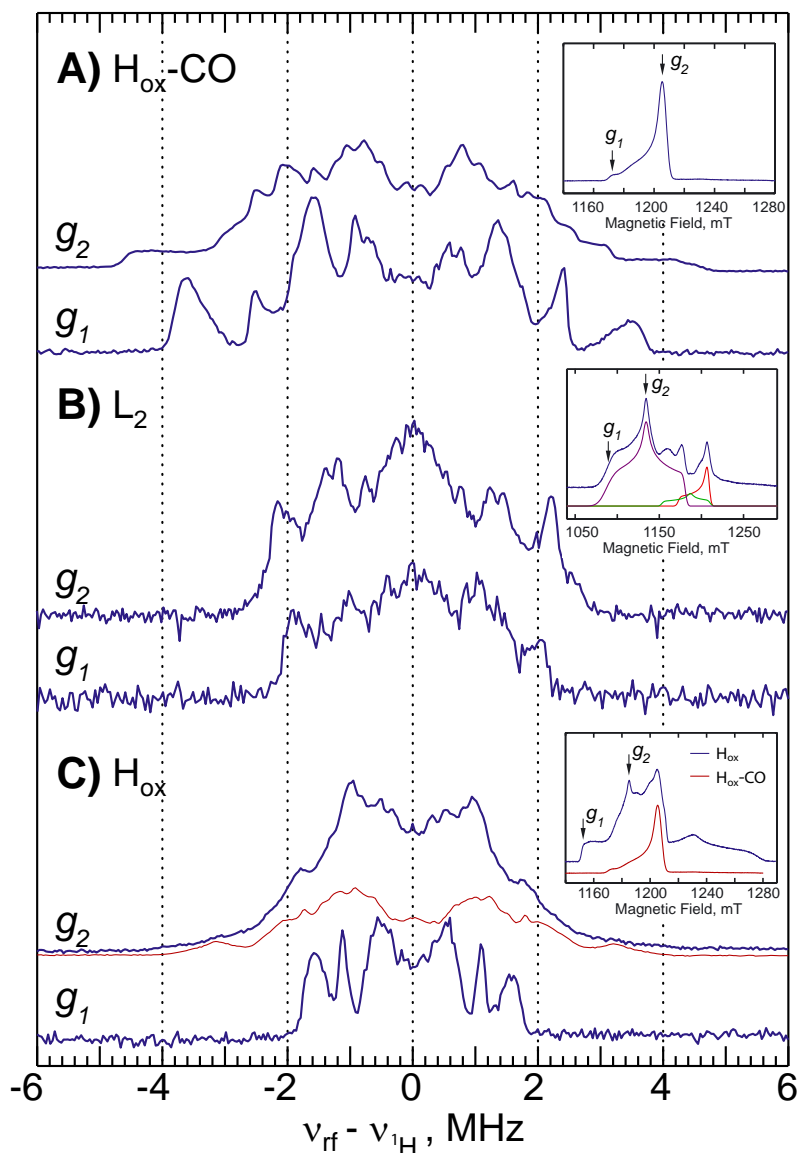


**Figure 9.5:** Q-band  $^1\text{H}$  Davies ENDOR spectra of the  $\text{H}_{\text{ox}}\text{-CO}$  (**A**), the  $\text{L}_2$  (**B**) and the  $\text{H}_{\text{ox}}$  (**C**) states of the H-cluster measured at different magnetic fields. Experimental conditions: **A**, temperature, 15 K; MW freq., 33.85 GHz,  $t_{\text{rf}} = 19\mu\text{s}$ ; magn.field, 1169.5mT( $g_1^{\text{CO}}$ ) and 1205mT( $g_2^{\text{CO}}$ ); **B**, temperature, 8 K; MW freq., 33.90 GHz,  $t_{\text{rf}} = 10\mu\text{s}$ ; magn.field, 1085mT( $g_1^{\text{L2}}$ ) and 1135mT( $g_2^{\text{L2}}$ ); **C**, temperature, 15 K; MW freq., 33.85 GHz,  $t_{\text{rf}} = 19\mu\text{s}$ ; magn.field, 1151.5 mT( $g_1^{\text{ox}}$ ) and 1185.7 mT( $g_2^{\text{ox}}$ );

prepared chemically. However, as it was already discussed in the chapter 7, the sample of the  $H_{ox}$  state reveal some contamination of the  $H_{ox}$ -CO state. The resulting spectra are shown in figure 9.5. The ENDOR spectra of the  $H_{ox}$ -CO state show  $^1H$  ENDOR signal with a maximum splitting of approximately 10 MHz, (at  $g_2^{co}$ ,  $B_0 = 1205mT$ ). The ENDOR spectra of the  $H_{ox}$  state reveal signals with maximum splitting of about 3 MHz (at  $g_2^{ox}$ ,  $B_0 = 1185.7mT$ ). This observation is in good agreement with what was found in the study of the  $^{57}Fe$  HF couplings, where exchange interaction between the subunits of the H-cluster is increasing from the  $H_{ox}$  state to the  $H_{ox}$ -CO state (chapters 6 and 7). The  $^1H$  ENDOR spectra of the  $L_2$  state reveal a signal with a maximum splitting close to 5 MHz which is an intermediate value between those found for the  $H_{ox}$  and the  $H_{ox}$ -CO states. From a general comparison of the shape of the  $^1H$  ENDOR spectra of the  $H_{ox}$ , the  $H_{ox}$ -CO and the  $L_2$  states, it is possible to conclude, that the strength of the  $[2Fe]_H$ - $[4Fe4S]_H$  exchange interaction in the  $L_2$  state is weaker than in the  $H_{ox}$ -CO state and stronger than in the  $H_{ox}$  state. However, the full analysis of these spectra is impossible, due to overlapping of signals from at least 8 protons.

In the  $H_{ox}$  state the HF coupling constants for the  $^{57}Fe$  nucleus in the  $[4Fe4S]_H$  were found to be around 11 MHz, while in the  $H_{ox}$ -CO state they are in the range of 22-38 MHz. The values of about 20 MHz for the  $^{57}Fe$  HF couplings for the  $[4Fe4S]_H$  subcluster of the  $L_2$  state is in between of those from the  $H_{ox}$  and  $H_{ox}$ -CO states. This fits to the scenario of moderate weakening of the  $[2Fe]_H$ - $[4Fe4S]_H$  exchange coupling with dissociation of the bridging CO ligand, suggested according to the  $^1H$  ENDOR study.

#### 9.4 Investigation of the $^{14}N$ nuclear spin interactions

Information about  $^{14}N$  nuclear spin interactions (i.e. HF and quadrupole interactions) would improve our knowledge about the distribution of the spin density over the CN ligands in the  $[2Fe]_H$  subcluster. Because of the successful study of the  $^{14}N$  nuclear spin interactions in the case of  $H_{ox}$  (see section 7.3), it is quite tempting to apply the same technique for further characterization of the electronic structure of the H-cluster in the the  $L_2$  state. Just as for the  $H_{ox}$  state, in this study X-band HYSCORE spectroscopy has been chosen. The optimum temperature for the EPR measurements of the  $L_2$  state is lower (6-8 K) than for the  $H_{ox}$  and  $H_{ox}$ -CO states. Therefore using the relatively short repetition rate results in the saturation of the overlapping signals from the  $H_{ox}$  and the  $H_{ox}$ -CO states. Hence the signals of the  $L_2$  species are dominant in the HYSCORE spectra, measured at

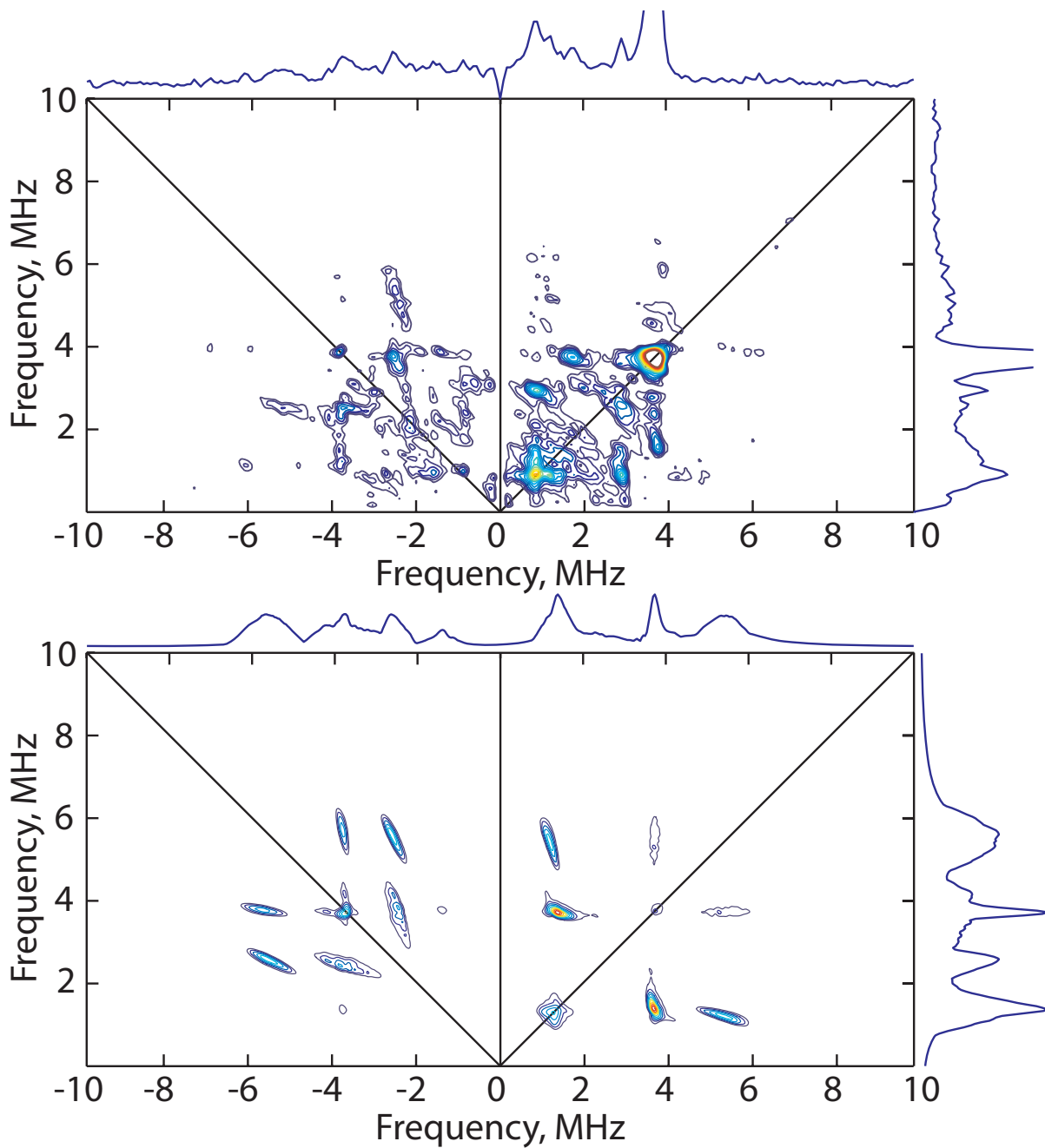


**Figure 9.6:** Experimental (top) X-band HYSORE spectra of the  $L_2$  state of the H-cluster for  $g_1$  position of the static magnetic field and its simulation (bottom). Experimental conditions: temperature, 8K; MW freq., 9.717 GHz; magn.field, 312.0 mT;  $\tau = 132$  ns. Simulation assumes one  $^{14}\text{N}$  coupled nucleus.

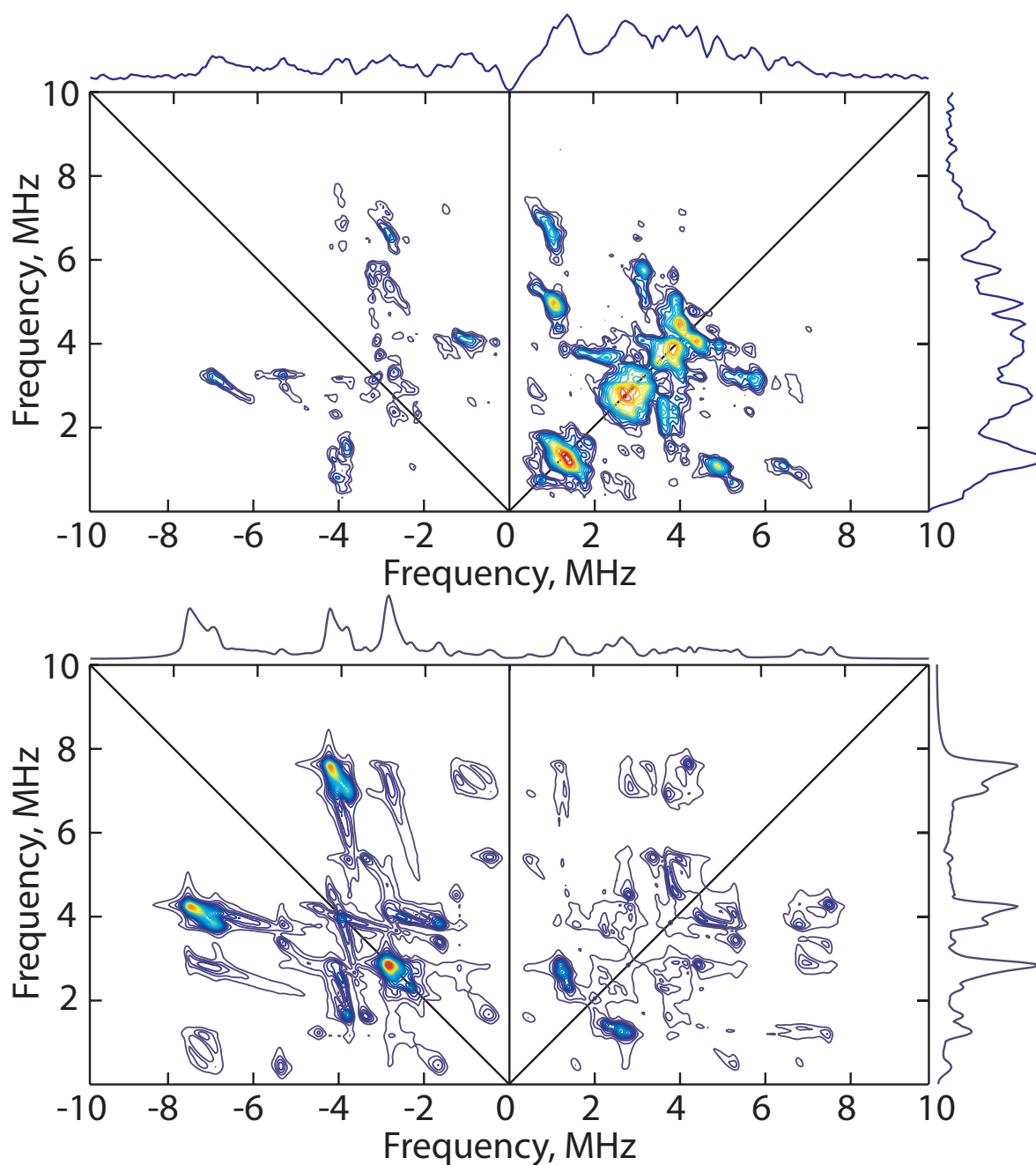


**Figure 9.7:** Experimental (top) X-band HSCORE spectra of the  $L_2$  state of the H-cluster for  $g_2$  position of the static magnetic field and its simulation (bottom). Experimental conditions: temperature, 12K; MW freq., 9.717 GHz; magn.field, 325.5 mT;  $\tau = 132$  ns. Simulation assumes one  $^{14}\text{N}$  coupled nucleus.

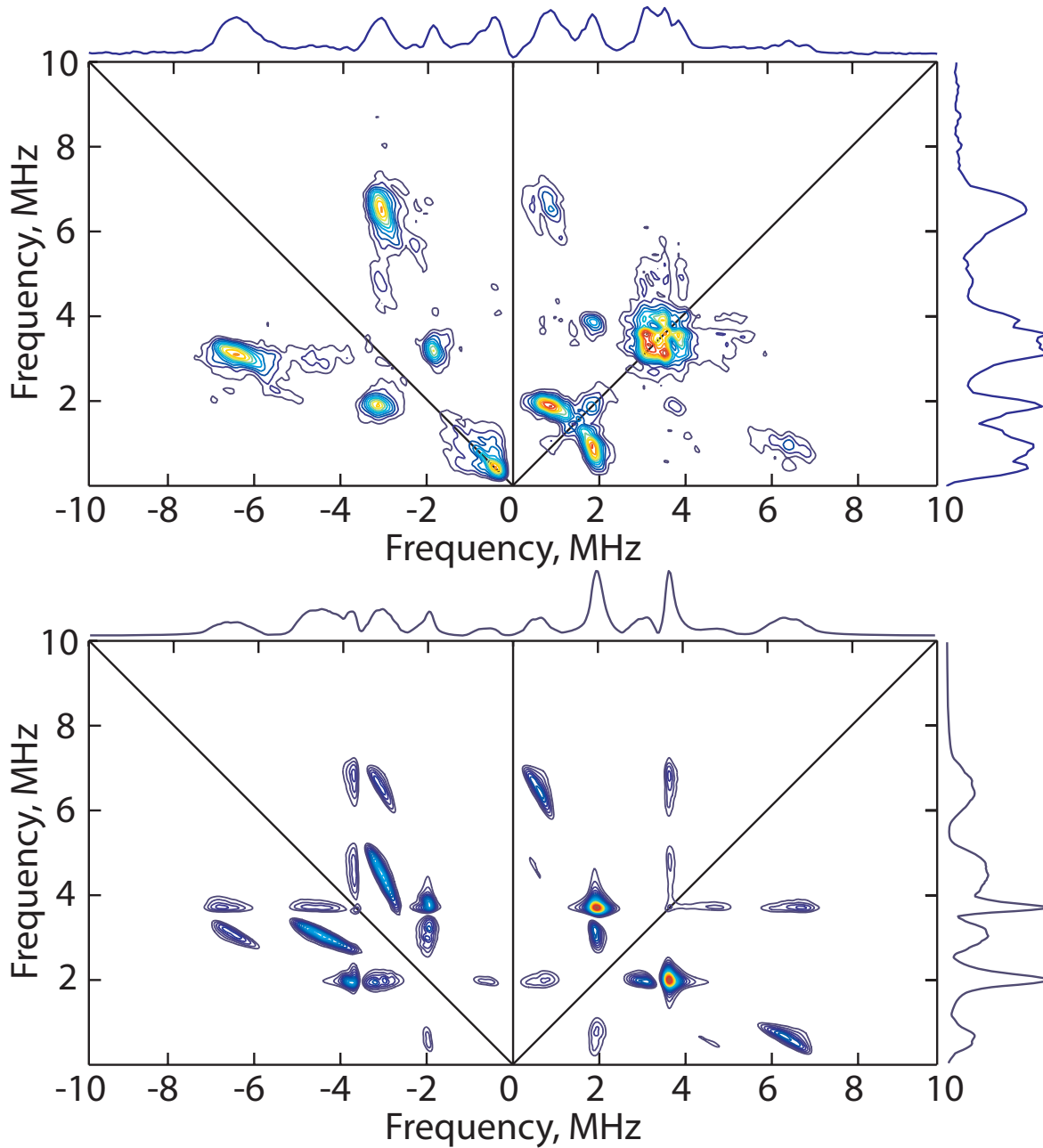


**Figure 9.8:** Experimental (top) X-band HSCORE spectra of the  $L_2$  state of the H-cluster for the static magnetic field close to  $g_3$  and its simulation (bottom). Experimental conditions: temperature, 8K; MW freq., 9.717 GHz; magn.field, 338.3 mT;  $\tau = 132$  ns. Simulation assumes one  $^{14}\text{N}$  coupled nucleus.

the high field component of the EPR spectrum ( $g_3^{L_2} = 2.051$ ) where it is overlapping with signals of the  $H_{ox}$  and the  $H_{ox}$ -CO states.

Figures 9.6, 9.7 and 9.8 show the X-band HYSCORE spectra measured at different positions of the static magnetic field together with their simulation. It was found, that most of the ridges in the spectra can be interpreted using only one  $^{14}\text{N}$  nucleus. Parameters used for the simulations are following:

***Hyperfine interaction***

$A_{xx}$ (MHz)	$A_{yy}$ (MHz)	$A_{zz}$ (MHz)	$ A_{iso} $ (MHz)	$\varphi$ (deg)	$\theta$ (deg)	$\psi$ (deg)
$5.1 \pm 0.2$	$4.5 \pm 0.2$	$0.6 \pm 0.2$	$3.4 \pm 0.2$	$40 \pm 10$	$34 \pm 10$	$10 \pm 10$

***Quadrupole interaction***

K (MHz)	$\eta$	$\varphi$ (deg)	$\theta$ (deg)	$\psi$ (deg)
$0.91 \pm 0.01$	$-0.4 \pm 0.05$	$0 \pm 20$	$39 \pm 10$	$0 \pm 10$

This parameters are very similar to those found for the  $H_{ox}$  state. The HF coupling is very anisotropic and the quadruple interaction is rather rhombic. Therefore this signal can be attributed to one of the CN ligands of the binuclear subcluster. On the other hand, since there are two CN ligands, present in the  $[2\text{Fe}]_H$  subcluster, it is expected to find two coupled  $^{14}\text{N}$  nuclear spins, as it was found for the  $H_{ox}$  state. Therefore it is expected to find more signals in the HYSCORE spectra.

Indeed, some ridges do not fit this interpretation even for the 'single-crystal'  $g_1$  HYSCORE spectrum. Since at this position of the magnetic field there is no contaminating signals, all ridges, found in HYSCORE spectra should correspond to the the  $L_2$  state. Thus, the presence of a second coupled  $^{14}\text{N}$  nuclear spin was suggested. Since all uninterpreted ridges are in  $(++)$  manifold a weak HF interaction is assumed. However, the complexity of the HYSCORE spectra does not allow to make a thorough analysis of the signals.

## 9.5 Investigation of the $^{13}\text{C}$ HF couplings

The electronic structure of the  $L_2$  state can be also probed by the  $^{13}\text{C}$  HFI from the coordinating CO ligands. For this study the  $H_{ox}$ -CO sample with three  $^{13}\text{C}$ - labeled CO ligands was used to generate the  $L_2$  state (sample 2, see section 6.3). In this sample the

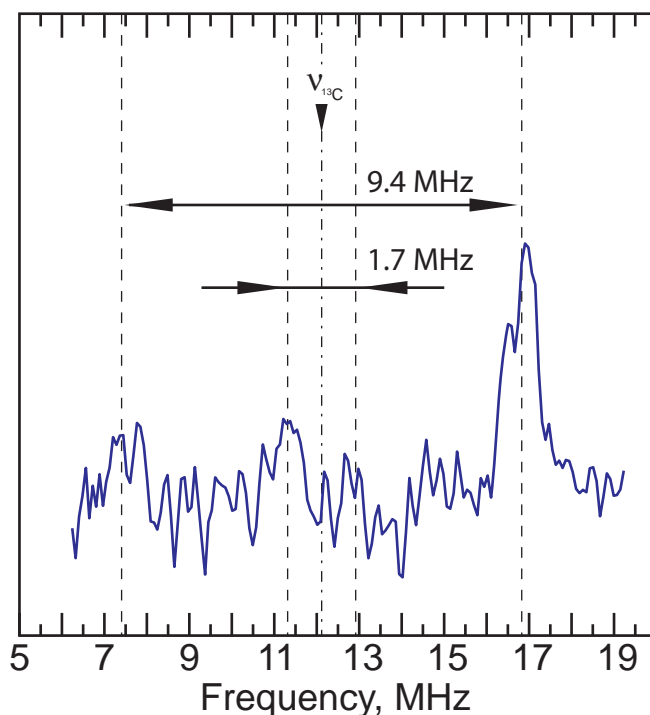


**Figure 9.9:** Q-band Davies ENDOR spectrum of the  $^{13}\text{C}$ -enriched H-cluster in  $L_2$  state. For preparation of the  $L_2$  state sample of triply  $^{13}\text{C}$  labeled enzyme in the  $\text{H}_{\text{ox}}\text{-CO}$  state (sample 2, discussed in sec. 6.3) has been used. Sample was illuminated for 40 min by OPO tuned to 530 nm at 50 K. Experimental conditions: temperature, 6K; MW freq., 33.823 GHz; magn.field, 1131.6 mT ( $g_2$ );  $t_{\text{mw}}^{\text{inv}} = 280$  ns;  $t_{\text{rf}} = 35\mu\text{s}$ .

external and terminal CO ligands of the distal iron are labeled as well as the bridging CO ligand. The measurements were done using the Q-band set-up since in X-band ENDOR, ESEEM and HYSCORE signals from the  $^{13}\text{C}$  nuclei are completely overlapping with the signals from  $^{14}\text{N}$  nuclei.

In the Q-band ENDOR spectra the signals from the  $^{13}\text{C}$  nuclei are well separated from those of  $^1\text{H}$  and  $^{14}\text{N}$ . Measurements at a magnetic field, corresponding to the maximum absorption in the spectrum of  $L_2$  reveals two pairs of peaks, centered at the  $\nu_{^{13}\text{C}} = 12.12$  MHz as it is shown in figure 9.9. One pair of shallow but reproducible peaks represents a very weak  $^{13}\text{C}$  HF coupling with a constant of 1.7 MHz at  $B_0 \parallel g_2$ . The second pair of peaks has a much larger amplitude and arise from a HF coupling constant of 9.4 MHz.

The light induced exchange of the  $^{13}\text{CO}$  ligands in the  $\text{H}_{\text{ox}}\text{-CO}$  state was estimated

to be about 56%<sup>2</sup>. According to an IR study [38] the external CO ligand remains in the structure of the L<sub>2</sub> state after light-induced conversion from the H<sub>ox</sub>-CO. Therefore it is expected, that as well as in the H<sub>ox</sub>-CO state, mostly the external CO ligand is labeled by <sup>13</sup>C in the case of the L<sub>2</sub> state. Hence, the observed peaks with larger amplitude (corresponding to the HF coupling of 9.4 MHz) are assigned to the external CO ligand of the distal iron. The terminal CO ligand of the proximal iron seems to be not involved in the photo-dissociation process. Therefore, the smaller <sup>13</sup>C HF coupling should be assigned either to the formal bridging CO ligand or to the terminal CO bond of the distal iron.

## 9.6 Discussion

### 9.6.1 Electronic structure

The investigation of the <sup>1</sup>H and the <sup>57</sup>Fe HF interactions of the [4Fe4S]<sub>H</sub> subcluster suggest that the [2Fe]<sub>H</sub>-[4Fe4S]<sub>H</sub> exchange interaction in the L<sub>2</sub> state is weaker than in the case of H<sub>ox</sub>-CO, which should result in larger HF coupling constants for <sup>57</sup>Fe nuclei of the binuclear subcluster. However, the HF coupling constants, found for the <sup>57</sup>Fe nuclei of the [2Fe]<sub>H</sub> subcluster are only slightly larger than in the case of the H<sub>ox</sub>-CO state. Moreover, the observed <sup>13</sup>C HF coupling, which most probably belongs to the carbon nucleus of the external CO is smaller than the one found for the H<sub>ox</sub>-CO state. A possible explanation of this phenomena is that the spin density is redistributed to the ligands of the iron atoms of the binuclear subcluster. This will certainly lower the spin density on the external CO bond and on the iron atoms.

Indeed, this has been confirmed by the investigation of the interactions of the <sup>14</sup>N nuclei. One <sup>14</sup>N nucleus was found to experience a relatively strong HF interaction. This <sup>14</sup>N HF interaction is stronger than in the H<sub>ox</sub>-CO state and in the H<sub>ox</sub> state of the H-cluster. Few additional signals in the (++) manifold of the X-band HYSCORE spectra, indicating another weakly coupled <sup>14</sup>N nucleus. Therefore, in contrast to the case of the H<sub>ox</sub> state, <sup>14</sup>N couplings of the CN ligands in the L<sub>2</sub> state are very asymmetric.

It is concluded, that the unpaired spin density is not equally distributed over the iron nuclei of the binuclear cluster. Taking into account observation of the relatively weak <sup>13</sup>C HF coupling of the external CO ligand it is suggested that the spin density is rather

<sup>2</sup>100% efficiency is when after illumination of the singly labeled (H<sub>ox</sub>-<sup>13</sup>CO) sample the <sup>13</sup>CO is equally distributed over all three positions for the CO ligands of the Fe<sub>d</sub>. Thus, the efficiency of 56% means that more than half of the <sup>13</sup>CO remains at the external position

localized on the proximal iron in contrast to the  $H_{ox}$  state. Consequently, the strong  $^{14}N$  HF coupling should be assigned to the cyanide ligand of the proximal iron.

### 9.6.2 Comparison with theoretical studies

Recently, two theoretical models of the  $L_2$  state of the H-cluster have been considered by Fiedler and Brunold [97]. In the first model the bridging CO ligand is completely dissociated. In the other model the formal bridging CO ligand is disconnected from the proximal iron and one intrinsic CO ligand of the distal iron is also removed.

Calculation of the singly occupied molecular orbitals (SOMOs) using spin-unrestricted DFT calculations reveal that in the first model 90% of the spin density is around the proximal iron and only 1% on the distal one. For the second model, the MO composition is vice-versa: most of the spin density is on the distal iron 78% and only a small amount on the proximal one (5%).

In the first model the spin-density is localized on the proximal iron which would lead to a strong exchange interaction between subunits of the H-cluster. It seems that for this model of the  $L_2$  state the  $[2Fe]_H$ - $[4Fe4S]_H$  exchange interaction should be similar or even greater than in the case of the  $H_{ox}$ -CO state <sup>3</sup>, which disagrees with conclusions based on the experimental observations, presented in this chapter.

Calculations on the second model reveal a complete shift of the spin density to the distal iron. This would certainly lead to a weakening of the  $[2Fe]_H$ - $[4Fe4S]_H$  exchange interaction probably even more than in the case of the  $H_{ox}$  state. Moreover, calculation reveal very strong (more than 20 MHz)  $^{13}C$  HF coupling on the carbon of the external CO bond which could not be confirmed by experimental findings.

Both these theoretical models assume lost of one CO ligand: bridging CO ligand for the first model and external CO ligand for the second. Since they both are not consistent with experimental observations it seems likely that the bridging CO bond is not completely lost. It is also consistent with the investigation of the photo-dissociation processes, presented in the previous chapter.

---

<sup>3</sup>As calculated by the authors of that article, in the case of the  $H_{ox}$ -CO state only 68% of the spin density is around the proximal iron (Fe 3d, 4s and 4p contributions), the rest is distributed over the distal iron, its ligands and about 5% on the  $S_{cys}$

---

# 10 Summary and Outlook

---

## 10.1 Summary

The active site of the [FeFe] hydrogenase consists of two subunits  $[2\text{Fe}]_{\text{H}}$  and  $[4\text{Fe}4\text{S}]_{\text{H}}$ , which are connected via sulfur of a cysteine. Both iron atoms of the bi-nuclear subcluster are coordinated by CO and CN ligands, keeping them in low oxidation states. The distal iron (corresponding to the 'cubane' subcluster) carries the "exchangeable" site, whose coordination changes in the catalytic cycle plays a key role in the hydrogenase reaction.

The electronic structure of the active site of the [FeFe]hydrogenase from *Desulfovibrio desulfuricans* has been probed for all paramagnetic states of the active enzyme using various EPR methods (i.e. EPR (both CW and pulse), pulse ENDOR, pulse TRIPLE, HYSCORE). Detailed investigations have been performed on  $^{13}\text{C}$ ,  $^{57}\text{Fe}$  enriched and the non-enriched enzyme in the active oxidized ( $\text{H}_{\text{ox}}$ ) state and its CO derivative ( $\text{H}_{\text{ox}}\text{-CO}$ ). Moreover, an EPR study has been performed on the light-induced states, resulting from illumination of the  $\text{H}_{\text{ox}}\text{-CO}$  state. Measurements of the hyperfine coupling constants of the  $^1\text{H}$ ,  $^{13}\text{C}$  (CO),  $^{14}\text{N}$  (CN) and  $^{57}\text{Fe}$  nuclei and quadrupole coupling constants of the  $^{14}\text{N}$  provided extensive information about the electronic structure.

During study of the  $\text{H}_{\text{ox}}\text{-CO}$  state of the H-cluster it was found that the  $[2\text{Fe}]_{\text{H}}\text{-}[4\text{Fe}4\text{S}]_{\text{H}}$  exchange interaction is very strong, resulting in large HF coupling constants of the  $^{57}\text{Fe}$  nuclei of the  $[4\text{Fe}4\text{S}]_{\text{H}}$  subcluster. The study of the electronic structure of the  $[2\text{Fe}]_{\text{H}}$  subcluster reveals a moderate distribution of the unpaired electron over the two iron atoms, which was confirmed by observation of a  $^{13}\text{C}$  HF interaction of the external CO bond of the distal iron. Applying the theoretical exchange-coupling model to the experimental data, it was suggested, that most of the spin density is located around the proximal iron, which is connected to the bridging  $\text{S}_{\text{cys}}$ .

In contrast to the  $\text{H}_{\text{ox}}\text{-CO}$  state, the measured  $^{57}\text{Fe}$  HF couplings of the H-cluster in the  $\text{H}_{\text{ox}}$  state indicate a rather weak intra-cluster exchange interaction. The unpaired electron was found to be almost equally distributed over the two iron nuclei in the  $[2\text{Fe}]_{\text{H}}$

## 10.1 Summary

---

subcluster. This was also confirmed by the study of the  $^{14}\text{N}$  HF coupling constants of the cyanides. Using X-band HYSCORE method, two  $^{14}\text{N}$  nuclei were identified and assigned to the cyanides. Detailed investigation of the Q-band HYSCORE spectra (which have better resolution) revealed presence of the third coupled  $^{14}\text{N}$  nuclear spin which was attributed to the  $-\text{CH}_2\text{-NH-CH}_2-$  (DTN) moiety of the dithiol bridging ligand of the irons in the binuclear subcluster. Comparison of the obtained results with spectroscopic data available in literature for the active state of the [FeFe] hydrogenase (type II, uptake) from *Clostridium pasteurianum* reveals differences in the  $^{57}\text{Fe}$  HF coupling constants, which suggests that these active sites may have different electronic and geometrical structures.

From the comparative analysis of the obtained spectroscopic data for different investigated states it is concluded, that the presence of the additional CO ligand in the external site of the distal iron has a strong influence on the electronic structure of the H-cluster by increasing the  $[2\text{Fe}]_{\text{H}}\text{-}[4\text{Fe}4\text{S}]_{\text{H}}$  exchange interaction.

During the study of the photo-dissociation of the CO ligands of the H-cluster in the  $\text{H}_{\text{ox}}\text{-CO}$  state two light-induced species have been detected using EPR techniques. Q-band pulse ENDOR allows the identification of one of them as the  $\text{H}_{\text{ox}}$  state. The EPR signal of this state is increasing with time, while the signal of the  $\text{H}_{\text{ox}}\text{-CO}$  state is decreasing. The EPR signal of the second light-induced species ( $\text{L}_2$ ) initially increases rapidly but after a certain time starts to decrease. The kinetic model of the photo-induced conversion, which has the best fit to the experimental kinetic profiles, assumes separate reversible conversion pathways from the  $\text{H}_{\text{ox}}\text{-CO}$  state to the  $\text{L}_2$  and the  $\text{H}_{\text{ox}}$  states. According to this model there does not occur any  $\text{L}_2 \rightleftharpoons \text{H}_{\text{ox}}$  conversion. Study of the wavelength dependence of the photo-dissociation processes reveal an increase of all rates with decreasing wavelength, which is consistent with the general profile of the UV/Vis absorption spectra of the [FeFe] hydrogenase.

For the first time the investigation of the electronic structure of the  $\text{L}_2$  state has been performed by studying of the interactions of the  $^1\text{H}$ ,  $^{13}\text{C}$ ,  $^{14}\text{N}$  and  $^{57}\text{Fe}$  nuclei the H-cluster. A relatively strong  $[2\text{Fe}]_{\text{H}}\text{-}[4\text{Fe}4\text{S}]_{\text{H}}$  exchange interaction was identified from the investigation of the  $^{57}\text{Fe}$  and  $^1\text{H}$  HF couplings. Quantitatively this exchange coupling is stronger than in the  $\text{H}_{\text{ox}}$  state and weaker than in the  $\text{H}_{\text{ox}}\text{-CO}$  state. As compared to the  $\text{H}_{\text{ox}}\text{-CO}$  state, in the  $\text{L}_2$  state the unpaired spin density is more distributed over the cyanide ligands of  $\text{Fe}_{\text{d}}$  and  $\text{Fe}_{\text{p}}$ , which was concluded from the study of the  $^{14}\text{N}$  interactions. However, in contrast to the  $\text{H}_{\text{ox}}$  state, this distribution is not equal for both CN ligands of the  $[2\text{Fe}]_{\text{H}}$  subcluster. From the consideration of the theoretical exchange coupling model

and an earlier DFT study of models of the  $L_2$  state it was concluded, that most of the spin density is located at the proximal iron ( $Fe_p$ ) and its intrinsic ligands. However, the observed  $^{13}C$  HF coupling of the external CO ligand indicates the presence of some spin density on the distal iron.

The rise and subsequent decrease of the EPR signal of the  $L_2$  state upon illumination of the  $H_{ox}$ -CO state is the fastest observed photo-dissociation process. Therefore it seems likely, that the bridging CO ligand is not completely dissociated in this process. This leads to the conclusion that in the  $L_2$  state the former bridging CO ligand becomes the terminal ligand of one of the iron atoms ( $Fe_p$  or  $Fe_d$ ). This is also supported by the discrepancy between the experimental results and DFT model assuming the absence of the bridging CO ligand.

## 10.2 Outlook

A detailed study on the electronic structure of the H-cluster in different states has been presented in this thesis. It was demonstrated, that the electronic structure is very dependent on the intra-cluster exchange interaction. Therefore, in order to construct a correct theoretical model of the active site, one should include the 'cubane' subcluster into the calculations (i.e. DFT).

High-field EPR studies of the H-cluster in its paramagnetic states should be performed in order to increase the precision of the determined parameters of the  $^{14}N$  and  $^{57}Fe$  nuclear spin interactions. EPR measurements, performed on single crystal samples may clarify the orientation of the g-tensor within the structure of the H-cluster. Moreover it would also help to resolve relative orientations of the HF tensors. This would lead to further detailing knowledge about the electronic structure of the H-cluster.

Application of the same methods to the [FeFe] hydrogenases from other organisms (e.g. *Chlamydomonas reinhardtii*) should extend the knowledge about differences of the active sites and their relations to the activities of the enzymes.

Investigation of inorganic model complexes of the active center may relate structural properties of the models to the native H-cluster and therefore help in construction the functional models of hydrogen evolving complexes.



## References

- [1] Cammack, R., Frey, M. and Robson, R: *Hydrogen as a Fuel. Learning from Nature*. Taylor & Francis Inc., 2001.
- [2] Adams, M.W.W. // *Biochimica et Biophysica Acta*, 594: 105–176 , (1981). BBA 86068.
- [3] Heidelberg, John F, Seshadri, Rekha, Haveman, Shelley A, Hemme, Christopher L, Paulsen, Ian T, Kolonay, James F, Eisen, Jonathan A, Ward, Naomi, Methe, Barbara, Brinkac, Lauren M, Daugherty, Sean C, Deboy, Robert T, Dodson, Robert J, Durkin, A Scott, Madupu, Ramana, Nelson, William C, Sullivan, Steven A, Fouts, Derrick, Haft, Daniel H, Selengut, Jeremy, Peterson, Jeremy D, Davidsen, Tanja M, Zafar, Nikhat, Zhou, Liwei, Radune, Diana, Dimitrov, George, Hance, Mark, Tran, Kevin, Khouri, Hoda, Gill, John, Utterback, Terry R, Feldblyum, Tamara V, Wall, Judy D, Voordouw, Gerrit and Fraser, Claire M // *Nat Biotech*, 22: 554–559 , (2004).
- [4] Volbeda, A., Charon, M.H., Piras, C., Hatchikian, E.C., Frey, M. and FontecillaCamps, J.C. // *Nature*, 373: 580–587 , (1995).
- [5] Volbeda, A., Garcia, E., Piras, C., deLacey, A.L., Fernandez, V.M., Hatchikian, E.C., Frey, M. and FontecillaCamps, J.C. // *Journal of the American Chemical Society*, 118: 12 989–12 996 , (1996).
- [6] Bagley, K.A., Vangarden, C.J., Chen, M., Duin, E.C., Albracht, S.P.J. and Woodruff, W.H. // *Biochemistry*, 33: 9229–9236 , (1994).
- [7] Bagley, K.A., Duin, E.C., Roseboom, W., Albracht, S.P.J. and Woodruff, W.H. // *Biochemistry*, 34: 5527–5535 , (1995).
- [8] VanderSpek, T.M., Arendsen, A.F., Happe, R.P., Yun, S.Y., Bagley, K.A., Stufkens, D.J., Hagen, W.R. and Albracht, S.P.J. // *European Journal of Biochemistry*, 237: 629–634 , (1996).
- [9] Albracht, S.P.J. // *Biochimica et Biophysica Acta-Bioenergetics*, 1188: 167–204 , (1994).

## REFERENCES

---

- [10] Surerus, K.K., Chen, M., Vanderzwaan, J.W., Rusnak, F.M., Kolk, M., Duin, E.C., Albracht, S.P.J. and Münck, E. // *Biochemistry*, 33: 4980–4993 , (1994).
- [11] Foerster, S., Stein, M., Brecht, M., Ogata, H., Higuchi, Y. and Lubitz, W. // *J.Am.Chem.Soc.*, 125: 83–93 , (2003).
- [12] Armstrong, F.A. // *Current Opinion in Chemical Biology*, 8: 133–140 , (2004).
- [13] Rieder, R., Cammack, R. and Hall, D.O. // *European Journal of Biochemistry*, 145: 637–643 , (1984).
- [14] Teixeira, M., Moura, I., Fauque, G., Czechowski, M., Berlier, Y., Lespinat, P.A., Le Gall, J., Xavier, A.V. and Moura, J.J. // *Biochimie*, 68: 75–84 , (1986).
- [15] Teixeira, M., Fauque, G., Moura, I., Lespinat, P.A., Berlier, Y., Prickril, B., Peck, H.D. Jr., Xavier, A.V., Le Gall, J. and Moura, J.J. // *European Journal of Biochemistry*, 167: 47–58 , (1987).
- [16] Pereira, A.S., Franco, R., Feio, M.J., Pinto, C., Lampreia, J., Reis, M.A., Calvete, J., Moura, I., Beech, I., Lino, A.R. and Moura, J.J. // *Biochemical and biophysical research communications*, 221: 414–421 , (1996).
- [17] Garcin, E, Vernede, X, Hatchikian, E.C., Volbeda, A, Frey, M and Fontecilla-Camps, J.C. // *Structure*, 7: 557–566 , (1999).
- [18] Berkessel, A. and Thauer, R.K. // *Angewandte Chemie-International Edition in English*, 34: 2247–2250 , (1995).
- [19] Berkessel, A. // *Current Opinion in Chemical Biology*, 5: 486–490 , (2001).
- [20] Lyon, E.J., Shima, S., Boecher, R., Thauer, R.K., Grevels, F.W., Bill, E., Roseboom, W. and Albracht, S.P.J. // *Journal of the American Chemical Society*, 126: 14 239–14 248 , (2004).
- [21] Shima, S., Lyon, E.J., Sordel-Klippert, M.S., Kauss, M., Kahnt, J., Thauer, R.K., Steinbach, K., Xie, X.L., Verdier, L. and Griesinger, C. // *Angewandte Chemie-International Edition*, 43: 2547–2551 , (2004).
- [22] Lyon, E.J., Shima, S., Buurman, G., Chowdhuri, S., Batschauer, A., Steinbach, K. and Thauer, R.K. // *European Journal of Biochemistry*, 271: 195–204 , (2004).
- [23] Schwörer, B., Fernandez, Victor M., Zirngibl, Carmen and Thauer, Rudolf K. // *European Journal of Biochemistry*, 212: 255–261 , (1993).
- [24] Adams, M.W.W. // *Biochimica et Biophysica Acta*, 1020: 115–145 , (1990).

- 
- [25] Nicolet, Y., Piras, C., Legrand, P., Hatchikian, C.E. and Fontecilla-Camps, J.C. // *Structure with Folding & Design*, 7: 13–23 , (1999).
- [26] Lemon, B.J. and Peters, J.W. // *Biochemistry*, 38: 12 969–12 973 , (1999).
- [27] Chen, J.S. and Mortenso, L.E. // *Biochimica et Biophysica Acta*, 371: 283–298 , (1974).
- [28] Adams, M.W.W // *Journal of Biological Chemistry*, 262: 15 054–15 061 , (1987).
- [29] Chen, J.S. and Blanchard, D.K. // *Biochemical And Biophysical Research Communications*, 84: 1144–1150 , (1978).
- [30] Adams, M.W.W. and Mortenson, L.E. // *Biochimica et Biophysica Acta*, 766: 51–61 , (1984).
- [31] Adams, M.W.W. and Mortenson, L.E. // *Journal of Biological Chemistry*, 259: 7045–7055 , (1984).
- [32] Peters, J.W., Lanzilotta, W.N., Lemon, B.J. and Seefeldt, L.C. // *Science*, 282: 1853–1858 , (1998).
- [33] Montet, Y., Amara, P., Volbeda, A., Vernede, X., Hatchikian, E.C., Field, M.J., Frey, M. and Fontecilla-Camps, J.C. // *Nature Structural Biology*, 4: 523–526 , (1997).
- [34] Lemon, B.J. and Peters, J.W. // *Journal of the American Chemical Society*, 122: 3793–3794 , (2000).
- [35] Nicolet, Y., de Lacey, A.L., Vernede, X., Fernandez, V.M., Hatchikian, E.C. and Fontecilla-Camps, J.C. // *Journal of the American Chemical Society*, 123: 1596–1601 , (2001).
- [36] Pierik, A.J., Hulstein, M., Hagen, W.R. and Albracht, S.P.J. // *European Journal of Biochemistry*, 258: 572–578 , (1998).
- [37] de Lacey, A.L., Stadler, C., Cavazza, C., Hatchikian, E.C. and Fernandez, V.M. // *Journal of the American Chemical Society*, 122: 11 232–11 233 , (2000).
- [38] Albracht, S.P.J., Roseboom, W. and Hatchikian, C. // *Journal of Biological Inorganic Chemistry*, 11: 88–101 , (2006).
- [39] Thomann, H., Bernardo, M. and Adams, M.W.W. // *Journal of the American Chemical Society*, 113: 7044–7046 , (1991).

## REFERENCES

---

- [40] Van Dam, P.J., Reijerse, E.J. and Hagen, W.R. // *European Journal of Biochemistry*, 248: 355–361 , (1997).
- [41] Chen, Z.J., Lemon, B.J., Huang, S., Swartz, D.J., Peters, J.W. and Bagley, K.A. // *Biochemistry*, 41: 2036–2043 , (2002).
- [42] Fan, H.J. and Hall, M.B. // *Journal of the American Chemical Society*, 123: 3828–3829 , (2001).
- [43] Georgakaki, I.P., Thomson, L.M., Lyon, E.J., Hall, M.B. and Darensbourg, M.Y. // *Coordination Chemistry Reviews*, 238: 255–266 , (2003).
- [44] Hatchikian, E.C., Forget, N., Fernandez, V.M., Williams, R. and Cammack, R. // *European Journal of Biochemistry*, 209: 357–365 , (1992).
- [45] Patil, D.S., Huynh, B.H., He, S.H., Peck, H.D., Dervartanian, D.V. and Legall, J. // *Journal of the American Chemical Society*, 110: 8533–8534 , (1988).
- [46] Hatchikian, E.C., Magro, V., Forget, N., Nicolet, Y. and Fontecilla-Camps, J.C. // *Journal of Bacteriology*, 181: 2947–2952 , (1999).
- [47] Roseboom, W., de Lacey, A.L., Fernandez, V.M., Hatchikian, C. and Albracht, S.P.J. // *Journal of Biological Inorganic Chemistry*, 11: 102–118 , (2006).
- [48] Wang, G., Benecky, M.J., Huynh, B.H., Cline, J.F., Adams, M.W.W., Mortenson, L.E., Hoffman, B.M. and Münck, E. // *Journal of Biological Chemistry*, 259: 4328–4331 , (1984).
- [49] Telser, J., Benecky, M.J., Adams, M.W.W., Mortenson, L.E. and Hoffman, B.M. // *Journal of Biological Chemistry*, 262: 6589–6594 , (1987).
- [50] Patil, D.S., Moura, J.J.G., He, S.H., Teixeira, M., Prickril, B.C., Dervartanian, D.V., Peck, H.D., Legall, J. and Huynh, B.H. // *Journal of Biological Chemistry*, 263: 18 732–18 738 , (1988).
- [51] Kowal, A.T., Adams, M.W.W. and Johnson, M.K. // *Journal of Biological Chemistry*, 264: 4342–4348 , (1989).
- [52] Popescu, C.V. and Münck, E. // *Journal of the American Chemical Society*, 121: 7877–7884 , (1999).
- [53] Vandijk, C., Mayhew, S.G., Grande, H.J. and Veeger, C. // *European Journal of Biochemistry*, 102: 317–330 , (1979).
- [54] Hagen, W.R., Vanberkelarts, A., Krusewolters, K.M., Dunham, W.R. and Veeger, C. // *Febs Letters*, 201: 158–162 , (1986).

- [55] Vandijk, C., Vanberkelarts, A. and Veeger, C. // *Febs Letters*, 156: 340–344 , (1983).
- [56] Bennett, B., Lemon, B.J. and Peters, J.W. // *Biochemistry*, 39: 7455–7460 , (2000).
- [57] Cao, Z.X. and Hall, M.B. // *Journal of the American Chemical Society*, 123: 3734–3742 , (2001).
- [58] Liu, Z.P. and Hu, P. // *Journal of the American Chemical Society*, 124: 5175–5182 , (2002).
- [59] Bruschi, M., Fantucci, P. and De Gioia, L. // *Inorganic Chemistry*, 42: 4773–4781 , (2003).
- [60] Pereira, A.S., Tavares, P., Moura, I., Moura, J.J.G. and Huynh, B.H. // *Journal of the American Chemical Society*, 123: 2771–2782 , (2001).
- [61] George, S.J., Cui, Z., Razavet, M. and Pickett, C.J. // *Chemistry-A European Journal*, 8: 4037–4046 , (2002).
- [62] Darensbourg, M.Y., Lyon, E.J., Zhao, X. and Georgakaki, I.P. // *Proceedings of the National Academy of Sciences of the United States of America*, 100: 3683–3688 , (2003).
- [63] Bominaar, E.L., Hu, Z.G., Münck, E., Girerd, J.J. and Borshch, S.A. // *Journal of the American Chemical Society*, 117: 6976–6989 , (1995).
- [64] Belinsky, M.I. // *Journal of Biological Inorganic Chemistry*, 1: 186–188 , (1996).
- [65] Xia, J.Q., Hu, Z.G., Popescu, C.V., Lindahl, P.A. and Münck, E. // *Journal of the American Chemical Society*, 119: 8301–8312 , (1997).
- [66] Mouesca, J.-M., Noodleman, L., Case, D. A. and Lamotte, B. // *Inorganic Chemistry*, 34: 4347–4359 , (1995).
- [67] Sun, L.C., Akermark, B. and Ott, S. // *Coordination Chemistry Reviews*, 249: 1653–1663 , (2005).
- [68] Rudowicz, C. and Misra, S.K. // *Applied Spectroscopy Reviews*, 36: 11–63 , (2001).
- [69] Schweiger, A. and Jeschke, G: *Principles of Pulse electron paramagnetic Resonance*. Oxford University Press, 2001.
- [70] Abragam, A and Bleaney, B.: *Electron paramagnetic resonance of transition ions*. Oxford University Press, 1986.

## REFERENCES

---

- [71] Slichter, C. P.: *Principles of Magnetic Resonance*. third. Edition. Springer Verlag, Berlin, 1990.
- [72] Atherton, N.M.: *Principles of Electron Spin Resonance*. Ellis Horwood, 1993.
- [73] McGarvey // *Journal Of Physical Chemistry*, 71: 51–67 , (1967).
- [74] Poole, C.P.: *Electron Spin Resonance*. Wiley, New York, 1983.
- [75] Rowan, L.G., Hahn, E.L. and Mims, W.B. // *Physical Review*, A137: 61 , (1965).
- [76] Mims, W.B. // *Physical Review B*, 5: 2409 , (1972).
- [77] Hoff, A.J., Editor. *Advanced EPR. Application in Biology and Biochemistry*. Elsevier, 1989.
- [78] Mehring, M., Höfer, P and Grupp, A // *Ber.Bunsenges. Phys.Chem.*, 91: 1137–1137 , (1987).
- [79] Gemperle, C and Schweiger, A // *Chemical Physics*, 91: 1481–1505 , (1991).
- [80] Mims, W.B. // *Proceedings of The Royal Society of London Series A-Mathematical And Physical Sciences*, 283: 452 , (1965).
- [81] Davies, E.R // *Physics Letters A*, A47: 1–2 , (1974).
- [82] Cook, R.J. and Whiffen, D.H. // *Proceedings of The Physical Society Of London*, 84: 845 , (1964).
- [83] Dinse, K.P., Biehl, R and Möbius, K // *Journal of Chemical Physics*, 61: 4335–4341 , (1974).
- [84] Höfer, P.: *Entwicklung von Puls-ENDOR-verfahren und Ihre Anwendung auf Polyazetylen*. University Stuttgart, PhD thesis, 1988.
- [85] Höfer, P., Grupp, A., Nebenfuhr, H. and Mehring, M. // *Chemical Physics Letters*, 132: 279–282 , (1986).
- [86] Shane, J.J., Höfer, P., Reijerse, E.J. and Deboer, E. // *Journal of Magnetic Resonance*, 99: 596–64 , (1992).
- [87] Szosenfogel, R. and Goldfarb, D. // *Mol.Phys.*, 95: 1295–1308 , (1998).
- [88] Stoll, S., Calle, C., Mitrikas, G. and Schweiger, A. // *J.Magn.Reson.*, 177: 93–101 , (2005).
- [89] Slichter, C.P.: *Principles of magnetic resonance*. Springer, 1981.

- [90] Ernst, R.R., Bodenhausen, G. and Wokaun, A.: *Principles of Nuclear Magnetic Resonance in One and Two Dimensions*. Clarendon press, Oxford, 1987.
- [91] Sienkiewicz, A., Smith, B.G., Veselov, A. and Scholes, C.P. // *Rev.Sci.Instrum.*, 67: 2134–2138 , (1996).
- [92] Epel, B., Arieli, D., Baute, D. and Goldfarb, D. // *Journal of Magnetic Resonance*, 164: 78–83 , (2003).
- [93] Epel, B., Gromov, I., Stoll, S., Schweiger, A. and Goldfarb, D. // *Concepts in Magnetic Resonance Part B-Magnetic Resonance Engineering*, 26B: 36–45 , (2005).
- [94] Epel, B., Poppl, A., Manikandan, P., Vega, S. and Goldfarb, D. // *J.Magn.Reson.*, 148: 388–397 , (2001).
- [95] Epel, B. and Goldfarb, D. // *J.Magn.Reson.*, 146: 196–203 , (2000).
- [96] Goldfarb, D., Epel, B., Zimmermann, H. and Jeschke, G. // *J.Magn.Reson.*, 168: 75–87 , (2004).
- [97] Fiedler, A.T. and Brunold, T.C. // *Inorganic Chemistry*, 44: 1794–1809 , (2005).
- [98] Willems, J.-P., Reijerse, E.J. and deBoer, E. // *Molecular Physics*, 83: 1155–1169 , (1994).
- [99] Volbeda, A and Fontecilla-Camps, J.C. // *Dalton Transactions*, : 4030–4038 , (2003).
- [100] Telser, J., Lee, H.I. and Hoffman, B.M. // *Journal of Biological Inorganic Chemistry*, 5: 369–380 , (2000).
- [101] Stoll, S. and Schweiger, A. // *J.Magn.Reson.*, 178: 42–55 , (2006).
- [102] Telser, J, Benecky, M.J., M.W.W., Adams, Mortenson, L.E. and Hoffman, B.M. // *Journal of Biological Chemistry*, 261: 13 536–13 541 , (1986).
- [103] Georgakaki, I.P., Thomson, L.M., Lyon, E.J., Hall, M.B. and Darensbourg, M.Y. // *Coordination Chemistry Reviews*, 238: 255–266 , (2003).
- [104] Patil, D.S., Huynh, B.H., He, S.H., Peck, H.D., Dervartanian, D.V. and Legall, J. // *Journal of the American Chemical Society*, 110: 8533–8534 , (1988).
- [105] Peters, J.W., Lemon, B.J. and Shankarling, G. // *Abstracts of Papers of the American Chemical Society*, 224: U645–U645 , (2002).
- [106] Lyon, E.J., Georgakaki, I.P., Reibenspies, J.H. and Darensbourg, M.Y. // *Journal of the American Chemical Society*, 123: 3268–3278 , (2001).

# *Curriculum Vitae*

**First name:** Alexey

**Surname:** Silakov

**Born in:** 1981, 23 of January.

**Birth place:** Russia, Tatarstan

**Nationality:** Russian

**Education:**

1987 - 1997 Basic Schooling, Russia

1997 - 2001 B.Sc. (Radiophysics), department of Physics, Kazan State University, Kazan, Russia

2001 - 2003 M.Sc. (Physics), department of Physics, Kazan State University, Kazan, Russia

2003 - 2007 PhD student, Max-Planck-Institut für Bioanorganische Chemie, Mülheim a.d. Ruhr;  
der Henrich-Heine-Universität, Düsseldorf, Germany

**Further training:**

EPR Summer school, 17-24 July, Wiesbaden, Germany, 2005

DEER school, 6-7 April, St.Andrews, United Kingdom, 2006

**List of Publications:**

S.Sen, R. Rakhmatullin, R. Gubaidullin, A. Silakov, "A pulsed EPR study of clustering of Yb<sup>3+</sup> ions incorporated in GeO<sub>2</sub> glass" // J. Non-Crystalline Solids 333 (2004) 22-27

A. Silakov, E. J. Reijerse, S.P.J. Albracht, E. C. Hatchikian, W Lubitz, "The electronic structure of the H cluster in the [FeFe]-hydrogenase from *Desulfovibrio desulfuricans*. A Q-band <sup>57</sup>Fe-ENDOR and HYSCORE study" // J.Am.Chem.Soc. (submitted)

A. Silakov, E. J. Reijerse, S.P.J. Albracht, W Lubitz, "Investigation of CN and CO ligands of the active center of the [FeFe]-hydrogenase from *Desulfovibrio desulfuricans*. A pulse EPR study of the <sup>13</sup>C and <sup>14</sup>N nuclear spin interactions". // J.Biol.Inorg.Chem (in preparation)

A. Silakov, E. J. Reijerse, S.P.J. Albracht, W Lubitz, "Photo-dissociation of the active center of the [FeFe]-hydrogenase from *Desulfovibrio desulfuricans* in the CO-inhibited state". // J.Biol.Inorg.Chem (in preparation).

**List of oral presentations:**

A. Silakov, E. J. Reijerse, S.P.J. Albracht, E. C. Hatchikian, W Lubitz, "Investigation of the active site of the Fe-only hydrogenase using pulse EPR" // Specialized Colloque AMPERE "EPR and ENDOR Spectroscopy of Metal Proteins and Spin-Labeled Proteins" 29.June-1.July, Leiden, The Netherlands, 2005

A. Silakov, E. J. Reijerse, S.P.J. Albracht, E. C. Hatchikian, W Lubitz, "Investigation of the active site of the Fe-only hydrogenase using pulse EPR" // 39th Annual International Meeting "Advanced Techniques and Application of EPR" 2-5 April, Edunburgh, United Kingdom, 2006

**List of poster presentations:**

A. Silakov, E. J. Reijerse, S.P.J. Albracht, E. C. Hatchikian, W Lubitz, // "Modern development of Magnetic Resonance", 15-20 August, Kazan Russia, 2004

A. Silakov, E. J. Reijerse, , W Lubitz, // DFG-Meeting - schwerpunktprogramm "Hochfield-EPR in Biologie, Chemie und Physik", 16-18 February, Hunfield, Germany, 2005

A. Silakov, E. J. Reijerse, W Lubitz, // Specialized Colloque AMPERE "EPR and ENDOR Spectroscopy of Metal Proteins and Spin-Labeled Proteins" 29.June-1.July, Leiden, The Netherlands, 2005

A. Silakov, E. J. Reijerse, S. Albracht, C. Hatchikian, W. Lubitz // EUROMAR 2005/EENC 2005, 3-8 July, Veldhoven, The Netherlands, 2005

A. Silakov, E. J. Reijerse, S. Albracht, C. Hatchikian, W. Lubitz // EPR Summer School 2005, 17-24 July, Wiesbaden, Germany, 2005

A. Silakov, E. J. Reijerse, W. Lubitz // 39th Annual International Meeting "Advanced Techniques and Application of EPR" 2-5 April, Edunburgh, United Kingdom, 2006

A. Silakov, E. J. Reijerse, W. Lubitz // SOLAR-H Workshop, 25-28 April, Gelsenkirchen, Germany, 2006

**Prizes and Awards:**

Prize for the Best poster // SOLAR-H Workshop, 25-28 April, Gelsenkirchen, Germany, 2006

**Other activities**

Some results of my work have been chosen for the cover of "EPR NEWS LETTER" journal n.16 (1), 2006